DESIGN AND DEVELOPMENT OF A MID-INFRARED CARBON MONOXIDE SENSOR FOR A HIGH-PRESSURE COMBUSTOR RIG

A Thesis

by

ALEJANDRO CAMOU

Submitted to the Office of Graduate and Professional Studies of
Texas A&M University
in partial fulfillment of the requirements for the degree of

MASTER OF SCIENCE

Chair of Committee,	Eric L. Petersen
Committee Members,	David A. Staack
	Rodney Bowersox
Head of Department,	Andreas A. Polycarpou

May 2014

Major Subject: Mechanical Engineering

ABSTRACT

A sensor for carbon monoxide measurement has been developed using a mid-infrared quantum-cascade (QC) laser operating in the fundamental band ($\Delta v = 1$) of CO near 4.5 μm. The fundamental band was chosen due to its stronger absorption line-strengths compared to the overtone bands near 2.3 μm and 1.55 μm. The mid-IR sensor was applied to a high-pressure combustor to determine the time-history of carbon monoxide and compare it to other measured combustor parameters to fully characterize the combustor's performance. A mixture of natural gas, oxygen, and carbon dioxide was used for combustion. An emissions probe was connected to the exhaust of the combustor that fed into an absorption cell with a known path length and two optical ports to allow mid-IR laser access for absorption. The temperature and pressure of the cell were measured, and the laser wavelength was monitored by a separate calibration process using a known CO/N_2 mixture. The operating wavelength was measured at the R(12) transition of 2190.01667 cm^{-1} (4.56618 μm) within ± 0.0008 cm^{-1} (± 0.01625μm) from CO absorption measurements using the known CO/N_2 mixture. This operating wavelength uncertainty was used to measure the uncertainty of the calculated CO absorption coefficient. The mid-IR sensor measured a CO concentration of 67 ppm ± 12 ppm at a steady rig temperature and rig pressure of approximately 2300˚F and 1500 psig, respectively. This measured CO concentration was comparable to equilibrium calculations with respect to the rig stable conditions.

The QC laser was also applied to validate the absorption time-history of a CO/Ar mixture at elevated temperatures and pressures in a shock tube at Texas A&M University. In addition to direct absorption measurements for CO in an absorption cell, the mid-IR sensor was also adapted to measure the hydrocarbon fuel concentration using a 3.39 μm HeNe laser. This method was used to validate the laser for potential mid-IR laser diagnostics for unburned hydrocarbon (UHC) concentration measurements. A fiber-coupled mid-IR sensor method was proposed for the direct CO absorption measurements through the combustor exhaust liner. The spectroscopic parameters of CO were determined using HITRAN. The broadening behavior of CH_4-CO_2 was experimentally determined on-site for mid-IR sensor calibration for hydrocarbon concentration measurements. The mid-IR sensor proved to provide successful CO time-histories during combustion at both transient and steady combustor conditions. The uncertainty in CO concentration can be reduced by eliminating condensation within the gas lines. The sensor also proved to capture the fuel flow variations while showing room for improvement in the broadening behavior. These tests using direct absorption spectroscopy (DAS) demonstrated the mid-IR sensor capability for species concentration measurements on a high-pressure combustor.

ACKNOWLEDGEMENTS

I would like to thank my advisor and committee chair, Dr. Eric Petersen, for his guidance and support throughout my graduate career. The knowledge and experience I gained under Dr. Eric Petersen has given me the tools necessary for my professional career in the future. I would also like to thank my committee members, Dr. David Staack, Dr. Rodney Bowersox as well as Dr. Simon North for their time and consideration throughout the course of my graduate work. I would also like to thank the engineers from Parametric Solutions Inc. (PSI) especially David Cusano and Mark Harris for their support and guidance during the rig performance tests, as well as the technicians from Wyle Laboratories for their help during the development and coupling of the mid-IR sensor.

I would like to thank my co-workers and friends that helped throughout my work. Specifically, I would like to thank Anabel Valencia, Dr. Christopher Aul, Jose Emiliano Vivanco, Clayton Mulvihill, Anibal Morones, and Olivier Mathieu for their advice, guidance and support throughout my graduate work.

Finally, I would like to thank my family for their support throughout the years. My family gave me the motivation, passion and dedication I needed to continue my professional career and to perform with the best of my abilities.

NOMENCLATURE

Abbreviations

$\left(A/F\right)_{stoic}$	Stoichiometric air-to-fuel ratio
$\left(A/F\right)$	Real air-to-fuel ratio
A	Helmholtz function (kJ)
A_i	Integrated absorbance of species *i* (cm^{-1})
c	Speed of light (m/s)
c_p	Specific heat (kJ/kg-K)
$\bar{c}_{p,i}$	Molar specific heat of species *i* (kJ/kmol-K)
E	Internal energy of a closed system (kJ)
E_u	Upper energy state
E_l	Lower energy state
ΔE	Energy separation
E''	Lower-state energy (cm^{-1})
G	Gibbs function (kJ)
G_{mix}	Total mixture Gibbs free energy (kJ)
g_j	Statistical weight
$\bar{g}_{f,i}$	Gibbs energy of formation of species *i* (kJ/kmol)
H	Enthalpy (kJ)
H_{mix}	Total mixture enthalpy (kJ)

$\bar{h}_{f,i}$	Enthalpy of formation of species *i* (kJ/kmol)
h_p	Planck's constant (J s)
$\bar{h}_i$	Molar enthalpy of species *i* (kJ/kmol)
I	Molecular moment of inertia (kg m^2)
I_o	Incident intensity from IR detector (reference) (V)
I_t	Transmitted intensity from IR detector (transmitted) (V)
J	Rotational quantum number
K_p	Equilibrium Constant
k	Boltzmann constant (m^2 kg s^{-2} K^{-1})
k_f	Force constant ($aJ\ \dot{A}^{-2}$)
k_v	Absorption coefficient (cm^{-1} atm^{-1})
L	Absorption path length (cm)
MW_{air}	Molecular weight of air (kg/kmol)
MW_{fuel}	Molecular weight of fuel (kg/kmol)
m_{air}	Mass of air (kg)
m_{fuel}	Mass of fuel (kg)
m_j	Broadening shifting temperature index (cm^{-1} atm^{-1})
N_i	Number of moles of species *i* (kmol)
N_j	Number of moles of species *j* (kmol)
n	Translational quantum number
n_j	Broadening temperature index

P	Total mixture pressure (atm)
p	Pressure (kPa)
p_i	Partial pressure of species *i* (kPa)
p°	Reference pressure (kPa)
$Q(T)$	Partition function
δQ	Heat added to a closed system in an infinitesimal process
R_u	Universal gas constant (kJ/kmol K)
S	Entropy (kJ/kg K)
S_{mix}	Total mixture entropy (kJ/K)
S_i	Absorption linestrength of species *i* (cm^{-2} atm^{-1})
$\bar{s}_i$	Molar entropy of species *i* (kJ/kmol-K)
T	Temperature (K)
T_o	Spectroscopic reference temperature (K)
T_{ref}	Reference temperature (K)
V	Volume (m^3)
δW	Work performed in a closed system in an infinitesimal process
x_i	Mole fraction of species *i*

Greek Symbols

$\Delta\nu_D$	Doppler linewidth
$\Delta\nu_C$	Collisional linewidth
$\Delta\nu_S$	Pressure-induced frequency shift

α_ν	Absorbance at wavenumber ν
γ_i	Self-broadening coefficient (cm^{-1} atm^{-1})
γ_j	Collision-induced broadening coefficient (cm^{-1} atm^{-1})
δ_j	Broadening shifting coefficient (cm^{-1} atm^{-1})
ε_j	Molecular energy at level *j*
ε_j'	Total molecular energy at level *j*
ε_o'	Molecular zero-point energy
ε_{trans}	Translational energy
ε_{rot}	Rotational energy
ε_{vib}	Vibrational energy
ε_{el}	Electronic energy
ε_{trans}'	Total translational energy
$\varepsilon_{trans,o}'$	Zero-point translational energy
ε_{rot}'	Total rotational energy
$\varepsilon_{rot,0}'$	Zero-point rotational energy
ε_{vib}'	Total vibrational energy
$\varepsilon_{vib,o}'$	Zero-point vibrational energy
$\Delta\varepsilon_o$	Change in molecular zero-point energy
μ	Reduced mass
$\bar{\mu}_i$	Chemical potential of species *i* (kJ/kmol)
ν	Wavenumber (cm^{-1})

v_i	Molar coefficient of species *i*
ν_o	Center wavenumber of molecular transition (cm^{-1})
υ	Vibrational quantum number
ϕ	Equivalence Ratio
ϕ_D	Doppler lineshape function
ϕ_C	Lorentzian lineshape function
ϕ_V	Voigt lineshape function

TABLE OF CONTENTS

LIST OF FIGURES

Page

LIST OF TABLES

Page

1. INTRODUCTION

1.1 Motivation and scope

Carbon monoxide (CO) is a product of incomplete combustion in hydrocarbon-fueled systems. CO emissions are heavily influenced by the system's equivalence ratio, operating pressure, and temperature. Within the combustion system, large amounts of CO are found in combustion zones operating fuel-rich due to the lack of oxygen needed to complete the reaction to form carbon dioxide (CO_2). High CO emissions are also found in combustion zones operating fuel-lean due to the dissociation of CO_2 (Lefebvre, 2010). In combustors, CO arises from incomplete combustion due to the inadequate burning rates in the primary zone influenced by the fuel/oxidizer ratio. CO may also increase due to inadequate mixing of the combustible mixture which causes fuel-rich combustion zones that yield high CO concentrations. Accurate concentration measurements of CO are important in any hydrocarbon-based combustion system to quantify its efficiency.

Laser absorption spectroscopy has played a major role in combustion measurements and temperature sensing. Laser spectroscopy techniques offer non-intrusive measurements that can detect the gas composition in the atmosphere and combustion systems as well as other flow-field parameters such as pressure, temperature and velocity. These techniques also offer time-sensitive and *in situ* species measurements that are important for combustion and propulsion applications. Several research groups have studied the absorption transitions of CO in the mid-IR particularly in its overtone bands and fundamental band near 1.55 μm, 2.3 μm, and 4.5 μm,

respectively. One of the major influences in line-selection for CO concentration measurements in combustion systems is its absorption line-strength compared to other major species in combustion. It is important to select a transition line with a high CO absorption line-strength to minimize interference from other major species in combustion such as water (H_2O) and carbon dioxide (CO_2). Extensive studies from the literature have been performed to characterize the broadening nature of CO with major species of combustion as well as common species such as Argon (Ar) that are found in shock-tube experiments.

The scope of this thesis is focused in the development of a mid-IR sensor for time-sensitive carbon monoxide (CO) measurements operating near 4.5 μm using the direct absorption spectroscopy (DAS) technique. The CO absorption line-strengths between the fundamental band and overtone bands were compared for an optimal line selection and are discussed. This mid-IR CO sensor was validated using a shock-heated mixture that contained CO in a shock tube at Texas A&M University. A model was developed to calculate the CO concentration using the CO spectroscopy parameters from the HITRAN Database (Rothman, 2005). This model was validated using the IR absorption measurements taken from the shock-tube experiments.

The mid-IR CO sensor was applied on a high-pressure combustor rig to characterize its performance by measuring CO emissions. The mid-IR sensor was adapted to perform *in situ* CO transient and steady-state measurements to compare the mid-IR diagnostics to other combustion parameters such as equivalence ratio, rig pressure, rig temperature, and other emission diagnostics. The CO concentrations were

measured by applying the DAS technique on a separate absorption cell that allowed the flow of combustion gases to be exposed to the mid-IR laser at a safe distance from the combustor rig test platform. Two mid-IR laser fiber-coupling methods have been proposed for a potentially improved CO measuring technique. These methods are currently under development and are being tested on the combustor rig in order to determine the optimal configuration that provides the highest signal-to-noise (SNR) while isolating the optical equipment from any vibrations during performance tests.

The mid-IR sensor was also adapted to measure unburned hydrocarbons (UHC) using a HeNe laser operating at fixed wavelength of 3.39 μm. This setup with a different laser provided a hydrocarbon fuel-measurement technique independent of the combustor rig conditions to compare with the flame ionization detector (FID) analyzer used to measure the rig's UHCs. The broadening behavior of methane (CH_4) with CO_2 was experimentally determined used for the calibration of the sensor's hydrocarbon fuel-measurement capability.

1.2 Organization of thesis

The present chapter discusses the motivation, scope and objective of the mid-IR diagnostics. Chapter 2 provides the theoretical combustion and spectroscopy background needed for the calculations performed in this thesis and also provides the background of the high-pressure combustor rig as well as its on-going testing program. Chapter 3 provides detailed information of the equipment and experimental apparatus that was used for the analysis presented in this thesis. Chapter 4 goes over the experimental

procedure taken for every diagnosis using the mid-IR sensor, and Chapter 5 provides the results and discussion. Chapter 6 summarizes the work done and provides the conclusion and recommendations for the mid-IR sensor capability.

2. BACKGROUND

This section is intended to give a background in the on-going combustor rig performance tests as well as the theory used for the analysis presented in this thesis. The rig objective and operability are presented to give an understanding of what is being tested and the reason behind it. Combustion and thermodynamic concepts are presented in a straightforward manner by presenting a simplified hydrocarbon-combustion example along with a brief thermodynamic summary for chemical equilibrium. This concept is important and necessary in the comparison of species mole fractions at equilibrium conditions. Finally, an overview of laser absorption spectroscopy and molecular spectroscopy is presented to understand the design and development of the mid-IR diagnostics.

2.1 Combustor objective and operability

The combustor rig is part of a ground-breaking test program for a new thermal power plant that will use supercritical carbon dioxide (CO_2) as the working fluid to produce low-cost electricity while eliminating emissions of nitrogen oxides (NOx), CO_2, and other pollutants. The turbomachinery of this new power plant is currently being engineered by Toshiba, and the high-pressure combustor was engineered and manufactured by the cooperation between Toshiba and Parametric Solutions Inc. (PSI). The combustor rig performance tests are being conducted at the Wyle Fluids Laboratory in San Bernardino, CA. The objective of the combustor rig performance tests are to

demonstrate stable combustion at high pressures up to 300 atmospheres using a mixture of natural gas, O_2, and a high concentration of CO_2 as the reactants. Many rig performance tests have been conducted at different conditions over the past year to demonstrate stable combustion at different pressure increments up to 300 atmospheres.

2.2 Hydrocarbon combustion and chemical equilibrium

Figure 1 illustrates a simplified schematic of a combustor. A reactant mixture of hydrocarbon C_xH_y and air enter the combustion chamber as the products of combustion exit the combustion chamber.

Figure 1 Simplified schematic of a combustion chamber using hydrocarbon C_xH_y as the fuel and air as the oxidizer.

The stoichiometric quantity of oxidizer is just the amount needed to completely burn a quantity of fuel. The stoichiometric relation for a hydrocarbon fuel given as C_xH_y is expressed as Eq. 1:

$$C_xH_y + a(O_2 + 3.76N_2) \rightarrow xCO_2 + (y/2)H_2O + 3.76aN_2 \quad (1)$$

where the number of moles of air, a, is given by the following relation:

$$a = x + {}^{y}/_{4} \tag{2}$$

At real engine conditions, the relation may be far from stoichiometric, resulting in incomplete combustion. The relation shown as Eq. 3 expresses a real combustion process:

$$C_xH_y + a(O_2 + 3.76N_2) \rightarrow bCO_2 + cH_2O + 3.76dN_2 + eCO + fO_2 + hC_xH_y \ldots \tag{3}$$

where the products of combustion will contain more than just water and carbon dioxide. The mixture is lean if more than the stoichiometric quantity of air, or oxidizer, is used. For a quantity of oxidizer less than the stoichiometric oxidizer quantity, the mixture is known as a rich mixture .As shown from the relations above, the product composition depends on the reactant composition. For a stoichiometric mixture using air, the air-to-fuel ratio is given as:

$$\left({}^{A}/_{F}\right)_{stoic} = \left(\frac{m_{air}}{m_{fuel}}\right)_{stoic} = \frac{4.76a}{1}\frac{MW_{air}}{MW_{fuel}} \tag{4}$$

where MW_{air} is the molecular weight of air [g/mol] and MW_{fuel} is the molecular weight of the fuel [g/mol)]. The equivalence ratio is defined as the ratio between the stoichiometric air-to-fuel ratio to the real air-to-fuel ratio expressed as the following:

$$\varphi = \frac{\left({}^{A}/_{F}\right)_{stoic}}{\left({}^{A}/_{F}\right)} = \frac{\left({}^{F}/_{A}\right)}{\left({}^{F}/_{A}\right)_{stoic}} \tag{5}$$

The general equivalence ratio for a combustion system using a fuel and oxidizer is given as:

$$\varphi = \frac{\left({}^{Ox}/_{F}\right)_{stoic}}{\left({}^{Ox}/_{F}\right)} = \frac{\left({}^{F}/_{Ox}\right)}{\left({}^{F}/_{Ox}\right)_{stoic}} \tag{6}$$

The equivalence ratio is a useful parameter to indicate how far the system is operating from stoichiometric and is used to characterize combustor performance. For gas turbine engines, the air-to-fuel ratio can be approximately 15:1 since a high dilution is required to maintain the temperature dictated by the first-stage turbine nozzle (Saravanamutto, 2001). Figure 2 illustrates the equilibrium composition of major product species and the adiabatic flame temperature as a function of equivalence ratio for CH_4-air combustion at 1 atm.

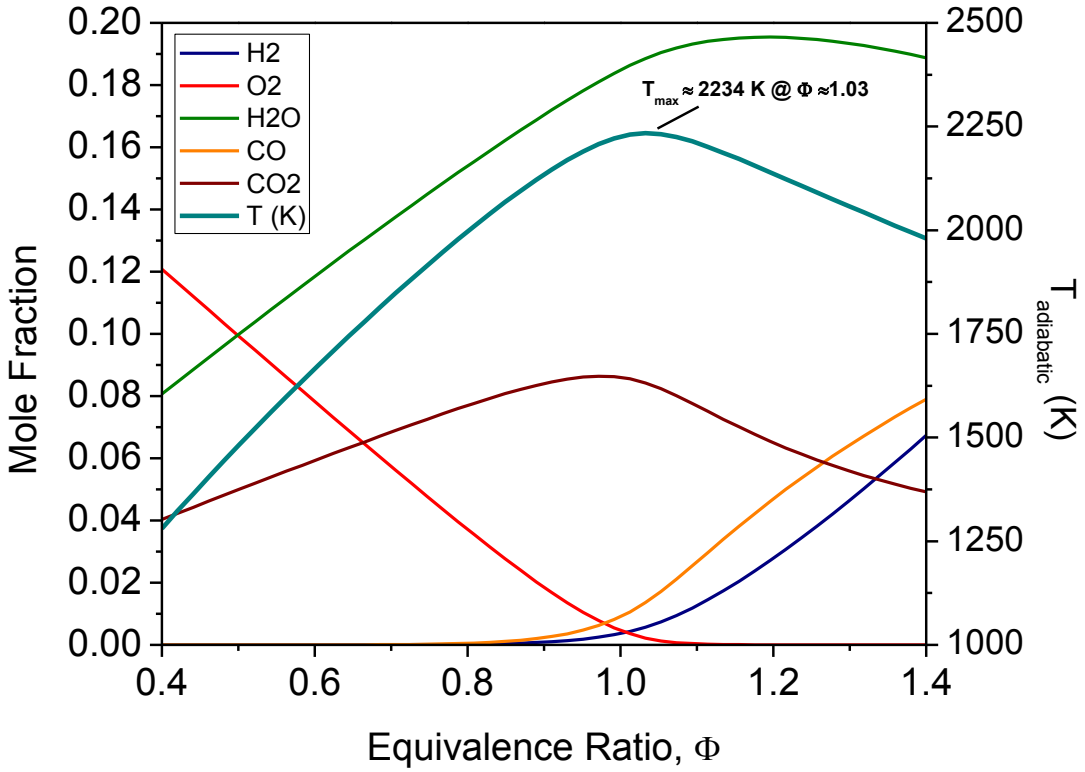

Figure 2 Equilibrium adiabatic flame temperature with major products for CH_4-air combustion at 1 atm.

2.2.1 Criterion for chemical equilibrium

During a combustion process, the major species of combustion such as H_2O, CO_2, and N_2 may dissociate depending on the combustion conditions. The dissociation of these major species can result in a host of minor species such as CO, OH O, N, NO, etc. With a fuel-rich mixture ($\Phi>1$), the products of combustion will contain a portion of unburned hydrocarbons (UHC) due to the lack of oxidizer to completely burn the hydrocarbon fuel. On the other hand, a lean-mixture ($\Phi<1$) will contain a larger portion

of the oxidizer due to its quantity in the reactants being higher than what is needed to completely burn the fuel. A simple atom balance will not determine the correct mole fractions for all products of combustion in a real combustion process. The mole fractions of all the product species can be calculated by a chemical equilibrium analysis. The equilibrium composition of a mixture can be determined by combining the first and second law of thermodynamics. Depending on the constraints of the system, a mass or molar-based property can be analyzed to determine the equilibrium composition. The derivations below demonstrate the chemical equilibrium criteria, depending on the system's constraints.

For a closed system with a fixed mass, the first law of thermodynamics, the heat added to the system, δQ, is equal to the summation of the change in the system's internal energy, dE, and the change in the amount of boundary work done, δW:

$$\delta Q = dE + \delta W = dE + pdV \tag{7}$$

where the heat and work are path dependent while the internal energy, E, is an exact differential because it is a property of the system. The second law of thermodynamics can be written in terms of the system's entropy, S, and the temperature for an infinitesimal process in a closed system as Eq. 8:

$$TdS \geq 0 \tag{8}$$

The inequality shown in Eq. 8 holds for all irreversible processes. Eq. 8 equals to zero for a reversible process. Eq. 7 and Eq. 8 can be combined to form the following:

$$dE \leq TdS - pdV \tag{9}$$

Eq. 9 implies that the system's internal energy, E, can be expressed as a function of two independent variables such as S and V when considering the boundary work. When a system contains multiple components, the internal energy must also be expressed as a function of the composition. The composition can be specified by the number of moles of the species *i* on a molar bases. Therefore, the internal energy of a system of multiple components can be expressed as:

$$E = E(S, V, N_i) \tag{10}$$

where N_i represents the number of moles of species *i*. The system's internal energy can be differentiated shown as Eq. 11:

$$dE = \left(\frac{\partial E}{\partial S}\right)_{V,N_i} dS + \left(\frac{\partial E}{\partial V}\right)_{S,N_i} dV + \sum_{i=1}^{N} \left(\frac{\partial E}{\partial N_i}\right)_{S,V,N_{j(j\neq 1)}} dN_i \tag{11}$$

When comparing Eq.11 with Eq. 9, the partials can be expressed as the system's temperature, pressure, and chemical potential represented as Eq. 12:

$$T = \left(\frac{\partial E}{\partial S}\right)_{V,N_i}, \quad p = -\left(\frac{\partial E}{\partial V}\right)_{S,N_i}, \quad \bar{\mu}_i = \left(\frac{\partial E}{\partial N_i}\right)_{S,V,N_{j(j\neq 1)}} \tag{12}$$

Each derivative shown above represents the partial derivative of the system's internal energy with respect to the independent variable while holding all the other variables constant. The chemical potential of species *i* represents the molar free energy contribution to the system from species *i*. It is defined as the partial of the system's internal energy with respect to the number of moles of species *i* while holding entropy,

volume and the number of moles of all the other species constant. Therefore, Eq. 11 can be written as the following:

$$dE = TdS - pdV + \sum_{i=1}^{N} \bar{\mu}_i \, dN_i \tag{13}$$

Eq. 13 can be rewritten depending on the natural variables of interest that constrain the system. Eq. 13 can be written in terms of the enthalpy, $H=E+PV$, for an open system as:

$$dH = TdS + VdP + \sum_{i=1}^{N} \bar{\mu}_i dN_i \tag{14}$$

It is also convenient to express Eq. 13 in terms of the Helmholtz function, $A=E-TS$, or the Gibbs function, $G=H-TS$ as shown as Eq. 15 and Eq. 16, respectively:

$$dA = -SdT - PdV + \sum_{i=1}^{N} \bar{\mu}_i dN_i \tag{15}$$

$$dG = -SdT - VdP + \sum_{i=1}^{N} \bar{\mu}_i dN_i \tag{16}$$

Typical problems for chemical equilibrium require the need to calculate the mixture composition at a given pressure and temperature. A good example is calculating the equilibrium product composition for a combustor. As mentioned above, the chemical potential represents the molar free energy of species i and can be defined as the partial of a molar-based extensive property with respect to the number of moles of species i, N_i:

$$\bar{\mu}_i = \left(\frac{\partial H}{\partial N_i}\right)_{S,p,N_{j(j\neq 1)}} = \left(\frac{\partial A}{\partial N_i}\right)_{T,V,N_{j(j\neq 1)}} = \left(\frac{\partial G}{\partial N_i}\right)_{T,p,N_{j(j\neq 1)}} = \bar{g}_i \tag{17}$$

Combining Eq. 9 and Eq. 13 results in the following criterion:

$$\sum_{i=1}^{N} \bar{u}_i dN_i \leq 0 \tag{18}$$

where the inequality holds for an irreversible process, while equality holds when the system reaches equilibrium:

$$\sum_{i=1}^{N} \bar{u}_i dN_i = 0 \tag{19}$$

The general criterion given as Eq. 19 can be applied to *E, H, A*, or *G* defined above to find the state of each property at equilibrium. The extensive properties defined above can be used to determine the reaction direction for any chemically reacting process and are related by the summation of the product of the chemical potential and change in moles during reaction for each species within the mixture:

$$-TdS_{E,V,N_i} = dE_{S,V,N_i} = dH_{S,P,N_i} = dA_{T,V,N_i} = dG_{T,P,N_i} = \sum \mu_i dN_i = 0 \tag{20}$$

2.2.2 Chemical equilibrium for an ideal gas

The entropy for an ideal gas is defined as the following:

$$ds = c_{p,o} \frac{dT}{T} - R_u \frac{dP}{P} \tag{21}$$

where *ds* is the change in entropy, $c_{p,o}$, is the specific heat, T is the temperature, R_u is the universal gas constant and *P* is the pressure. For an ideal mixture, the change in entropy for species *i* is simplified to the following:

$$d\bar{s}_i = \bar{s}_i(T,P) - \bar{s}_i\left(T_{ref}, P^\circ\right) = \bar{s}_i^\circ(T) - R_u ln\left(\frac{P_i}{P^\circ}\right) \tag{22}$$

where the entropy of formation is defined as the following using the specific heat of species *i* on a molar basis:

$$\bar{s}_i^{\circ}(T) = \int_{T_{ref}}^{T} \bar{c}_{p,i} \frac{dT}{T} \tag{23}$$

The total entropy of the ideal mixture is defined as the summation of the entropies of each species multiplied by their number of moles:

$$S_{mix}(T,P) = \sum_{i=1}^{L} N_i \bar{s}_i \tag{24}$$

Similarly, the total enthalpy of a mixture is composed of the enthalpies of each species along with their number of moles:

$$H_{mix}(T,P) = \sum_{i=1}^{L} N_i \bar{h}_i \tag{25}$$

where the total enthalpy of species *i* is composed of the enthalpy of formation, $h^o_{f,i}$, and the sensible enthalpy represented by the integral with respect to the temperature. The reference temperature is typically taken to be 298 K.

$$\bar{h}_i(T) = \bar{h}_{f,i}^{\circ} + \int_{T_{ref}}^{T} \bar{c}_{p,i}\, dT \tag{26}$$

For a system with constant pressure, *P*, temperature, *T*, and mass, m, it is useful to combine the ideal mixture's properties in the form of the Gibbs free energy:

$$G = H - TS \tag{27}$$

The Gibbs function for a mixture of ideal gases can be expressed as:

$$G_{mix} = \sum N_i \bar{g}_{i,T} = \sum N_i \left[\bar{g}_{i,T}^{\circ} + R_u T ln\left({}^{P_i}/_{P^{\circ}} \right) \right] \tag{28}$$

where Ni is the number of moles for species i, $g^o_{i,T}$ is the Gibbs function of formation and P_i is the partial pressure of species i, and P^o is the reference pressure usually taken as 1 atm. The equilibrium constant K_P for an ideal gas can be defined as Eq. (30) for the general sub-reaction shown below:

$$aA + bB + \cdots \leftrightarrow dD + eE + \cdots \tag{29}$$

$$K_P = \frac{\left({P_D}/{P^\circ}\right)^d \cdot \left({P_E}/{P^\circ}\right)^e \cdots}{\left({P_A}/{P^\circ}\right)^a \cdot \left({P_B}/{P^\circ}\right)^b \cdots} \tag{30}$$

The equilibrium constant is a useful parameter that can be used to determine the equilibrium mole fractions for the reaction under consideration. For a reaction of a mixture of ideal gases at chemical equilibrium at constant temperature and pressure, the equilibrium constant can be related to the Gibbs function of formation of each species by the following expressions:

$$\Delta G^\circ_T = -R_u T ln\left(K_p\right) \tag{31}$$

$$K_p = exp\left({-\Delta G^\circ_T}/{R_u T}\right) \tag{32}$$

The equilibrium constant for the reaction shown below can be expressed as Eq. (34) assuming an ideal gas mixture:

$$CO + {1}/{2}\, O_2 \Leftrightarrow CO_2 \tag{33}$$

$$K_p = \frac{\left(P_{CO}/P^{\circ}\right)\left(P_{O_2}/P^{\circ}\right)^{1/2}}{\left(P_{CO_2}/P^{\circ}\right)} \tag{34}$$

The mole fractions of each species can be determined when Eq. (32) and Eq. (34) are combined to form the following:

$$\frac{x_{CO}x_{O_2}^{0.5}}{x_{CO_2}}\left(\frac{P}{P^{\circ}}\right)^{0.5} = exp\left[\frac{-\Delta G_T^{\circ}}{R_u T}\right] \tag{35}$$

An additional two equations are needed to solve Eq. (35) since there are a total of three species. The second and third equations can be derived by performing a conservation of elements as well as summing the mole fractions to unity.

2.3 Laser absorption spectroscopy

2.3.1 Absorption and emission spectra

A molecule can experience induced absorption, spontaneous emission or induced (stimulated) emission when it is subjected to radiation of frequency v corresponding to an energy separation defined as:

$$\Delta E = E_u - E_l = h_p v \tag{36}$$

where E_u is the upper energy state, $E_l$is the lower energy state, and h_p is Planck's constant $[6.62607 \times 10^{-34} J\ s]$. The upper and lower energy states that define the

molecular transition can be translational, rotational, vibrational, or electronic. The molecular transition undergoing these three processes is illustrated in Figure 3:

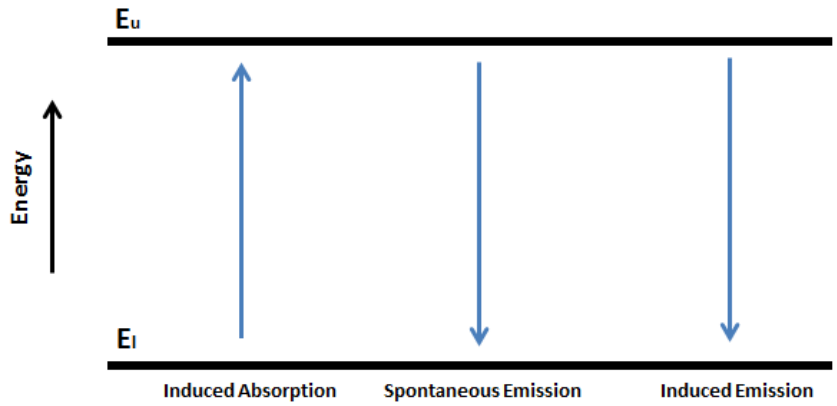

Figure 3 Absorption and Emission between energy states E_u and E_l for an atom or molecule. The radiation takes place between stationary states *u* and *l*.

Eq. (36) can also be written as a function of *c*, the speed of light [$2.998 \times 10^8\ m/s$], and λ, wavelength [m]:

$$\Delta E = h_p v = h_p \frac{c}{\lambda} \tag{37}$$

If a source of radiation passes through a gaseous molecular sample, molecules in the lower state E_l absorb radiant power and undergo a molecular transition characterized by Eq. (37). The difference in the spectral distributions between the incident and the transmitted power is known as the absorption spectrum of the molecular sample. The resulting absorption spectrum is a discrete absorption spectrum if the ΔE energy states

are bound levels. Discrete absorption or emission spectra are never monochromatic (Demtröder, 1996). Each spectral line has a spectral distribution around the central frequency, ν_o, as shown in Figure 4. The half width, or Full Width at Half Maximum (FWHM), is represented as $\Delta\nu$. This spectral distribution corresponds to the molecular transition with the bound energy difference $\Delta E = E_u - E_l$.

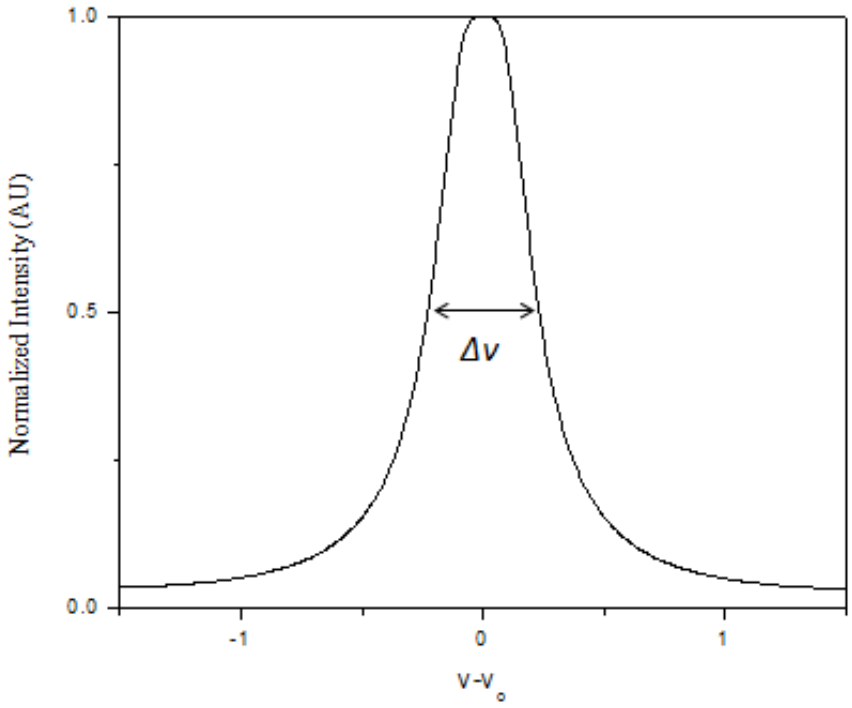

Figure 4 Line profile of a spectral line with normalized intensity units (AU).

2.3.2 Widths and spectral lineshapes

An absorption or emission transition is affected by physical mechanisms that perturb its energy levels. These physical mechanisms are known as broadening effects and affect the way the absorbing or emitting molecules interact with the radiative energy. In the case of an absorbing molecule, the broadening effects dictate the line profile of its spectral line when interacting with a light source such as a laser beam. There are several broadening effects that can influence a spectral line profile, but only Doppler and collisional broadening were considered for the absorption measurements in this work. Other broadening mechanisms such as collisional narrowing (Dicke narrowing) or saturation broadening are significant in other applications and can be described by (Demtröder, 1996).

Doppler broadening is due to the thermal motion of the absorbing molecules. Doppler broadening causes the central frequency, ω_o, to shift when a molecule has a velocity component in the same direction as the laser propagation. This broadening effect and shift in frequency caused by the random thermal motion of the molecule produces a Gaussian profile with a lineshape function defined as:

$$\phi_D(v) = \frac{2}{\Delta v_D}\sqrt{\frac{ln2}{\pi}}\,exp\left[-4ln2\left(\frac{v-v_o}{\Delta v_D}\right)^2\right] \tag{38}$$

The Doppler linewidth, Δv_D [cm^{-1}], of the spectral line caused by this Gaussian profile is defined as Eq. (39) where v_o [cm^{-1}] is the central frequency, T [K] is the temperature and m [g/mol] is the molecular weight of the absorbing species.

$$\Delta v_D = 7.16 \times 10^{-7} v_o \sqrt{\frac{T}{m}} \tag{39}$$

Collisional (pressure) broadening is caused by shifts in energy levels due to molecular collisions. The energy levels of the absorbing molecule, *i*, are shifted when it collides by a molecule, *j*. This energy level shift depends on the electron configuration of the absorbing species and collisional partner. The collisional-broadened lineshape function takes the form of a Lorentzian profile and is defined as Eq. 40 and collisional linewidth, Δv_C [cm^{-1}], caused by pressure broadening defined as Eq. 41:

$$\phi_C(v) = \frac{\Delta v_c/2}{\pi[(v - v_o - \Delta v_s)^2 + (\Delta v_c/2)^2]} \tag{40}$$

$$\Delta v_c = P \sum_j X_j 2\gamma_i \tag{41}$$

where P [atm] is the total mixture pressure, X_j is the mole fraction of the collisional partner, j, and γ_i [cm^{-1}atm^{-1}] is the self-broadening coefficient. The self-broadening coefficient depends on the collisional partner and is a function of temperature; it can be scaled to the proper temperature when expressed as Eq. (42):

$$\gamma_j(T) = \gamma_j(T_o) \left(\frac{T_o}{T}\right)^{n_j} \tag{42}$$

where To [K] is the reference temperature, usually taken as 296 K (Rothman, 2005), and n_j is known as the temperature index. Pressure broadening also causes a line-center shift, $v_o + \Delta v_s$. The pressure-induced frequency shift, Δv_s [cm^{-1}], is defined as:

$$\Delta v_s = P \sum_j X_j \delta_j \tag{43}$$

where δ_j [$cm^{-1}atm^{-1}$] is the shifting coefficient. Note that both the collisional linewidth and pressure-induced shift are proportional to the total mixture pressure. The shifting coefficient depends on the collisional partner, j, and can be scaled to the appropriate temperature by Eq. (44):

$$\delta_j(T) = \delta_j(T_o)\left(\frac{T_o}{T}\right)^{m_j} \tag{44}$$

Doppler broadening is dominant in gases at low pressures, while collisional broadening dominates at high pressures. The natural linewidth of the spectral line, which has a Lorentzian line profile, is difficult to measure without special techniques since the spectral line is concealed by other broadening effects. Doppler and collisional broadening have significant contributions in many spectroscopy applications. Therefore, it is necessary to determine a lineshape function that will take into account these significant broadening mechanisms. The overall lineshape can be expressed as a Voigt profile which is a convolution of the Gaussian and Lorentzian lineshapes. Eq. (45) defines the lineshape function for a Voigt profile:

$$\phi_V(v) = \left[\frac{\sqrt{(4ln2/\Pi)}}{\Delta v_D}\right] \times V(w, a_v) \tag{45}$$

where $V(w,a_V)$ is the normalized Voigt function and is a function of two non-dimensional parameters defined as the following:

$$w = 2\sqrt{ln2}\,\frac{v - v_o - \Delta v_s}{\Delta v_D} \tag{46}$$

$$a_v = \sqrt{ln2}\frac{\Delta v_c}{\Delta v_D} \tag{47}$$

Figure 5 illustrates the broadening and shifting effects of pressure for a CO/air mixture and neat CO at 300 K.

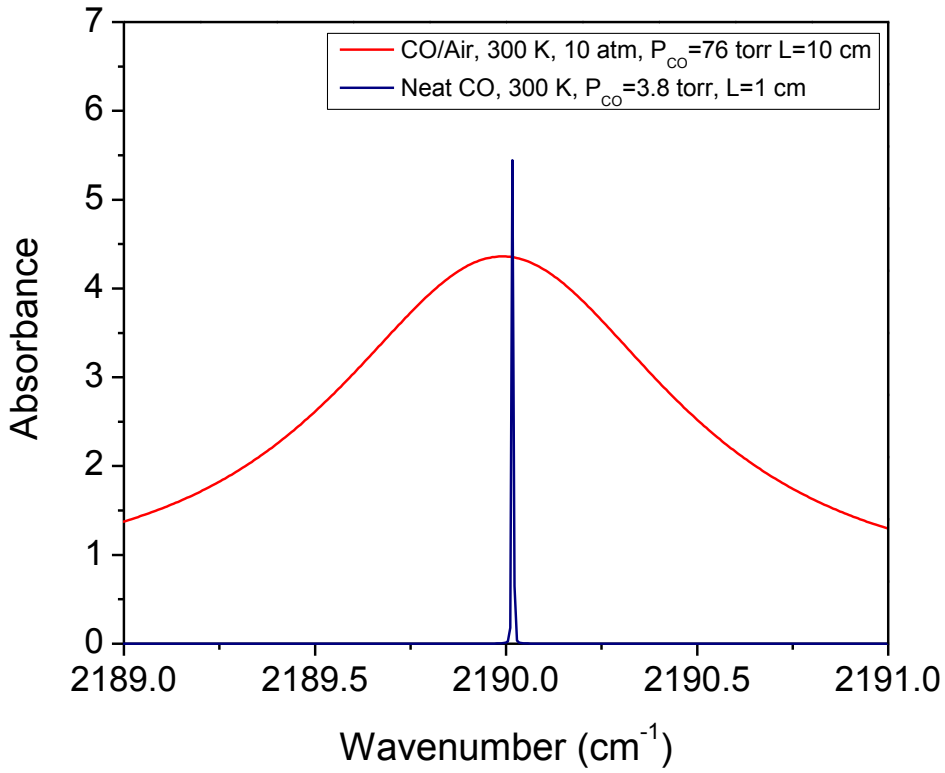

Figure 5 Illustration of the pressure-induced broadening and shifting for CO/air and neat CO at 300 K with different absorption path lengths.

2.3.3 Beer-lambert law

Direct absorption spectroscopy (DAS) is a technique that relates the attenuation of laser intensity along a fixed path to the absorbance of a gas species. Similar to modulation spectroscopy, the DAS technique plays a big role in combustion applications as well as the measurement of flow parameters such as gas composition, temperature and pressure. This absorption technique can be represented by the Beer-Lambert law.

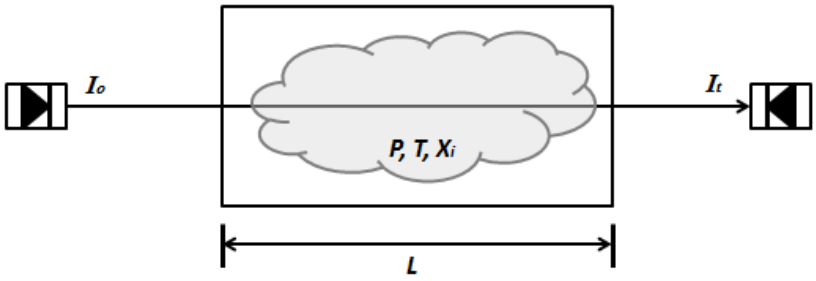

Figure 6 Simplified schematic for direct absorption spectroscopy measurements. The absorbance path length, L, is the total length in which the species *i* absorbs energy.

A collimated laser beam with intensity I_o passes through a uniform gas sample with a fixed length L as shown in Figure 6. The laser energy is absorbed when the laser frequency v [cm^{-1}] is resonant with the frequency of a transition line of the absorbing species within the gas mixture. The laser intensity attenuation is related to the absorbance of species *i* by the Beer-Lambert law:

$$\left(\frac{I_t}{I_o}\right)_v = exp[-k_v(T,P)X_iPL] \tag{48}$$

where I_t is the transmitted intensity after the beam passes through the gas sample, and the absorption coefficient is defined as:

$$k_v(T,P) = S_i(T)\phi_v \tag{49}$$

where S [cm^{-2} atm^{-1}] is the absorption line-strength of the specific species transition, P [atm] is the total pressure, x_i the mole fraction of the absorbing species i, and $\emptyset(v)$ [cm] the line-shape function. The absorbance is defined as the dimensionless product:

$$\alpha_v = -ln\left(\frac{I_t}{I_o}\right) = S_i(T)\phi_v X_i P L \tag{50}$$

The line-shape function, $\emptyset(v)$, is normalized to have unit area across the spectral line which defines the integrated absorbance as:

$$A_i = \int \alpha_v dv = S_i(T)\phi_v X_i P L \tag{51}$$

As shown above, the integrated absorbance can be reduced to the product of the species absorption line-strength, partial pressure, and path length. The absorption line-strength is defined as:

$$S_i(T) = S_i(T_o)\frac{Q(T_o)}{Q(T)} exp\left[-\frac{h_p c E''}{k}\left(\frac{1}{T}-\frac{1}{T_o}\right)\right]\frac{\left[1-exp\left(-\frac{h_p c v_o}{kT}\right)\right]}{\left[1-exp\left(-\frac{h_p c v_o}{kT_o}\right)\right]} \tag{52}$$

where $Q(T)$ is the partition function, E'' [cm^{-1}] is the lower-state energy, v_o [cm^{-1}] is the line-center frequency, h_p is Planck's constant, c is the speed of light, and k is the Boltzmann's constant.

2.3.4 Partition functions and molecular energy modes

The partition function represents the total energy allocated to each energy mode and is defined as:

$$Q(T) = \sum_j g_j e^{-\varepsilon_j/kT} \tag{53}$$

where g_j is the statistical weight, or degeneracy, of a given energy level j. The statistical weight represents the number of different states, or different molecular orientations, in the same energy level. Energy levels exist as a result of quantum mechanics stating that each energy mode can only exist at certain discrete values, that is, they are quantized. The total energy of a molecule is defined as the sum of its translational, rotational, vibrational, and electronic energies:

$$\varepsilon' = \varepsilon'_{trans} + \varepsilon'_{rot} + \varepsilon'_{vib} + \varepsilon'_{el} \tag{54}$$

where the subscript denotes the summation of the energies in energy level j with their corresponding zero-point energies, ε'_o, defined as Eq. (55):

$$\varepsilon'_j = \varepsilon_{trans} + \varepsilon_{rot} + \varepsilon_{vib} + \varepsilon_{el} + \varepsilon'_o \tag{55}$$

Therefore, the energy of the molecule in energy level j is defined as:

$$\varepsilon_j = \varepsilon'_j - \varepsilon'_o = \varepsilon_{trans} + \varepsilon_{rot} + \varepsilon_{vib} + \varepsilon_{el} \tag{56}$$

For the translational energy mode, the total energy can be defined as:

$$\varepsilon'_{trans} = \frac{h_p^2}{8m}\left(\frac{n_1^2}{a_1^2} + \frac{n_2^2}{a_2^2} + \frac{n_3^2}{a_3^2}\right) \tag{57}$$

where h_p is the Planck's constant and m is the molecular weight. The coefficients n_1, n_2, and n_3 are quantum numbers that can take integral values. The lowest quantum number defines the ground state and zero-point energy. The coefficients a_1, a_2, and a_3 are dimensions that describe the overall size of the system. The zero-point energy of translation, $\varepsilon'_{trans,0}$, is very small to where it can be approximated as zero:

$$\varepsilon'_{trans,o} \approx 0 \tag{58}$$

Therefore, the translational energy above the zero-point energy is defined as:

$$\varepsilon_{trans} \approx \frac{h_p^2}{8m}\left(\frac{n_1^2}{a_1^2}+\frac{n_2^2}{a_2^2}+\frac{n_3^2}{a_3^2}\right) \tag{59}$$

From Eq. (53), the partition function is taken as the summation of all energy states. Therefore, the translational partition function is defined as:

$$Q(T)_{trans} = \sum_j g_{j,trans} exp\left(-\frac{\varepsilon_{j,trans}}{kT}\right) \tag{60}$$

For the rotational energy mode, the total energy is defined as:

$$\varepsilon'_{rot} = \frac{h_p^2}{8\pi^2 I} J(J+1) \tag{61}$$

where J is the rotational quantum number (J=0,1,2,3, etc.), and I is the molecule's moment of inertia [kg m^2]. The zero-point energy of rotation is zero, and the energy above the zero-point energy is defined as:

$$\varepsilon'_{rot,0}=0 \tag{62}$$

$$\varepsilon_{rot} = \frac{h_p^2}{8\pi^2 I} J(J+1) \tag{63}$$

Using the quantum mechanical results $g_J = 2J + 1$ and replacing the summation by an integral (Anderson, 2006), the partition function for rotation is defined as:

$$Q(T)_{rot} = \frac{8\pi^2 IkT}{h_p^2} \tag{64}$$

For vibration, the total energy is defined as:

$$\varepsilon'_{vib} = h_p \nu \left(\upsilon + \frac{1}{2}\right) \tag{65}$$

where υ is the vibrational quantum number (υ = 0,1,2,3, etc.), and ν is the fundamental vibrational frequency of the molecule. The zero-point energy and energy above the zero-point energy for vibration are defined as:

$$\varepsilon'_{vib,o} = \frac{1}{2} h_p \nu \tag{66}$$

$$\varepsilon_{vib} = \upsilon h_p \nu \tag{67}$$

For the vibrational partition function, quantum mechanics dictates that the statistical weight for all energy levels of a diatomic molecule, g_n, is equal to one:

$$Q(T)_{vib} = \frac{1}{1 - exp\left(-\frac{h\nu}{kT}\right)} \tag{68}$$

The electronic energy and partition function are left out of this discussion due to the ground-state molecular analysis of this thesis. The total partition function is the combination of the partition functions of each mode of energy shown below:

$$Q(T) = Q(T)_{trans} Q(T)_{rot} Q(T)_{vib} \tag{69}$$

As described above, knowing the information of each mode of energy of a molecule allows for the calculation of the partition function and hence the absorption line-strength, *S(T)*, at temperature *T*. The equilibrium constant defined as Eq. (32) can also be expressed as a function of the total partition function:

$$K_p = \left(\frac{kT}{V}\right)^{\sum v_i} exp\left(-\frac{\Delta\varepsilon_o}{kT}\right) \prod_i Q(T)_i^{v_i} \tag{70}$$

where *V* is the total volume of the system and $\Delta\varepsilon_o$ is the change in zero-point energy. Eq. (70) expresses the relation between chemical equilibrium and statistical thermodynamics and can be applied to harsh conditions where it is necessary to analyse the different modes of energy to calculate thermodynamic properties and chemical composition.

2.3.5 Vibrational spectroscopy and infrared spectra

The discussion of vibrational spectroscopy and infrared spectra will be limited to diatomic molecules since the main objective for this thesis is to analyze the diatomic molecule carbon monoxide, CO. As shown in the previous section, the vibrational energy is expressed as Eq. (65). For diatomic molecules, the vibrational frequency can be expressed as Eq. (71), where k_f is the force constant $[aJ\ \dot{A}^{-2}]$ and μ is the reduced mass. The reduced mass is given by Eq. (72), where m_1 and m_2 are the masses of the atoms that make up the diatomic molecule.

$$\nu = \frac{1}{2\pi}\left(\frac{k_f}{\mu}\right)^{1/2} \tag{71}$$

$$\mu = \frac{m_1 m_2}{(m_1+m_2)} \tag{72}$$

The force constant represents the strength of the bond for molecular vibration. Examples of diatomic molecules include O_2, CO, N_2, and NO. Figure 7 illustrates a plot of potential energy, *E*, as a function of bond length, *R*. Figure 7 also illustrates the vibrational energy levels of a molecule.

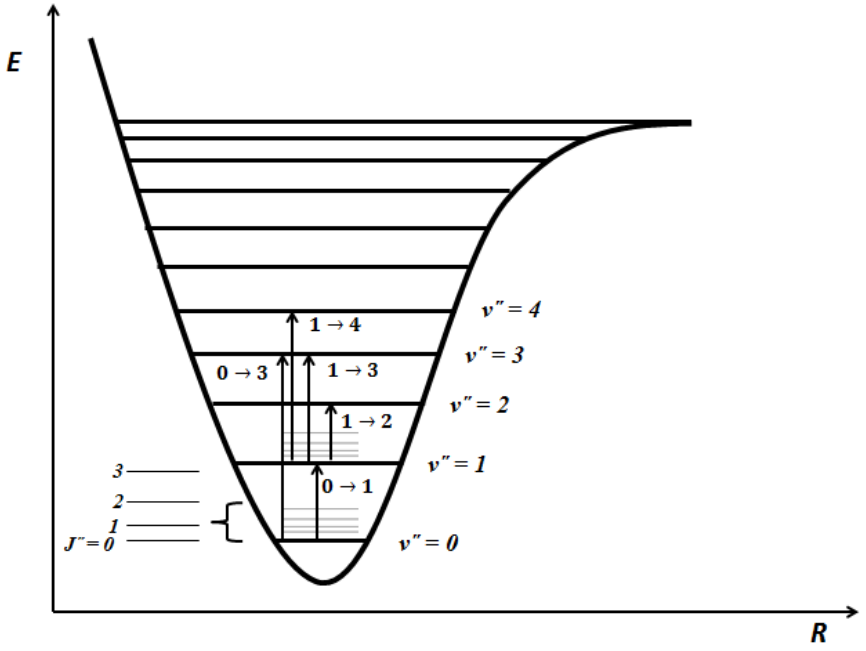

Figure 7 Potential energy v. bond length including vibrational (υ) and rotational (J) energy levels in the electronic ground state.

A vibrational transition is represented as a vibrational band. The transition υ = 0 to υ = 1 ($0 \rightarrow 1$) corresponds to the fundamental band. Transitions from $0 \rightarrow n$ with $n > 1$ are known as overtone bands and $1 \rightarrow n$ with $n < 1$ as hot bands. These transitions can also be expressed using the vibrational selection rule (Δυ = ±1) such as $\Delta v'' = 1$ for the fundamental band, where $\Delta v'' = v''(upper) - v''(lower)$ (Hollas, 2005). Transition lines refer to the transition between two rotational levels within the two given vibrational levels which create the structure of a band.

Vibrational-rotational spectroscopy refers to transitions between rotational energy levels associated with two different vibrational levels. The combination of using the vibrational rule (Δυ = ±1) and the rotational selection rule that governs the rotational transitions between to vibrational energy levels (ΔJ = ±1) gives rise to what is known as the R branch (ΔJ = +1) and the P branch (ΔJ = -1) when a diatomic molecule contains rotational and vibrational energy. Each of these transitions is labeled as *R(J)* or *P(J),* where *J* is understood to be the lower state value, J''. The band center, which is forbidden, is positioned when the selection rule is $\Delta J = 0$ meaning that the pure vibrational transition is not observed. There are some molecules that have an exception to this selection rule which is beyond the scope of this thesis. Selected transitions can be expressed as (ν″, J'') indicating the vibrational and rotational ground levels.

2.3.6 CO absorption spectroscopy

Figure 8 illustrates the absorption line-strength, *S(T)*, for CO at 300 K from 1 to 6 μm. The line-strength was calculated using the 2004 HITRAN database (Rothman, 2005). CO is shown to have noticeable absorption between 4.3 and 5.5 μm with a peak absorption line-strength near 4.5 μm. This peak is near the fundamental band ($\Delta v = 1$) at 4.566 μm (2190.02 cm^{-1}). Noticeable absorption is also shown close to 2.5 μm with a local peak near 2.3 μm corresponding to the first overtone band ($\Delta v = 2$) near 2.3 μm. Figure 9 and Figure 10 illustrate the absorption line-strength for CO_2 and H_2O at 300 K from HITRAN. The absorption line-strength of CO near 4.5 μm is more than 2 orders of magnitude higher than the absorption line-strength of H_2O near 4.5 μm. CO_2 does not show noticeable absorption at that wavelength but has a peak about 2 orders of magnitude higher compared to CO near 4.2 μm. Careful selection of the operating wavelength is needed to minimize any absorption interference from other species.

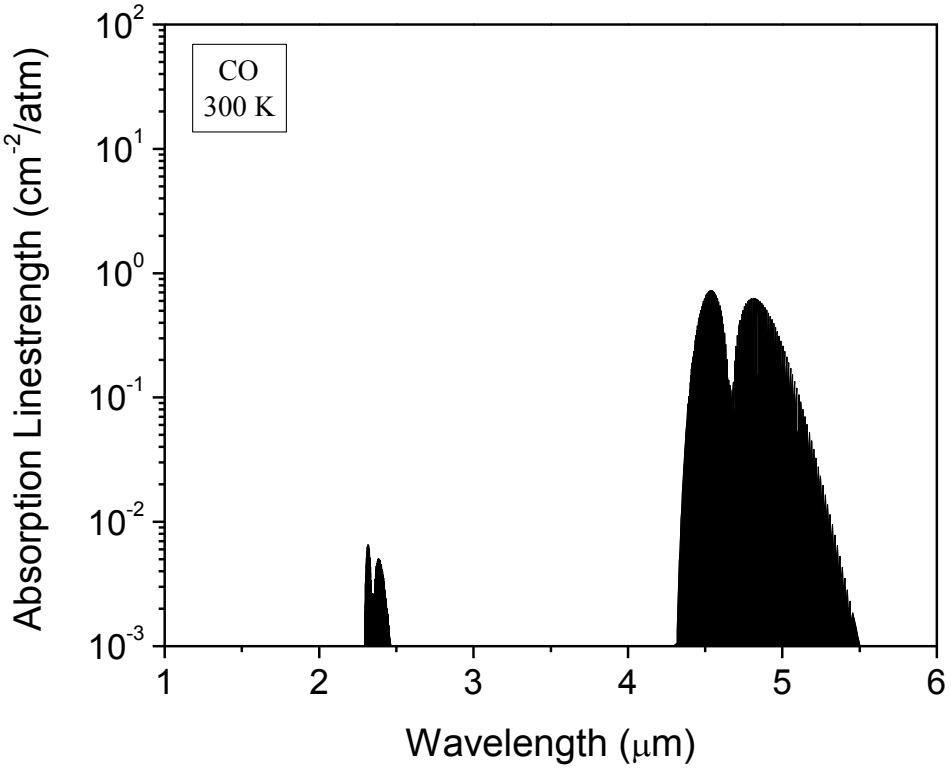

Figure 8 CO absorption line-strengths at 300 K in the IR region from 1 – 6 μm. Taken from HITRAN 2004 database (Rothman, 2005).

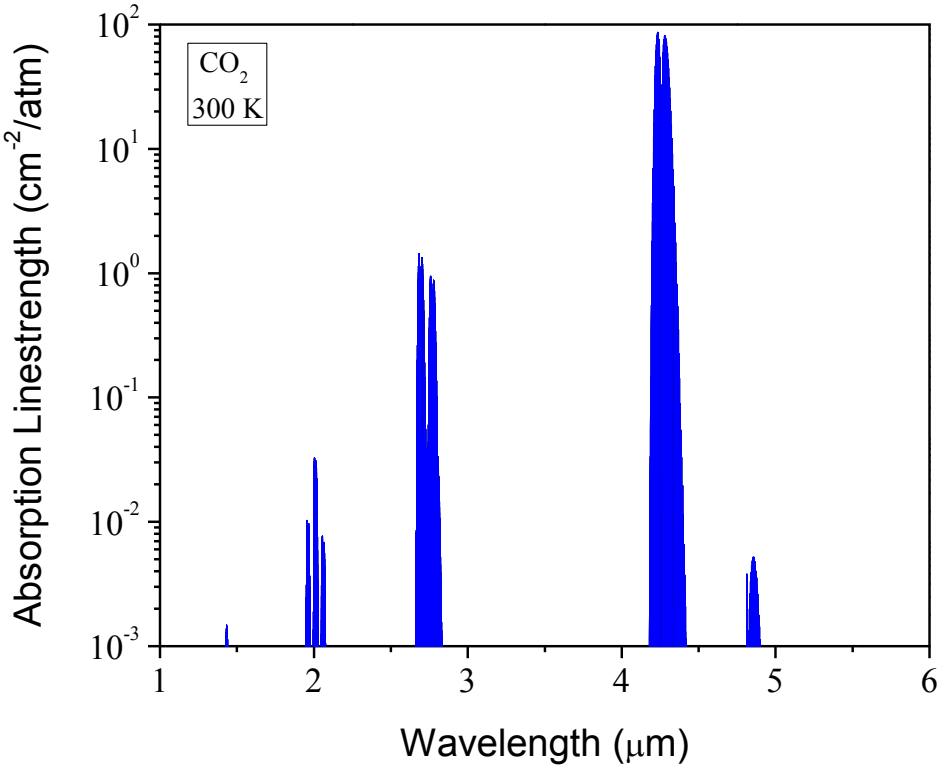

Figure 9 CO_2 absorption line-strengths at 300 K in the IR region from 1 – 6 μm. Taken from HITRAN 2004 database (Rothman, 2005).

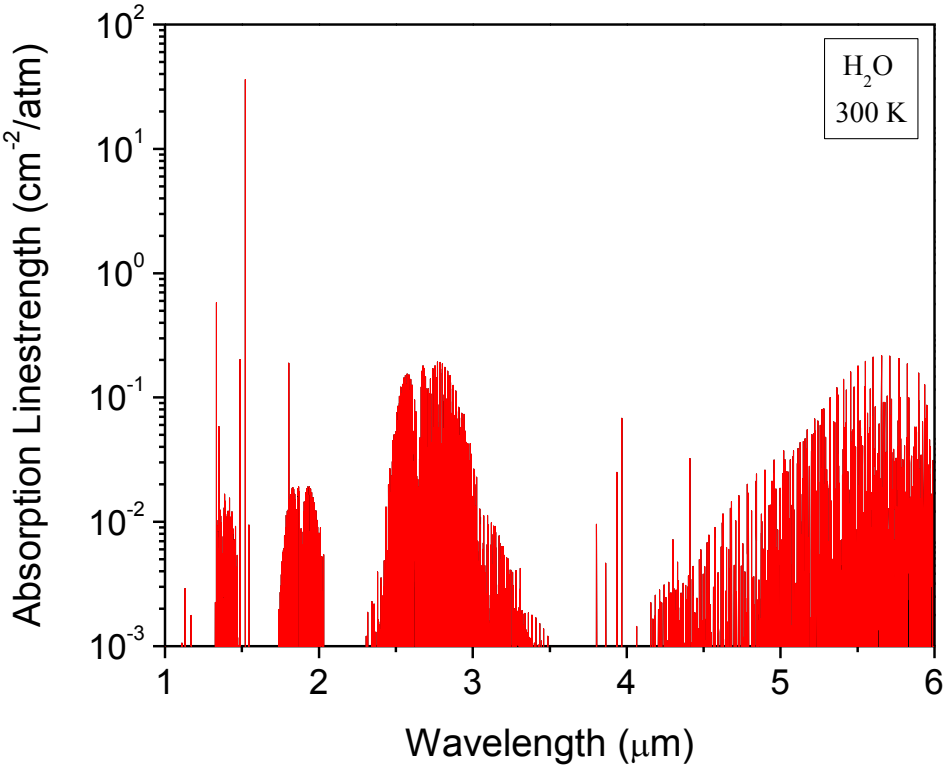

Figure 10 H_2O absorption line-strengths at 300 K in the IR region from 1 – 6 μm. Taken from HITRAN 2004 database (Rothman, 2005).

2.3.7 CH_4 absorption spectroscopy

The CH_4 molecule has a strong absorption line at 3.39 μm (2947.9 cm^{-1}). The broadening parameters of CH_4 with different collisional partners have been investigated by several groups. The effects of pressure and temperature on the methane broadening parameters have been investigated (McMahon et al., 1972; Klinbeil et al., 2006) as well as its absorption at 3.39 μm in the atmosphere (Edwards, et al., 1965). The laser emission of the helium-neon laser (HeNe) at 3.39 μm has been used extensively for the

absorption diagnostics of CH_4 and other hydrocarbons. This wavelength is of great interest for a variety of hydrocarbons for laser diagnostics since it is near the fundamental vibrational frequency of the coupling between the carbon and hydrogen atoms.

3. EXPERIMENTAL APPARATUS

The main objective of the combustor rig performance tests was to demonstrate a stable operation of the combustor with respect to combustor pressure and temperature using a mixture of natural gas, O_2 and a high concentration of CO_2. Prior to adapting the mid-IR sensor to the combustor rig, the sensor was validated using a shock-heated mixture with a known concentration of CO in a shock tube at Texas A&M University. This step was necessary to understand the QC laser wavelength sensitivity to current and temperature control. Once it was validated for CO absorption, the mid-IR sensor was coupled with the emissions probe mounted on the rig exhaust to perform the mid-IR diagnostics on the combustion gases. The mid-IR sensor was also adapted to measure fuel concentration during cold-flow tests using a continuous-wavelength (cw) He-Ne laser at 3.39μm.

This chapter discusses the experimental setup for the mid-IR diagnostics performed for this study. First, the mid-IR equipment used for the experiments is discussed and justified. Then, the mid-IR diagnostics setup is described for CO sensor validation using a shock-heated mixture. The process of capturing a sample from the combustion gases is explained as well as how the sample gas flow is directed to the emissions equipment. Aside from the mid-IR diagnostics, two additional gas analyzers were installed (by PSI workers) to measure unburned hydrocarbons, CO, and O_2 for the combustor rig performance tests. The mid-IR diagnostics adapted to measure UHC is

also discussed. Finally, the two fiber-coupled mid-IR sensor configurations are discussed.

3.1 Mid-IR equipment selection

3.1.1 Lasers as mid-IR sources for CO concentration measurements

Extensive studies of CO detection in the first and second overtone band have been carried out using different laser absorption techniques. Mihalcea et al. (1998) employed a fiber-optic diode laser system to measure combustion emission species such as CO, CO_2, and NO in the second overtone band (Δv= 3) near 1.55 μm. Chao et al. (2009) employed a tunable diode laser absorption spectroscopy (TDLS) sensor as well as a wavelength modulation spectroscopy (WMS) sensor for CO detection in the first overtone band (Δv= 2) near 2.3 μm. Lin et al. (2013) also investigated the CO detection near 2.3 μm by coupling optical emission spectroscopy (OES) and TDLS techniques. However, the absorption line-strengths of dominant combustion products H_2O and CO_2 were comparable to CO line-strengths near 1.55 and 2.3 μm which limited the CO detection limit.

The fundamental band (Δv = 1) near 4.5 μm was proven to have significantly higher CO absorption line-strengths compared to the first and second overtone bands near 2.3 and 1.55 μm, respectively. In addition to the higher line-strengths, the absorption from dominant interfering species such as H_2O and CO_2 was proven to be minimal near 4.5 μm which was shown in Chapter 2. CO detection in the fundamental band has been investigated by Jimenez et al. (2006) using a difference-frequency-mixing

based diode laser sensor. However, the low mid-IR power of the diode laser of less than 1 μW limited the sensitivity and signal-to-noise ratio for CO detection. Ren et al. (2012) employed a distributed feedback quantum cascade laser (DFB-QCL) to access the fundamental band of CO near 4.5 μm. DFB-QC lasers provide a higher power (mW) that result in higher-sensitivity measurements. A DFB-QC laser was used for the CO concentration measurements in this study.

As discussed in Chapter 2, a 3.39-μm (2947.903 cm^{-1}) HeNe laser was used for the adaptation of the mid-IR sensor to measure UHC concentrations on the combustor rig. Similar combustion applications to this study have been investigated using the 3.39 μm HeNe laser such as the development of a mid-IR sensor for pulse detonation engines (PDE) (Klingbeil et al., 2007) and the concentration measurement of heavy gas-phased hydrocarbons in a shock tube (Rotavera et al., 2010). Mevel et al. (2012) compiled 3.39 μm absorption cross section data for a variety of gas-phased hydrocarbons. The 3.39 μm HeNe laser has also been used in mid-IR absorption measurements of liquid hydrocarbon fuels by Porter et al. (2009).

3.1.2 Mid-IR detector selection

The mid-IR detectors selected for the DAS measurements presented in this thesis was based on the desired operating wavelength and bandwidth. Figure 11 shows a plot provided by Teledyne Judson Technologies showing the detectivity, D^*, of a variety of detector elements they offer with respect to the wavelength. As discussed in the previous chapters, the wavelength selected for this study was near the fundamental band of CO

($\Delta\nu$ = 1) close to 4.5 µm. The detector element was chosen to be Indium Antimonide (InSb) due to its highest detectivity at 4.5 µm.

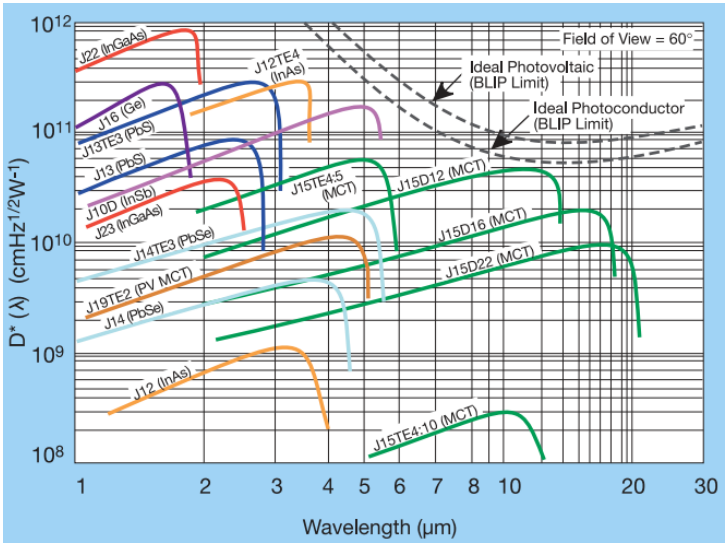

Figure 11 IR detectivity for a variety detector elements manufactured by Teledyne Judson Technologies. Taken from http://www.judsontechnologies.com/.

The detector element was chosen to be Indium Antimonide (InSb) due to its highest detectivity at 4.5 µm. Two dewar-packaged InSb detectors with an active diameter of 1 mm from Teledyne Judson Technologies were selected. A set of PA-9 preamplifiers were matched to both InSb detectors that provided a bandwidth of 1 MHz as well as a DC and AC coupled output. The high bandwidth was required to measure species concentration in time-sensitive shock-tube experiments.

3.1.3 Mid-IR optical equipment selection

All of the optics selected were optimized for the operating wavelength at 4.5 μm. Gold-coated, 1-in. diameter mirrors were used to reflect both the QC laser at 4.5 μm as well as the HeNe laser at 3.39 μm. A set of 1-in. calcium fluoride (CaF_2) lenses was used for focusing and beam-splitting purposes. A set of 1-in diameter bandpass filters was selected for both 3.39 μm and 4.5 μm. The bandpass filters were changed depending on the laser being used.

3.2 Mid-IR laser diagnostic shock-tube setup

All spectroscopic measurements were performed in a stainless steel shock tube located at Texas A&M University with an internal diameter of 15.24 cm. A schematic and picture of the shock tube and the mid-IR optical experimental setup are illustrated in Figure 12 and Figure 13, respectively. The incident shock wave propagates through the shock tube, heating the mixture temperature and pressure from (T_1, P_1) to (T_2, P_2) and eventually reflects from the end wall of the shock tube. The mixture is then raised to (T_5, P_5) after the reflected shock wave propagates through the shock tube. The pressure is measured by a pressure transducer located 16 mm from the shock-tube end wall. A more-detailed description of the shock-tube facility is given in the literature (Aul, et al., 2013).

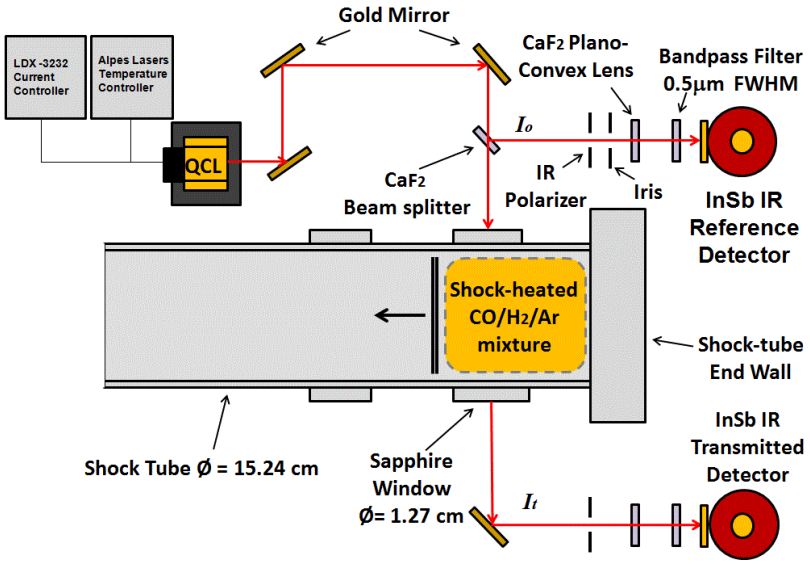

Figure 12 Schematic of the mid-IR diagnostic setup on a shock tube at Texas A&M University. The QC laser is tuned to access the R(12) transition of CO near 2190.02 cm^{-1} (4.566 μm).

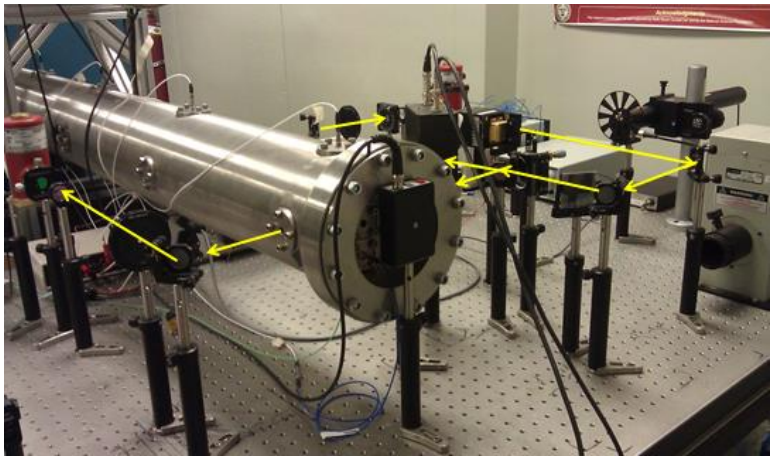

Figure 13 Mid-IR diagnostics in a shock tube at Texas A&M University. The laser path is shown to illustrate the path of the beam.

The room-temperature operated DFB-QC laser was driven by a LDX-3232 current controller and a TC-3 temperature controller from Alpes Lasers. The laser was thermoelectrically cooled and housed with collimation optics in a HHL module housing provided by Alpes Lasers. The QCL was also air-cooled for a more-stable laser performance. The current and temperature were tuned to access the $\nu''= 0$, R(12) transition of CO near 4.566 μm (2190.02 cm^{-1}). The transition line was validated by filling the shock-tube driven section with a known CO/Air mixture to confirm peak CO absorption prior to the shock-heated runs. A series of irises and bandpass filters were used to block out interference emission and any unwanted light from other wavelengths.

A mixture of 0.1% CO, 5% H_2, and 94.9% Ar (by vol.) was utilized for the results presented herein. Hydrogen was added to the mixture to minimize the vibrational relaxation time of CO behind the reflected shock wave. The spectroscopic parameters described above for air and self-broadened CO can be tabulated using the HITRAN 2004 database (Rothman, 2005). However, argon-broadening information is necessary to accurately predict the CO absorption for the shock-heated mixture. Ren et al. (2012) performed extensive studies to measure line-strength parameters as well as argon-broadening coefficients for CO transitions in the R and P-branches. They investigated their temperature dependence and extrapolated the argon-broadening parameters to fit high-temperature conditions typically experienced in shock-tube experiments.

3.3 High-pressure combustor rig testing and monitoring

The combustible mixture used for the combustor rig performance tests is comprised of natural gas, O_2, and a high concentration of CO_2. The O_2 and CO_2 mix before entering the combustor rig to form the oxidizer stream. This oxidizer mixture is then ignited with natural gas within the primary zone of the combustor by a colorless pyrophoric substance known as Triethylborane (TEB). The combustion process is propagated through the combustor and the product gases exit through the exhaust nozzle. Separate nitrogen N_2 and CO_2 cooling circuits flow within the rig to cool the combustor and exit through the exhaust nozzle along with the combustion gases. The performance tests that contained ignition were known as hot-fire tests, while tests without ignition were known as cold-flow tests. All of the gases used for the rig performances tests were stored in pressurized vessels stored close to the rig test platform.

The mid-IR diagnostics performed on the high-pressure combustor rig were coupled with the rig's data-acquisition system. This coupling allowed the mid-IR diagnostics to be synchronized with the rig's performance parameters to accurately measure the CO concentration as a function of time during a given test run. The combustor performance parameters include the equivalence ratio, fuel flow, and oxidizer flow. The combustor rig's data-acquisition system also included the pressure and temperature measurements throughout the rig as well as other testing instrumentation. Figure 14 shows a side-view of the combustor rig with attached instrumentation. The rig was pointed towards an exhaust stack where the combustion gases were directed away, as shown in Figure 15.

Figure 14 Side-view of combustor rig. A series of pressure transducers and thermocouples were attached throughout the rig to monitor rig performance and component conditions.

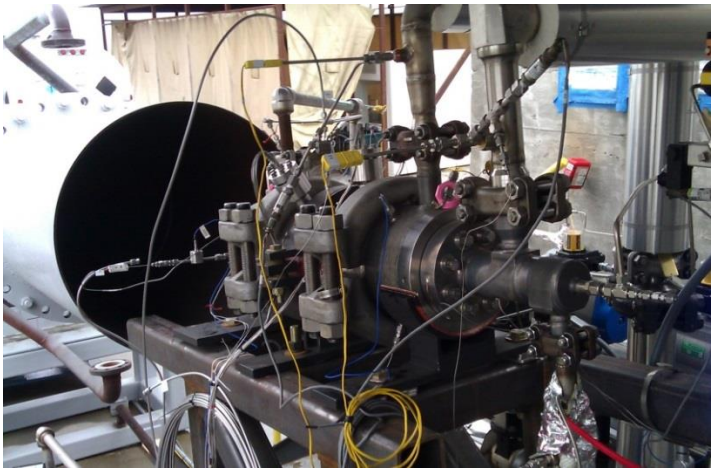

Figure 15 Combustor rig exhaust pointed towards an exhaust stack. The test platform and the surrounding area were evacuated during performance tests for safety.

A test station is shown in Figure 16, where the live feed of the measured rig parameters were monitored. This interface allowed for the mid-IR signals from the IR detectors to be monitored continuously.

Figure 16 Combustor rig test monitor. The measured rig parameters as well as the mid-IR signals were monitored continuously during performance tests at a safe distance.

3.4 Combustor rig emissions probe and sample gas line

An emissions probe was mounted on the rig exhaust to capture the combustion gases for emission analysis. Figure 17 shows a side-view of the combustor rig including the emissions probe, circled in red. The combustion gases exited the rig exhaust nozzle and entered the emissions probe orifice where it was directed to a line that led to the

emissions equipment. Figure 18 illustrates a simplified schematic of the probe housing, while Figure 19 shows a picture of the housing mounted on the exhaust.

Figure 17 Combustor rig side-view showing the probe housing. The housing contained the emissions probe that transferred the sample captured from the combustion gases into the emissions equipment.

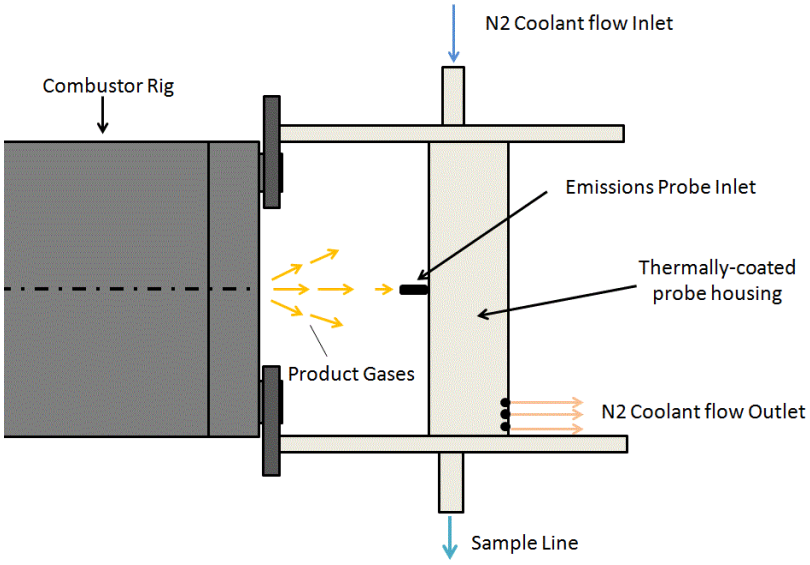

Figure 18 Schematic of the combustion gases exiting the rig exhaust nozzle and into the emissions probe. N_2 gas flowed within the housing to protect the emissions probe from high temperatures.

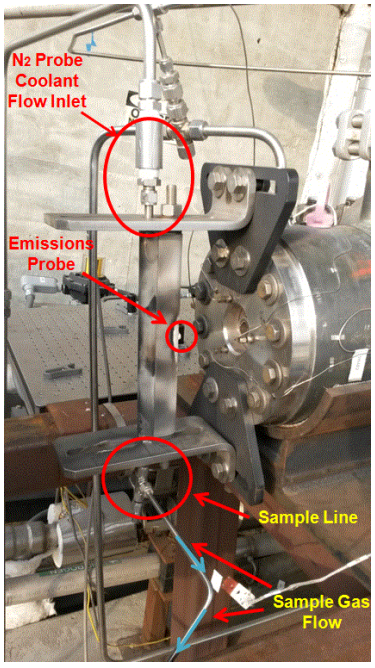

Figure 19 Emissions probe and sample gas transfer mounted on the rig exhaust. The N_2 coolant gas flow entered the housing and exited in the direction of the combustion gases.

A thermal coating was applied on the exterior of the probe housing to protect the emissions probe from the flame. N_2 gas flowed through the probe housing for cooling purposes and exited in the direction of the combustion gases while the emissions probe was sealed to prevent any N_2 flow through the sample line. The sample line directed the sample gas into the three different emission systems shown in Figure 20. The far left block in Figure 20 is an unburned hydrocarbon (UHC) analyzer manufactured by VIG Industries, Inc., which operated as a flame ionization detector (FID) using a H_2-O_2 flame. The middle block in Figure 20 represents an O_2 and CO analyzer with a sample conditioning system for H_2O removal. The O_2/CO analyzer was manufactured by California Analytical Instruments (CAI) Inc. The block on the far right represents the mid-IR diagnostics. The pressure and temperature of the sample gas were monitored prior to entering the gas analyzers with a 0-50 psig pressure transducer and K-type thermocouple.

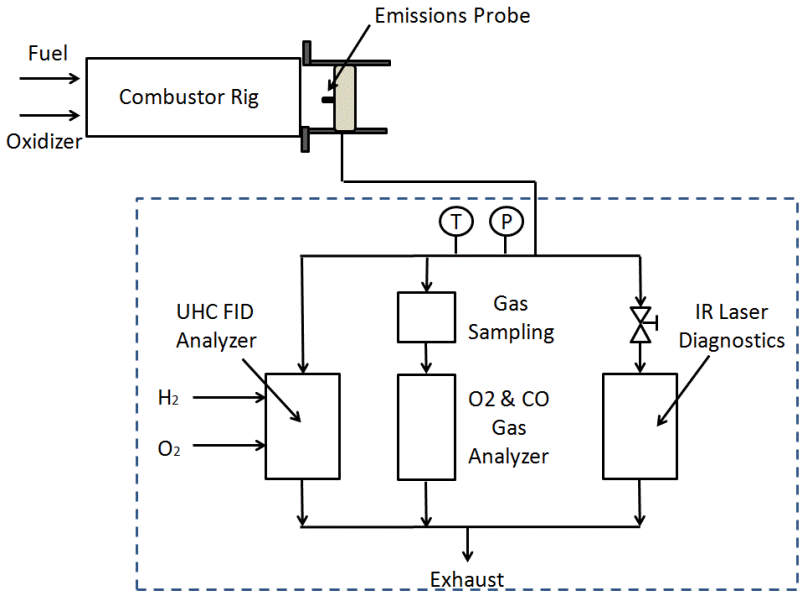

Figure 20 Distribution of sample gas captured from the rig exhaust into the three emission systems: UHC analyzer (left), O_2/CO analyzer (center) and mid-IR sensor (right).

The emissions equipment was located in a shed close to the rig test platform. Figure 21 shows the sample gas flow from the rig exhaust directed towards the emissions shed. This shed protects the equipment from rain and the harsh environment during performance tests. Flow is split in three ways that feed into each emissions system shown in Figure 21. All three emission systems dump the sample gas to the atmosphere after analysis.

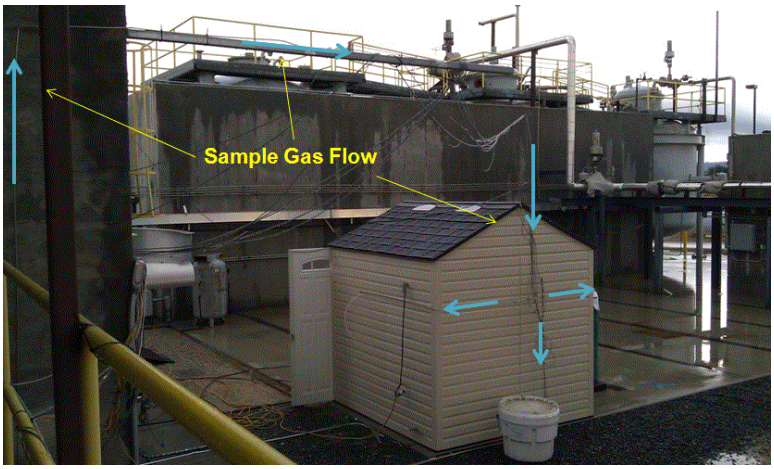

Figure 21 The sample gas captured from the rig exhaust was directed towards the emissions shed where the UHC analyzer, O_2/CO analyzer, and the mid-IR sensor were located.

3.5 Mid-IR laser diagnostic setup for CO concentration measurements

3.5.1 Mid-IR laser diagnostics during rig performance tests

The mid-IR sensor adapted to measure CO concentrations during rig performance tests is illustrated in Figure 22. The absorption cell used for the DAS measurements contained an optical path length of about 11.8 cm. This optical path length was chosen for optimal CO absorption with good signal-to-noise ratio (SNR). More information on the absorption cell optimization and constraints are found in A.2 of the appendix. The absorption cell contained two optical windows made of sapphire. These optical windows were intentionally made for the fiber-coupled, mid-IR sensor configuration which is discussed later in this chapter.

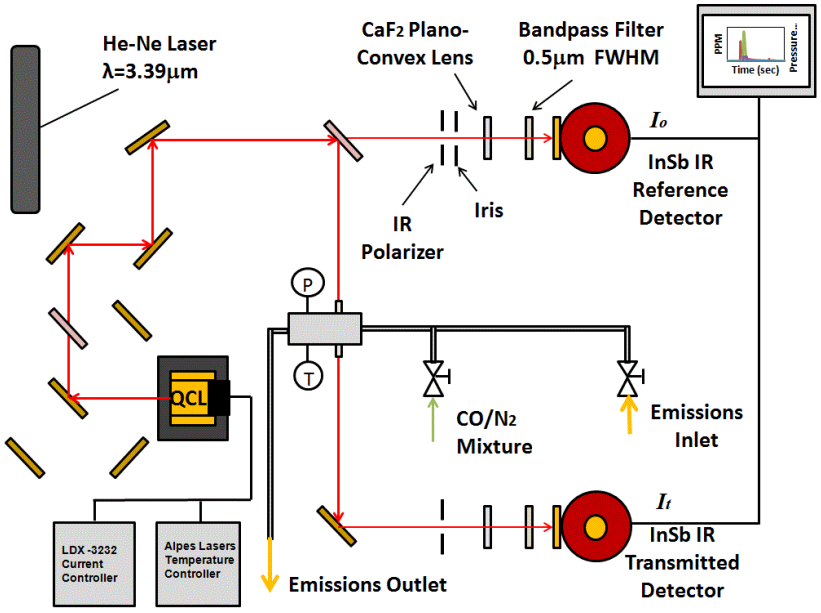

Figure 22 Mid-IR diagnostics setup for CO concentration measurements. The reference and transmitted IR detectors were coupled into the combustor rig DAQ system. The QCL was tuned to operate near the R(12) transition at 2190.02 cm^{-1} (4.566 μm).

The sample gas from the rig entered the absorption cell and exited to the atmosphere. The pressure and temperature were monitored by a 0-50 psig pressure transducer and K-type thermocouple within the absorption cell as shown in Figure 22. Figure 23 shows a top-view of the mid-IR laser diagnostic setup. Similar to the mid-IR optical setup on the shock tube, the two InSb IR detectors were used to capture the incident and transmitted signals. The InSb IR detectors were connected to the PA-9 preamplifiers manufactured by Teledyne Judson Technologies and coupled into the rig data-acquisition system for synchronous and live data-capturing.

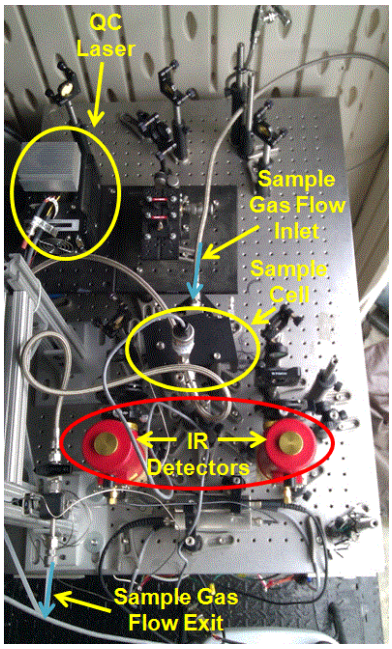

Figure 23 Top-view of the mid-IR diagnostic setup. The sample gas flow (top) enters the absorption cell and exits to the atmosphere (bottom) during rig performance tests.

Figure 24 shows the pitch-side of the mid-IR diagnostics where the QC laser beam was reflected from a set of gold mirrors to direct the beam towards the receiving-side. Figure 25 shows the receiving-side of the diagnostics where the IR laser beam was split into two beams by a 50/50 beamsplitter. One beam was transmitted through the beamsplitter into the IR reference detector that recorded I_o. The other beam was reflected off of the beamsplitter towards the absorption cell. The beam propagated through the absorption cell where it was attenuated by the CO within the sample gas flow. The attenuated IR laser beam was then reflected off of a gold mirror towards the IR (transmitted) detector that recorded I_t. Both beams were focused by a CaF_2 plano-convex lens into the 1-mm active diameter InSb elements sealed by cryogenic dewars that make

up the red detector housing. Narrow-bandpass filters centered at about 4.5µm with a FWHM of 0.5µm were placed right before both IR detectors to block any unwanted light from going into the detectors. An iris was placed before the detectors for additional protection from unwanted light. An IR polarizer was also placed before the incident optics to adjust the laser intensity going into the incident IR detector. The raw voltage signals from both IR detectors were measured through the rig DAQ system for performance tests. Figure 26 shows a close-up on the absorption cell with the IR laser beam propagating as the sample gas flowed. Figure 26 shows a close-up on the absorption cell with the IR laser beam propagating as the sample gas flowed. Figure 27 shows the sample gas inlet for the mid-IR sensor. A needle valve controlled the sample gas flow into the absorption cell.

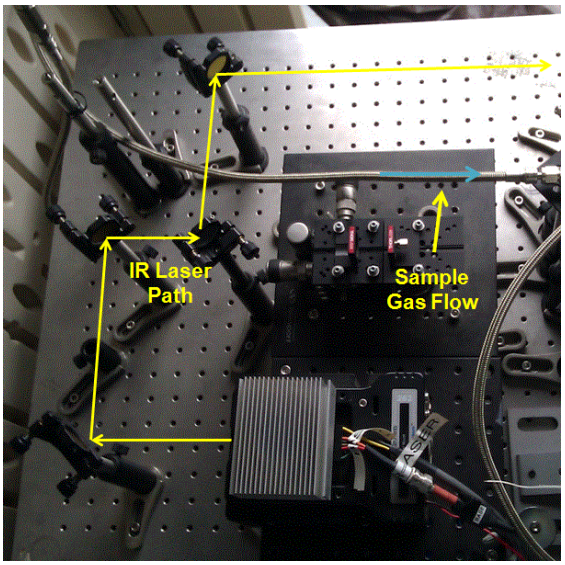

Figure 24 Pitch-side of mid-IR sensor where the QC laser outputs a collimated IR beam. The beam is reflected through a series of mirrors for DAS measurements.

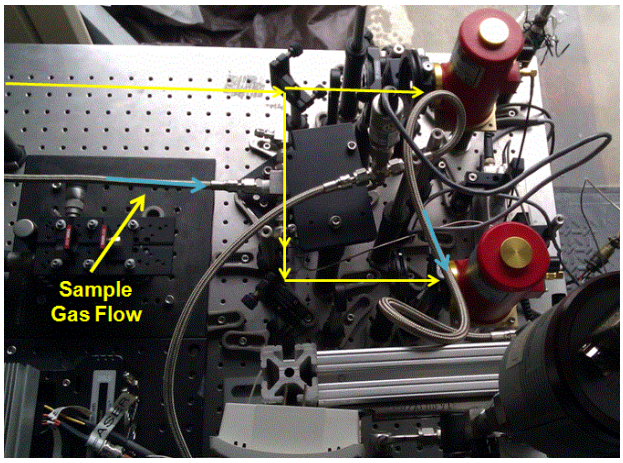

Figure 25 Catch-side of the mid-IR sensor where the IR laser beam is split into the IR reference and transmitted detector.

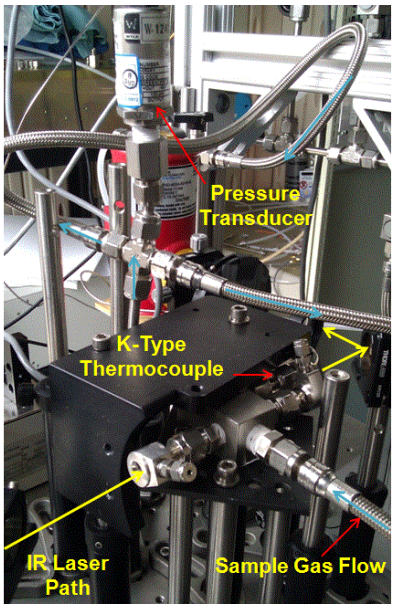

Figure 26 IR laser beam propagation through the absorption cell as the sample gas flowed through the cell.

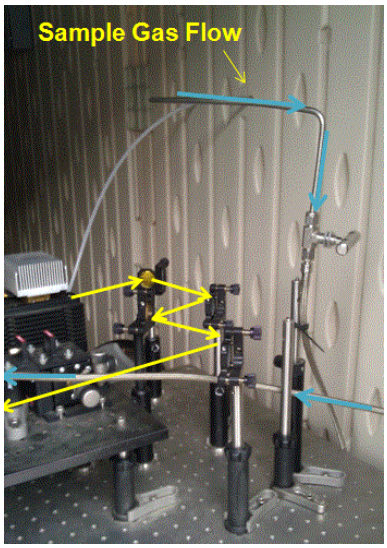

Figure 27 Sample gas flow inlet to the mid-IR sensor. A valve was placed to seal off the mid-IR sensor when it was not in use.

Figure 28 illustrates a schematic of the absorption cell during a CO mid-IR absorption diagnostic test on the combustor rig. The Swagelok quarter-turn valve that leads to the calibration manifold is closed during the absorption diagnostics.

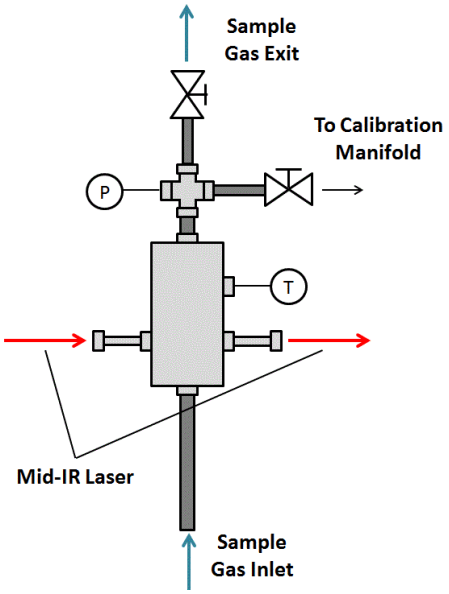

Figure 28 Absorption cell schematic during a CO mid-IR absorption diagnostic test on the combustor rig. The sample gas flows as the mid-IR laser passes through the cell.

3.5.2 Mid-IR QC laser calibration for CO concentration measurements

The operating wavelength needed to be known prior to each test to make accurate CO concentration measurements. Although the QC laser was validated using a shock-heated mixture at Texas A&M University, the QC laser may exhibit small mode-jumps which was discussed in Ch. 2 (coupled with the fact the system was operating in a challenging environment when compared to what exits in a laboratory). Therefore, the mid-IR sensor needed to be wavelength-calibrated prior to any DAS measurements.

The mid-IR sensor was calibrated for operation near the R(12) transition (2190.02 cm^{-1}) using a mixture of 0.1% CO/N_2 (vol.) provided by Airgas. The layout of the CO/N_2 mixture with respect to the mid-IR diagnostics is shown in Figure 22. Figure 29 and Figure 30 show how the CO/N_2 mixture was transferred to the absorption cell.

Figure 31 and Figure 32 illustrate a schematic of the absorption cell and the calibration gas manifold, respectively. The needle valve controlling the sample gas flow was closed, and the absorption cell was evacuated to less than 500 mTorr using a vacuum pump. The leak rate of the absorption line was measured to be less than 100 mTorr/min. The absorption cell was filled with the known CO/N_2 mixture, and the laser attenuation was measured for sensor calibration. The temperature was recorded by the K-type thermocouple within the absorption cell, while the sub-atmospheric pressure during calibration was measured by a MKS sub-atmospheric gauge that possessed a 0.5% relative uncertainty.

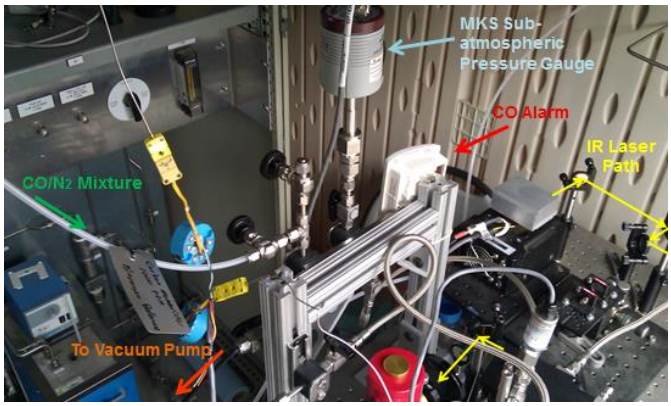

Figure 29 The absorption cell was initially evacuated, sealed and filled with a mixture of 0.1% CO/N_2 (vol.) for sensor calibration.

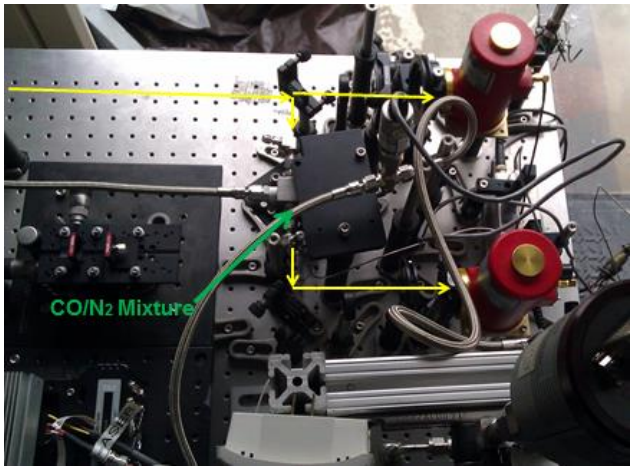

Figure 30 CO/N_2 calibration mixture was transferred into the absorption cell at selected pressures, and the laser attenuation was measured to determine the true operating wavelength.

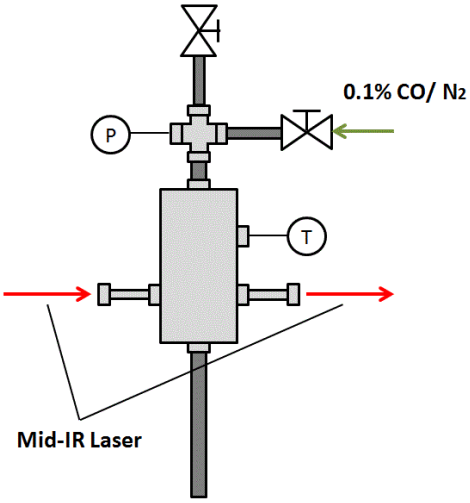

Figure 31 Absorption cell schematic during the QC laser calibration. The absorption cell is sealed from the sample gas during the calibration procedure.

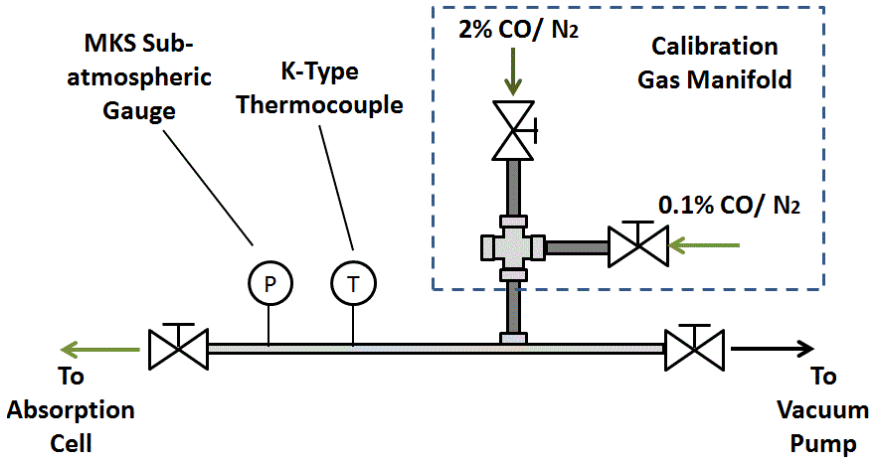

Figure 32 Calibration gas manifold that feeds the CO/N_2 calibration gas into the absorption cell. The pressure and temperature of the calibration gas are monitored as the absorption cell is filled.

3.6 Mid-IR laser diagnostics for UHC concentration measurements

The mid-IR sensor was adapted to measure unburned hydrocarbons (UHC) from the combustor rig. To test the validity of this configuration, the sensor was used during rig performance test without ignition (cold-flow tests) to measure the hydrocarbon fuel concentration. The mid-IR sensor was calibrated for CH_4 using the 3.39 μm HeNe laser since the natural gas composition used for the performance test was mainly comprised of CH_4.

The mid-IR diagnostics for fuel concentration measurements consisted of the same optical setup discussed in 3.5.1. However, a set of gold mirrors were placed to co-align the HeNe laser with the original beam path of the QC laser. This was done for the flexibility of adapting the mid-IR sensor to measure CO or hydrocarbon concentrations without any additional optical alignment. The bandpass filters used for the CO

measurements were replaced with a set of filters with center wavelength (CWL) of 3.39 µm and a 0.195-µm FWHM. The schematic of the mid-IR diagnostics adapted to measure unburned hydrocarbons is shown in Figure 33.

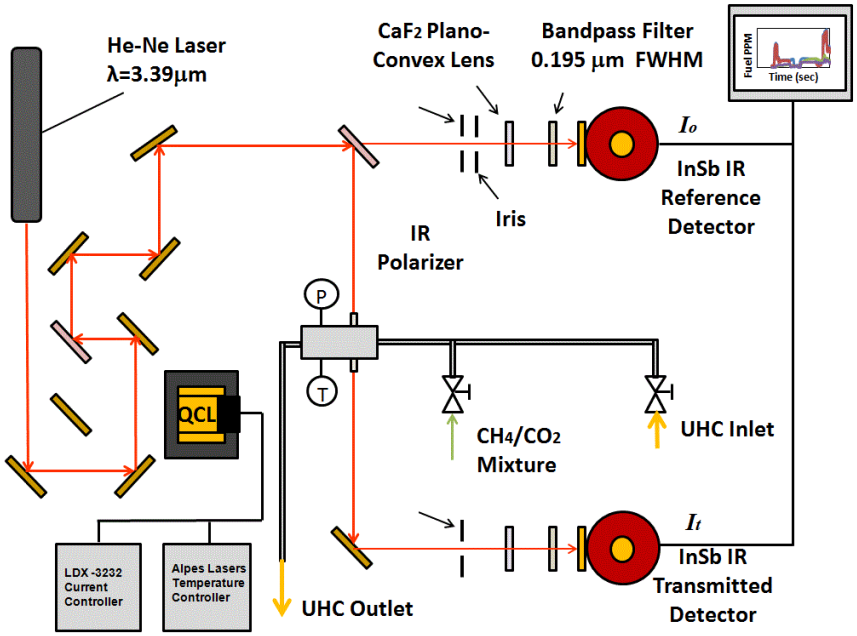

Figure 33 Mid-IR sensor adapted to measure unburned hydrocarbons using a HeNe laser at 3.39 µm.

Wavelength calibration of the mid-IR sensor was not needed with the HeNe laser since it only operates at 3.39 µm. However, an additional set of experiments was required to determine the CO_2 broadening behavior with CH_4. A mixture of 3% CH_4/CO_2 was used to experimentally determine absorption cross-section between the two constituents. A relation between the absorption cross-section and the total mixture pressure was experimentally determined for CH_4 broadened with CO_2. The detailed

analysis for this calibration procedure can be found in A.3 of the Appendix. CO_2 was used instead of O_2 or N_2 because the fuel was heavily diluted in CO_2 during cold-flow tests. The O_2 percentage within the oxidizer was kept low during cold-flow tests to avoid possible auto-ignitions at high-pressure cold-flows. Therefore, the mid-IR sensor and the UHC analyzer were calibrated using the calibration gas comprised of 3% CH_4/CO_2.

3.7 Fiber-coupled mid-IR sensor for CO concentration measurements

In addition to the DAS measurements performed using the absorption cell, the design and development of a fiber-coupled mid-IR sensor configuration has been proposed to directly align the mid-IR laser through the combustor rig. Although the fiber-coupled configurations were not used for any of the rig performance tests discussed in this study, they were implemented onto the rig to validate its use for future performance tests. The advantage of implementing such a configuration is to measure the CO concentration directly from the combustor in order to understand the true CO behavior during the combustion process. This in situ measurement would provide a direct comparison between the DAS measurements using the absorption cell and the combustor. This section discusses the design and development of two possible configurations.

Two fiber-coupled configurations have been proposed. The configurations differ in the way the mid-IR optical fiber is coupled onto the combustor rig. Both fiber-coupled configurations have three designated sections. Section A is known as the fiber-coupling section where the mid-IR beam from the QC laser is coupled into the optical fiber.

Section B is designated as the pitch side where the fiber and collimating lens are attached to the rig while outputting a collimated mid-IR beam. Section C is designated as the catch side where the mid-IR beam passes the absorbance path length and into the IR transmitted detector. Figure 34 illustrates a schematic of Section A.

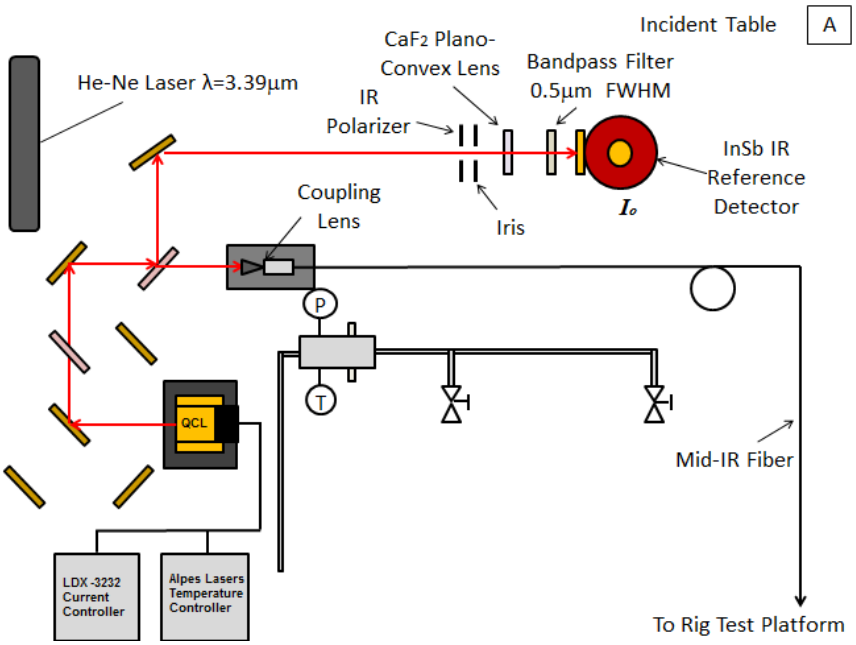

Figure 34 Schematic of Section A of the fiber-coupled mid-IR sensor. The mid-IR beam is focused into the optical fiber where it is extended up to the combustor rig.

The optical setup discussed in section 3.5.1 is used for Section A of the fiber-coupled mid-IR sensor. The mid-IR beam is split into two beams using the 50/50 beamsplitter further upstream than discussed in section 3.5.1. The first split beam is transmitted through the beamsplitter and into a mid-IR objective lens where the beam is focused down to a spot diameter of approximately 32 µm. The optical fiber is a 7-m

Chalcogendie (CIR) As-s glass fiber with a core diameter of 180 μm. The mid-IR objective lens is supplied by Innovation Photonics with a focal length of 6 mm. A Microblock 3-Axis positioner with a differential micrometer from Thorlabs is used for the coupling of the mid-IR laser into the optical fiber.

3.7.1 Configuration 1 for fiber-coupled mid-IR sensor

Figure 35 illustrates the configuration 1 layout for the fiber-coupled mid-IR sensor. Section A is located behind a concrete wall and in a safe distance from the combustor rig test platform. The 7-m optical fiber is attached onto the rig shown as Section B.1. The mid-IR exits the fiber/collimator assembly, passes through the combustor, and enters a 5-in. diameter integrating sphere with a 1-in. diameter entrance slit. The gold-coated integrating sphere, manufactured by Labsphere, allows for small beam misalignment cause by rig vibrations. This effect is due to the highly reflective, diffuse surface of the sphere that allows the IR beam entering the sphere to be incident on the IR detector. A bandpass filter entered at 4.5 μm with a 0.5 μm FWHM at the entrance of the integrating sphere.

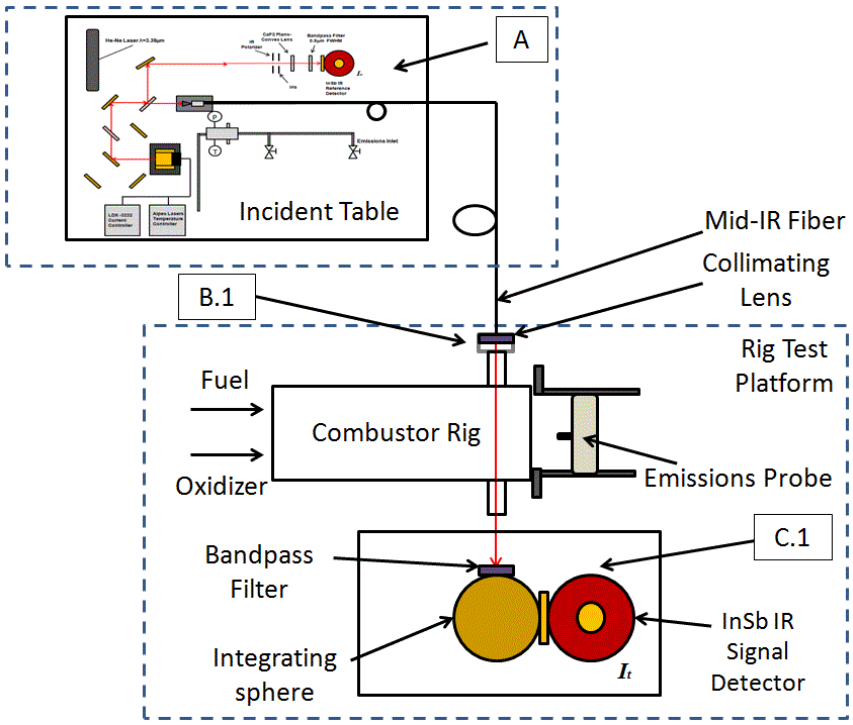

Figure 35 Configuration 1 layout for fiber-coupled mid-IR sensor. The optical fiber is attached to the optical window port that provides optical access through the rig.

Figure 36 shows a three-dimensional CAD model of the rig exhaust provided by PSI along with the mid-IR laser beam path. The optical window port shown in Figure 36 contains an orifice above the sapphire window to allow N_2 to purge externally for cooling purposes. This window port was developed by EnvirOptics, Inc.

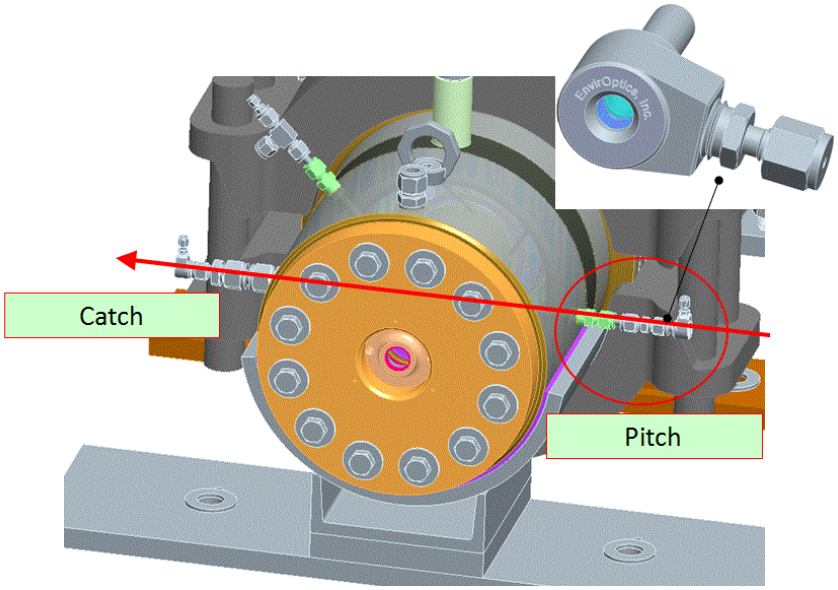

Figure 36 CAD model of combustor rig showing mid-IR laser beam propagation. The optical window port developed by EnvirOptics, Inc. is mounted on both ends of the optical pathway. This image is courtesy of PSI.

Figure 37 illustrates a simplified cross-section of the combustor rig exhaust showing the optical pathway through the combustor exhaust liner. The absorbance path length may be taken as the exhaust liner inner diameter with caution. The total distance of the Swagelok fittings connecting the optical window ports may need to be considered part of the path length since the combustion gases can expand within their small volumes.

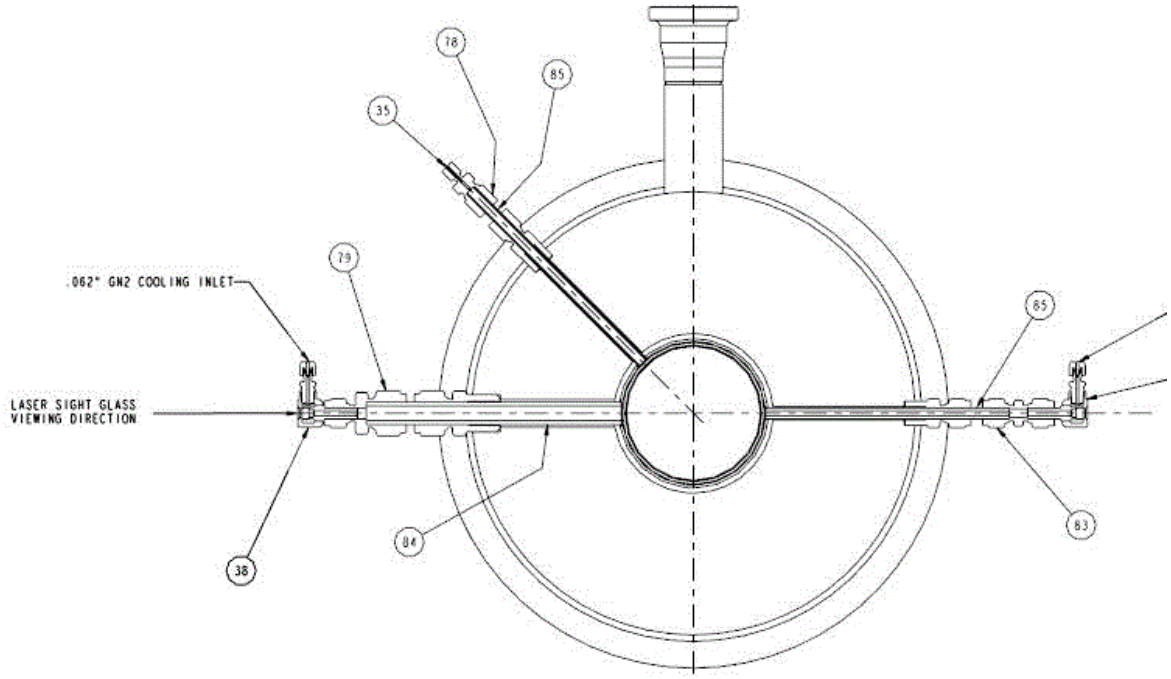

Figure 37 Simplified cross-section of the combustor rig showing the optical pathway through the combustor exhaust liner. Drawing is courtesy of PSI.

Figure 38 shows the proposed fiber/collimator attachment method circled in red. The attachment is represented by Section B.1 in Figure 35. Figure 39 shows the position of the integrating sphere with respect to the optical window port represented as Section C.1 in Figure 35.

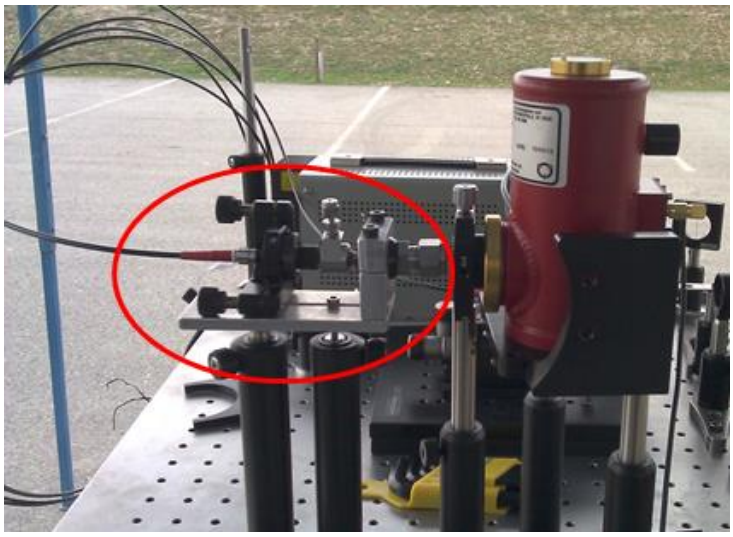

Figure 38 Attachment method between fiber/collimator assembly and combustor rig. The IR detector arrangement shown is for maximizing the mid-IR signal through the optical fiber.

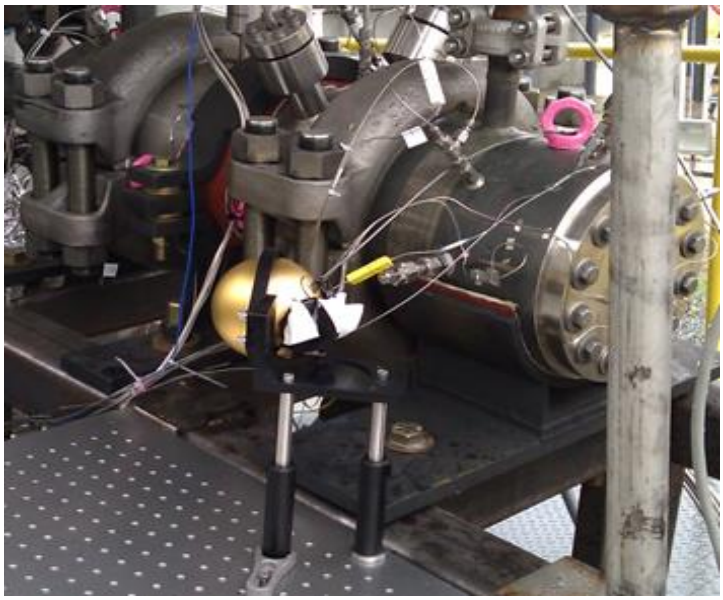

Figure 39 Location of the integrating sphere with respect to the combustor rig optical window port represented as Section C.1. The IR transmitted detector is not shown.

3.7.2 Configuration 2 for fiber-coupled mid-IR sensor

Figure 40 illustrates a schematic of configuration 2. The optical fiber is attached near the exit of the exhaust (B.2), and the mid-IR laser propagates through the exit gas flow and into the integrating sphere (C.2). The mid-IR laser is aligned as close to the exhaust as possible to avoid any changes in static conditions due to over-expansion. Figure 41 shows the optical breadboards used to for B.2 and C.2. The black breadboard table on the right side of Figure 41 (pitch side) is bolted onto a concrete block on the ground to isolate the optical fiber and collimator from the rig vibrations as much as possible. Figure 42 shows the optical fiber and collimator mounted on the pitch side along with the integrating sphere and IR transmitted detector mounted on the catch side. The equipment is lowered below the exhaust center to show the alignment between optics. A total of 35 in was measured between the collimator and the integrating sphere.

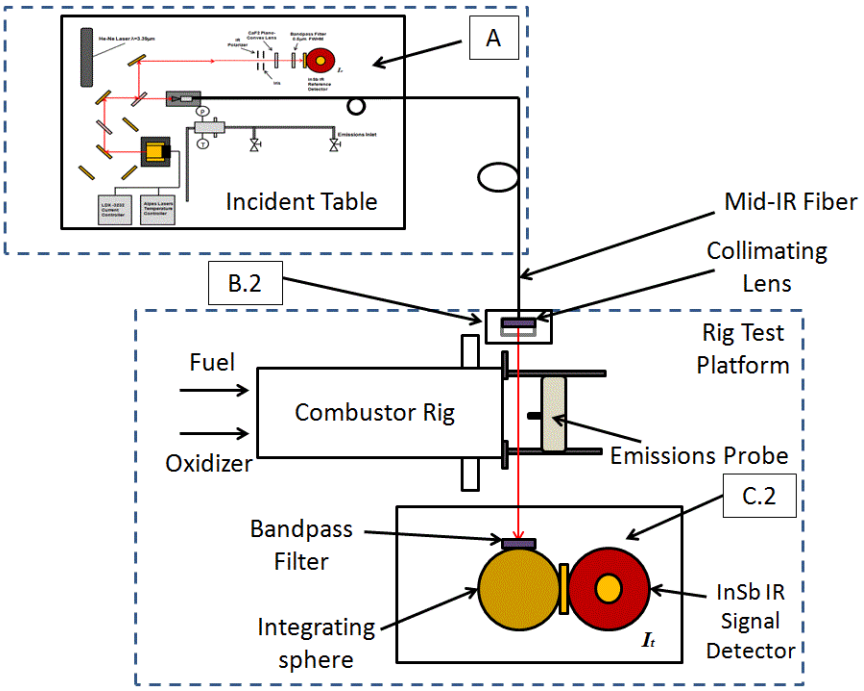

Figure 40 Schematic of configuration 2 for the fiber-coupled mid-IR sensor. The fiber is bolted close to the exhaust and shoots the mid-IR laser beam through the flame zone.

Figure 41 Mounted optical breadboards near exhaust for configuration 2 represented as B.2 and C.2.

Figure 42 Optical fiber and integrating sphere aligned below the rig exhaust center to show beam path.

4. EXPERIMENTAL PROCEDURE

In addition to the previously discussed mid-IR sensor configurations, the experimental procedure needs to be clarified for accurate IR signal monitoring. As discussed in A.3 of the Appendix, The IR voltages from the InSb IR detectors each contain an offset due to the IR emissions generated from the surroundings. The IR signal outputs from the detectors without operating any lasers, or zero IR signals, increase with increasing ambient temperature. These zero signals need to be frequently monitored to account for the zero-offset variation. In addition to monitoring the zero IR signals, the baseline signals, or IR signals with the laser beam incident on the detectors, also need to be monitored. A signal offset may be generated from one of the IR detectors by a drift in laser power. Nevertheless, both zero and baseline IR signals needed to be frequently monitored for accurate concentration measurements.

The zero and baseline IR signals were recorded from a portable digital oscilloscope prior to every combustor rig performance test. The difference in IR signals from both detectors is "zeroed" to correct for species absorption during the performance tests. After the combustor rig test platform has been evacuated for the commencement of high-pressure flows, the IR signals are monitored through a .vi created using LabVIEW that provided a live feed from all of the measured rig parameters. Measuring the IR signals from the detectors through the .vi allows the viewer to check for any odd laser behavior with respect to the mass flows, rig temperature and pressure. Any IR baseline offsets or signal fluctuations shown from the .vi were recorded. This procedure was

repeated after all rig performance tests. The zero and baseline IR signals were recorded using the portable digital oscilloscope once the rig test platform was cleared for personnel. The CO/N_2 calibration process was repeated to check for any laser mode-jumps.

These IR measurement procedures were replicated for fuel concentrations using the 3.39 μm HeNe laser. Although checking for any laser mode-jumps is not necessary for the HeNe laser since it operates at a continuous wavelength of 3.39 μm, the IR zero and baseline measurement procedure was still used. The HeNe laser called for more-frequent IR baseline signal monitoring due its noticeable nature in laser power drifts in the HeNe laser. The zero and baseline IR signals were also used for statistical uncertainty to calculate the total uncertainty in species concentration shown in A.3 in the Appendix.

5. RESULTS AND DISCUSSION

The results shown in this chapter were taken from the combustor rig tests performed at the Wyle facility in San Bernardino, CA. The transient behavior such as ignition and flame-out were successfully captured for the ignited performance tests, or hot-fire tests. Section 5.1 discusses the mid-IR sensor validation using a shock tube located at Texas A&M University. This validation using a shock-heated mixture was an important step before applying it to the combustor rig performance tests to understand the behavior of the QC laser and its tunable range with respect to temperature and current. A 0.1% CO / 5% H_2 / 94.9% Ar mixture was used and shock-heated to measure the CO absorbance behind the incident and reflected shock waves. Section 5.2 presents the results obtained from the combustor rig performance tests for CO concentration measurements. The mid-IR sensor was calibrated on-site by using a CO/N_2 mixture discussed in the previous chapters. The results presented in section 5.2 compare the mid-IR diagnostics to the measured combustor rig parameters to understand the CO time-history during combustion. An equilibrium analysis was performed to analyze the mid-IR CO concentration measurements during stable rig conditions. The CO concentration was measured as 67 ppm ±12 ppm at a stable rig pressure and temperature during a successful stable rig operation close to 103 bar. Section 5.3 presents the results using the mid-IR diagnostics adapted to measure fuel concentration to validate its usability for potential UHC measurements during hot-fires. These measurements are performed using a HeNe laser operating at 3.39 μm. The absorption coefficient for these measurements

was experimentally determined prior to any performance test without ignition (cold-flow tests) to understand the broadening effect for CH_4-CO_2. Finally, section 5.4 discusses the preliminary results for the fiber-coupled mid-IR diagnostics and its design challenges. Although they have not been tested during rig performance tests, the fiber-coupled configurations provide a direct optical access through the exhaust liner of the combustor rig.

5.1 Mid-IR sensor validation using a shock-heated mixture

Figure 43 illustrates the CO absorbance and pressure traces as the shock wave propagated through the shock tube. The absorbance was calculated using Eq. 50 along with the voltage signals captured by the InSb IR detectors. Prior to the shock, the driven section of the shock tube was filled to a total mixture pressure of 300 torr at 294 K (state 1) using 0.1% CO, 5% H_2, and 94.9% Ar. The incident shock wave flowed through the mixture and raised the pressure and temperature to 2.85 atm and 786 K (state 2). After the shock wave hit the end wall, the reflected shock raised the pressure and temperature even further to 10.8 atm and 1419 K (state 5).

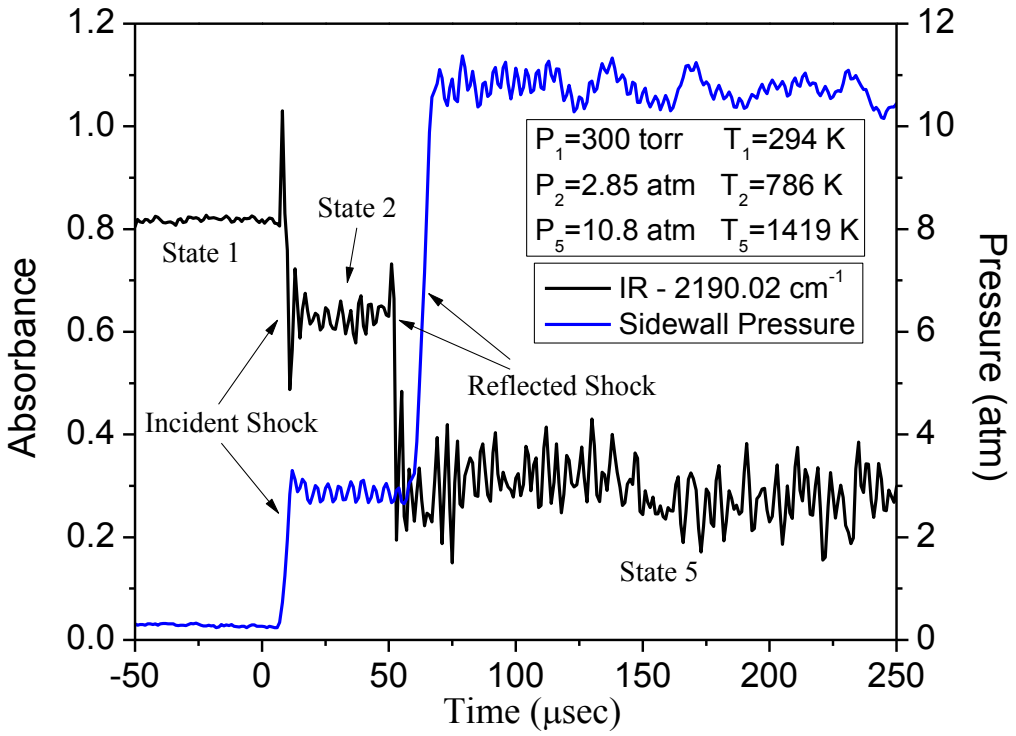

Figure 43 Fixed-wavelength CO absorbance time-history in the shock tube with 0.1% CO / 5% H_2 / 94.9% Ar.

The conditions at each state were calculated using standard normal-shock relations along with the measured incident shock speed. Figure 44 illustrates the simulated absorbance spectra of the CO R(12) transition. The absorbance was calculated using the CO line-strength taken from the HITRAN 2004 database (Rothman, 2006) along with the Ar-broadening parameters measured by Ren et al. (2012). Table A. 1 of the Appendix summarizes the CO line-strength and Ar-broadening parameters measured by Ren et al. (2012) along with their uncertainty for the R(12) transition. The H_2-

broadening was neglected since the Ar-collision-broadened width is dominant due to its significant dilution.

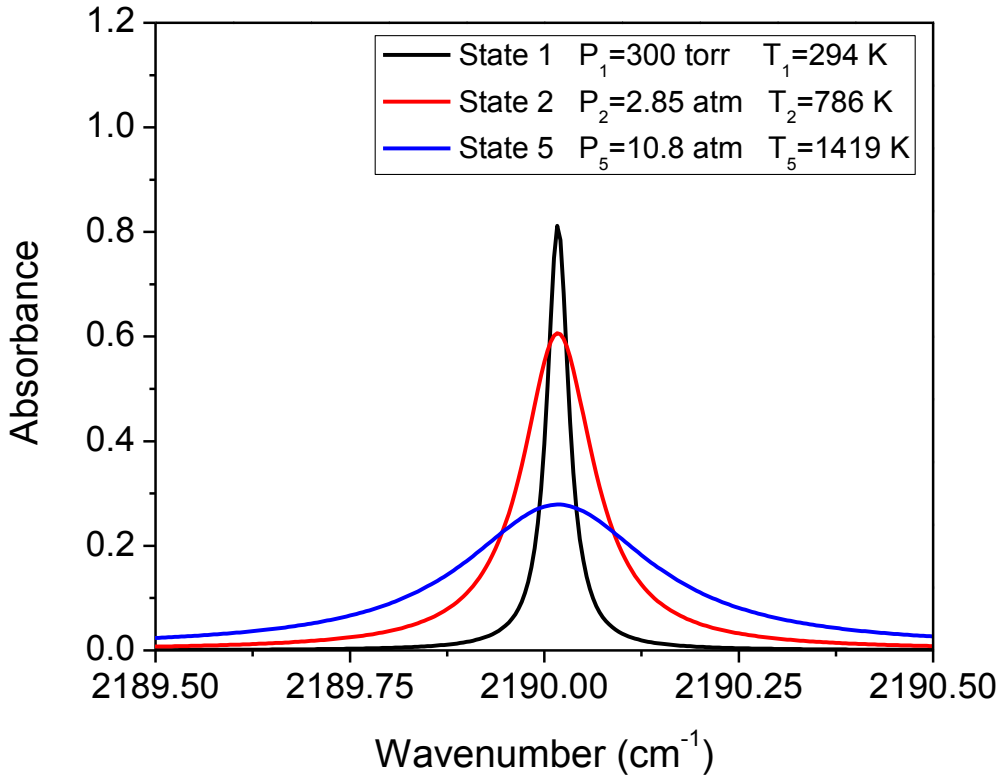

Figure 44 Simulated absorbance for 0.1% CO / 5% H_2 / 94.9% Ar. The simulated absorbance corresponds to shock-heated conditions.

The absorbance measured during the shock-heated runs shows good agreement with the simulated absorbance. The state 2 simulated absorbance shows a slight under-prediction compared to its measured absorbance due to its greater uncertainty in the Ar-broadening parameters. Ren et al. measured the Ar-broadening coefficient, $2\Upsilon_{CO\text{-}Ar}$, and

extrapolated it to fit the temperature range of 1100-2000 K along with the temperature index, *n*.

However, the missing Ar-broadening information at T_2 from the shock-heated runs leads to larger uncertainties in the simulated spectra. The reported values in Table A. 1 for $2\gamma_{CO\text{-}Ar}$ (296K) measured at room temperature and fitted to 1100-2000 K are 0.088 [cm^{-1} atm^{-1}] with an uncertainty of 3.0% and 0.079 ±0.007 [$cm^{-1}atm^{-1}$], respectively. The reported value and uncertainty for the temperature index, *n*, fitted to 1100-2000 K is 0.581 ±0.012 (Ren et al., 2012).

5.2 CO concentration measurements using IR diagnostics at 4.5μm

5.2.1 On-site sensor calibration for CO concentration measurements

The mid-IR sensor was calibrated prior to the rig performance tests for proper CO concentration measurements. As discussed in Chapters 3 and 4, the mid-IR sensor was first validated on-site at room temperature by filling the absorption cell with 0.1 % CO/N_2 (vol.) and measuring the CO absorbance prior to each rig performance (hot-fire) test. The absorbance was compared to the calculated absorbance using the DAS simulation to verify the operating wavelength. Table A. 2 of the Appendix tabulates the $CO\text{-}N_2$ broadening at 300 K that was used to calculate the broadening coefficient at the corresponding temperature during calibration. Figure 45 illustrates the measured absorbance using the CO/N_2 calibration gas compared to the calculated absorbance. The absorption coefficient is plotted in Figure 46 using the results shown in Figure 45. The difference shown between the measured and calculated absorbance is due to laser mode-

jumps that cause a shift in operating wavelength. This wavelength shift causes the absorption coefficient to drift away from its peak value at 2190.02 cm^{-1} depending on how far the laser mode-jumps spectrally. Section A.1 of the Appendix discusses the QC laser mode-jumps and proposes an ideal laser condition for a more stable operation.

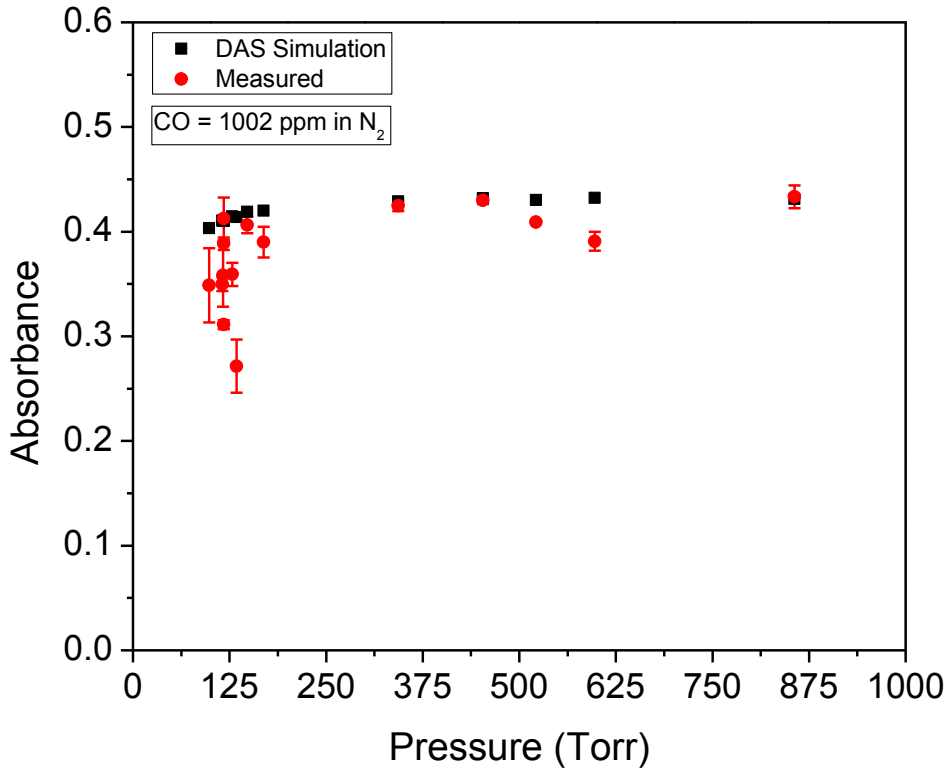

Figure 45 CO absorbance comparison between measured and calculated values using 0.1 % CO/N_2 (vol.) mixture.

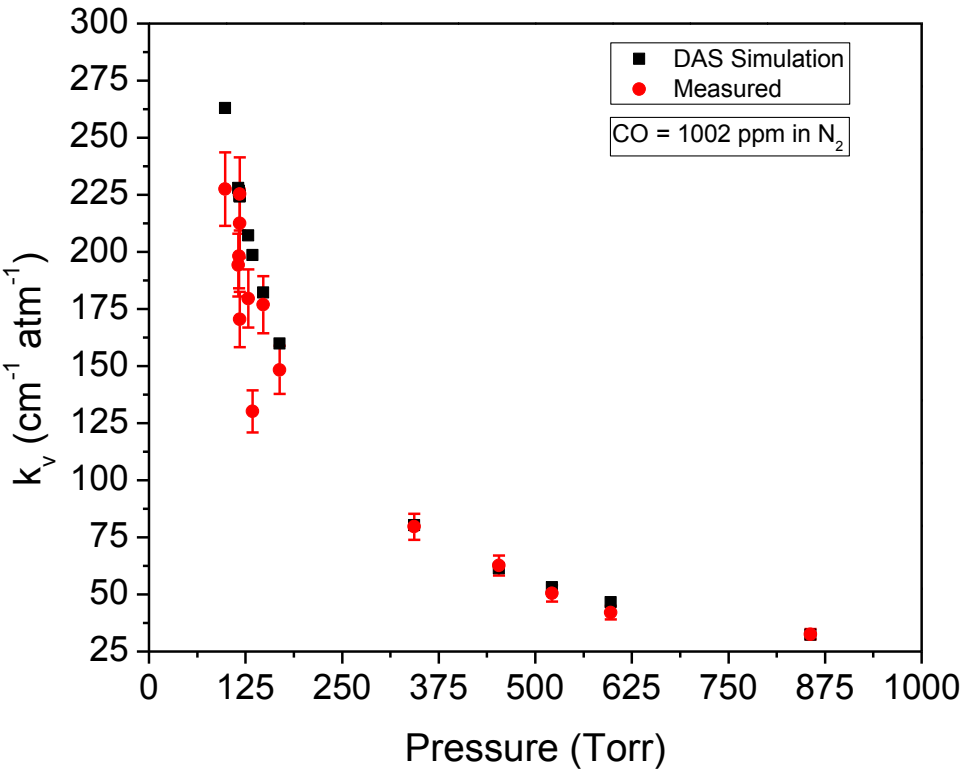

Figure 46 CO absorption coefficient comparison between measured and calculated values using 0.1 % CO/N_2 (vol.) mixture.

Figure 47 illustrates the calculated spectral variation of the CO absorption coefficient for the known CO/N_2 mixture. Based on the laser mode-jumps discussed in A.1 and observation in Figure 46, the wavenumber/wavelength uncertainty was measured to be ± 0.008 cm^{-1} (± 0.01625 nm). This uncertainty was based on the wavenumber increment selected to be 0.004 cm^{-1} for the DAS simulations. The lowest wavenumber increment that can be selected was dictated by the absorption line-strength spectral resolution provided by HITRAN 2004 database (Rothman, 2005). The measured

wavenumber/wavelength uncertainty was measured as the maximum standard deviation recorded for every absorbance measurement taken. Smaller laser mode-jumps have been recorded and are within the reported wavelength uncertainty. This uncertainty in operating wavelength was applied to the total uncertainty analysis of the CO concentration measurements by accounting for the deviation in the absorption coefficient illustrated in Figure 47. The large deviations in the measured absorbance and absorption coefficient at lower mixture pressures (118 and 169 torr) are due to the combination of the thinner spectral lines and wavelength uncertainty. The laser mode-jump has less of an effect at higher mixture pressures since the spectral lines are more broadened. Therefore, the calibration procedure provides a finer wavelength-tuning at lower mixture pressures.

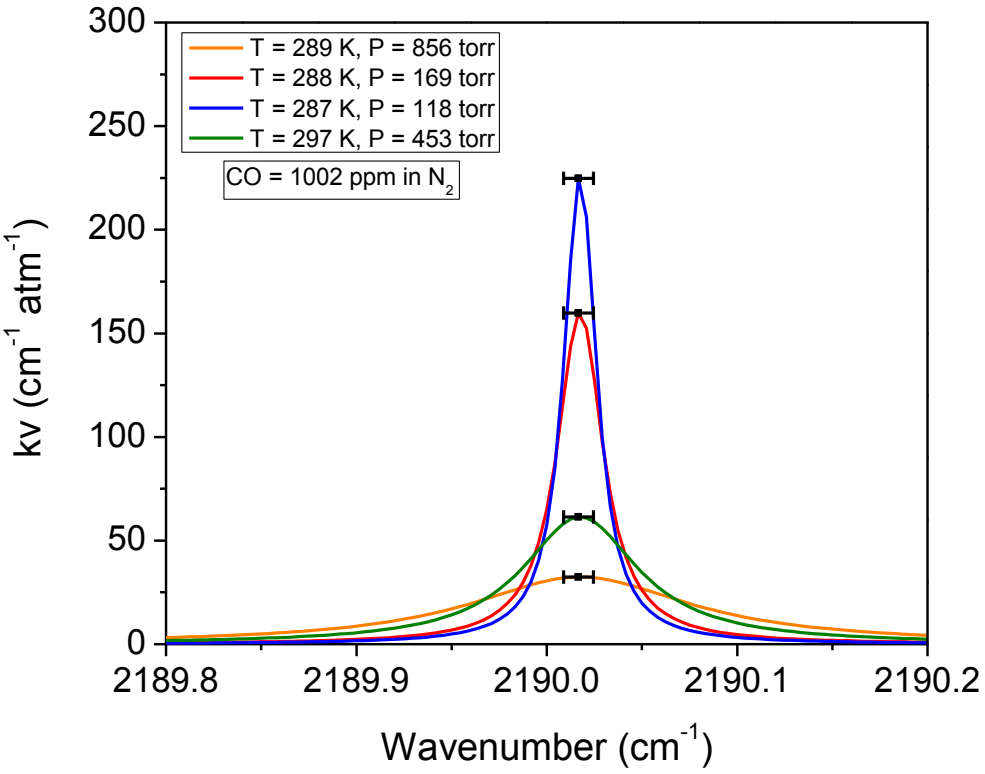

Figure 47 Spectral variation of absorption coefficient and wavenumber uncertainty due to laser mode-jumps.

The calibration procedure was also performed after the combustor rig performance tests to verify operating wavelength and identify any laser mode-jumps. As discussed in A.1 of the Appendix, the CO concentration uncertainty can be reduced by operating in a more stable laser condition observed at 400 mA and -20˚C. Having the mid-IR diagnostics equipment outside (ambient conditions) made it difficult to fix the thermal load since the ambient temperature fluctuates. Ambient temperatures have been recorded around 100˚F during mid-IR absorption measurements. As mentioned in the

previous chapters, the external cooling system of the QC laser is a passive cooler. Although this cooler is capable of accessing the ideal stable condition of the QC laser at high ambient temperatures, the cooling system can be improved by installing an active cooler for better performance that will reduce the thermal load while operating at a more-stable condition.

5.2.2 CO concentration measurements during combustor rig performance tests

Figure 48 illustrates the CO concentration for one of the rig performance (hot-fire) tests. The rig temperature, pressure, and equivalence ratio are also plotted. The CO ppm levels shown were taken from the CAI analyzer and the IR diagnostics at 4.5 μm. The parameters EM1 and EM2 from the CAI analyzer correspond to the high-ppm CO range and low-ppm CO range, respectively. The parameter EM2 is used for a more accurate CO concentration measurement at low-ppm levels. Ignition occurs around 6 s dictated by the rig temperature and pressure. There is about a 3-s delay in the mid-IR diagnostics from the time of ignition. The CAI analyzer shows about a 12-s delay due to the sample gas conditioning for H_2O removal. An initial CO spike is shown from ignition causing EM2 to saturate, then gradually decreases to a stable condition between 75 -100 s. This stable condition is taken with respect to the equivalence ratio stabilizing around 0.74. Figure 49 shows the rig flame-out occurring around 107 s.

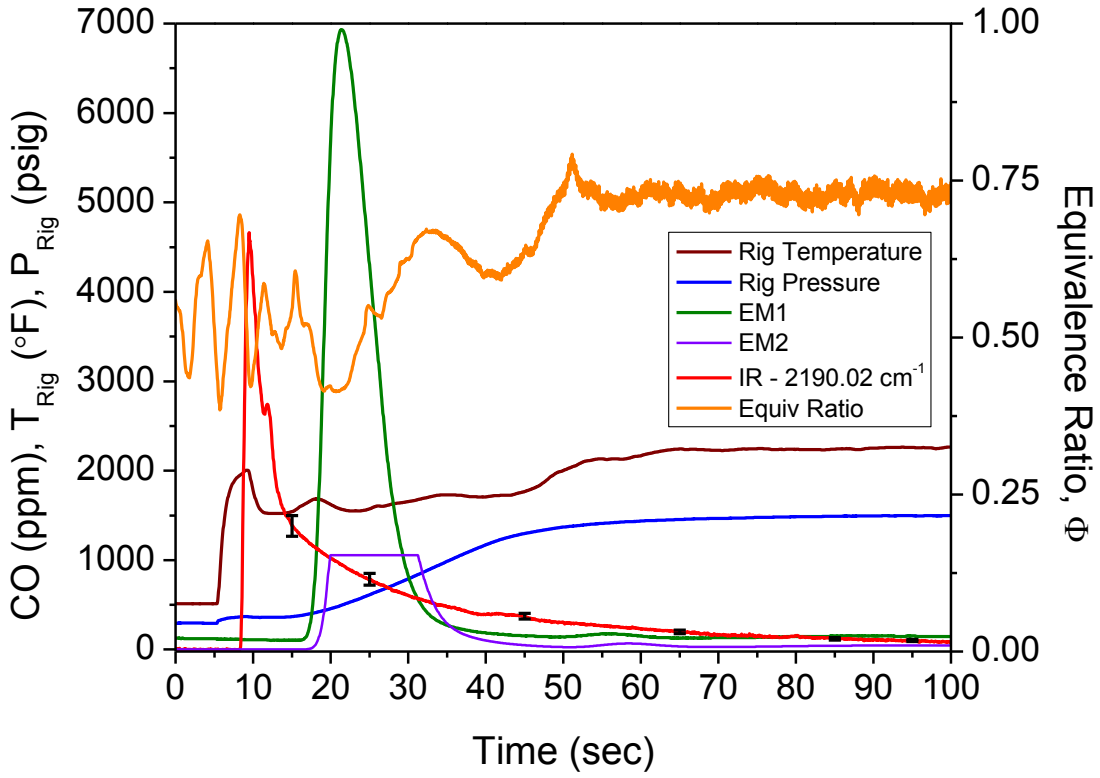

Figure 48 Combustor rig performance (hot-fire test). Stable rig conditions are shown from 75 – 100 s.

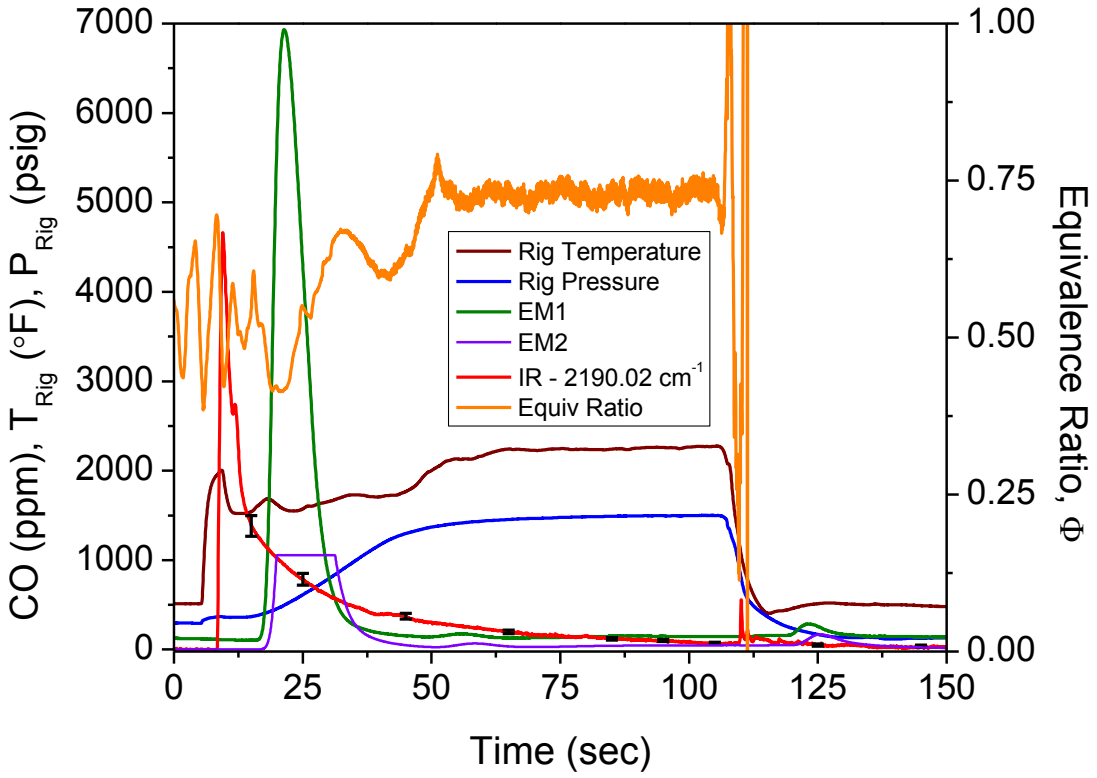

Figure 49 Flame-out occurred around 107 s during hot-fire test. The CO emission shows a spike in concentration due to combustion flame-out.

Figure 50 illustrates the baseline signals from the IR diagnostics and CAI analyzer before ignition. The baseline signal from EM1 shows an offset of about 125 ppm while EM2 shows a baseline of approximately 0 ppm. This is due to the lower-ppm limit from EM2 resulting in a more accurate reading at lower ppm levels. The baseline from the mid-IR diagnostics also marks approximately 0 ±10 ppm. It is crucial to record the baseline mid-IR signals prior to any performance test to validate the mid-IR

absorption diagnostics. It is also necessary to record the baseline after the hot-fire to gauge any baseline-shifts due to laser drifts.

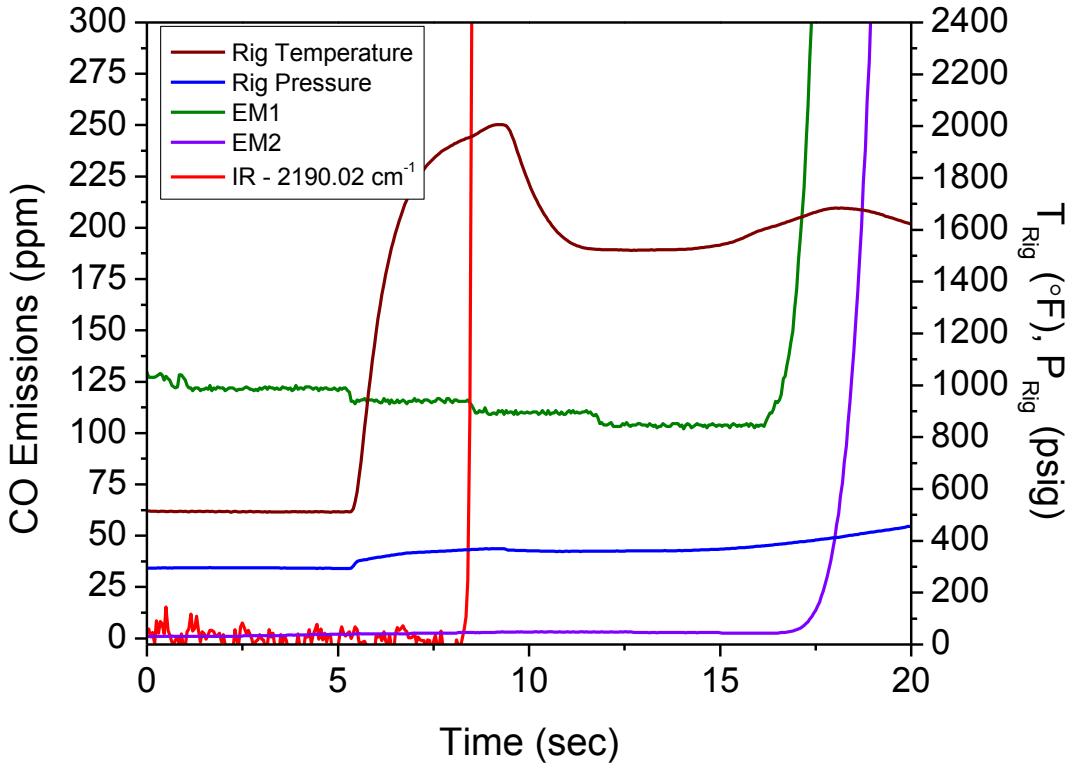

Figure 50 Baseline emission signals prior to ignition. EM2 and mid-IR sensor show stale baseline signals around 0 ppm. EM1 shows a 125-ppm offset due to its lower accuracy at low ppm levels.

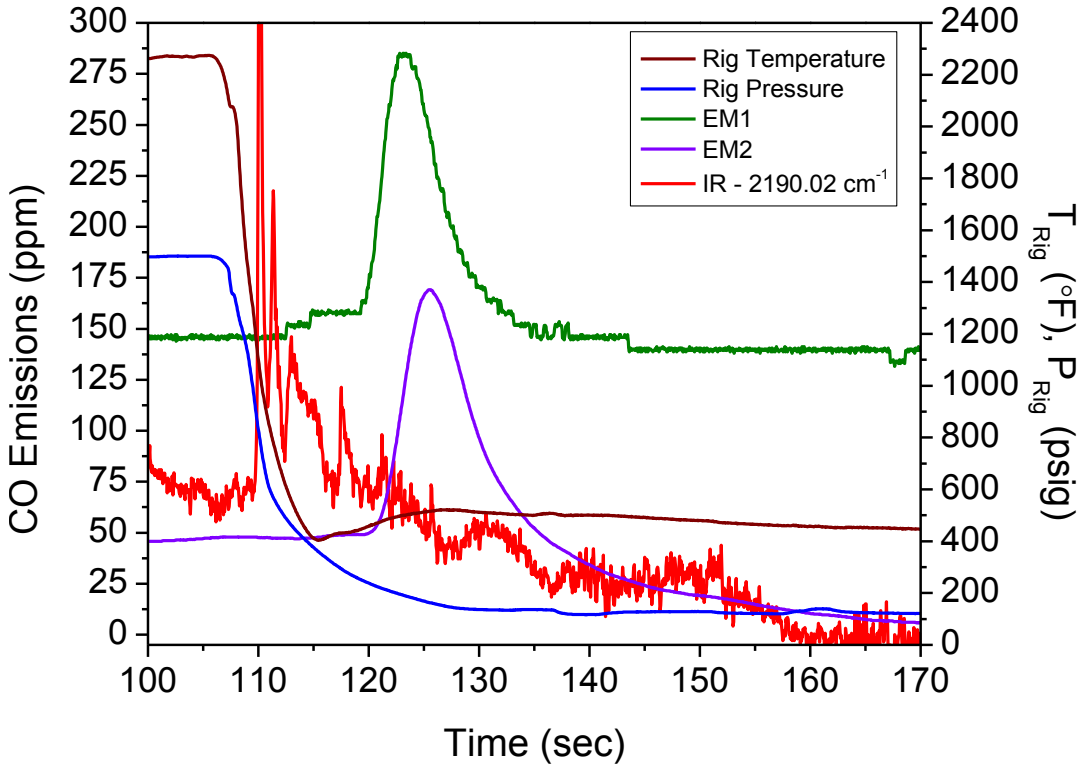

Figure 51 Emission signals after rig flame-out.

Figure 51 shows the CO emission signals returning to their baseline, confirming minimal baseline shifts. EM1 shows a ppm level slightly higher than its baseline due to its lower accuracy at low-ppm levels. All three CO concentration measurements show a peak towards the end of the performance test. This slight increase in CO ppm levels is likely due to incomplete hydrocarbon combustion characteristics during flame-out.

Figure 52 shows the CO concentration from 75 to 110 s. This time interval was selected to observe the emission during stable rig conditions dictated by the rig pressure

and temperature. Figure 53 zooms in on the last stable time interval before flameout. The 3-s delay on the mid-IR diagnostics can be seen from the point of flameout around 107 s. At 85 s, the mid-IR sensor measured the CO concentration to be 120 ppm ±15 ppm. The CO concentration was measured to be 102 ppm ± 14 ppm at 95 s and 67 ppm ±12 ppm at 105 s. The relative uncertainty seems to be increasing as the IR signal reaches a stable condition between 100-108 s due to the reduction in SNR caused by lower laser attenuation (lower IR signal absorption).

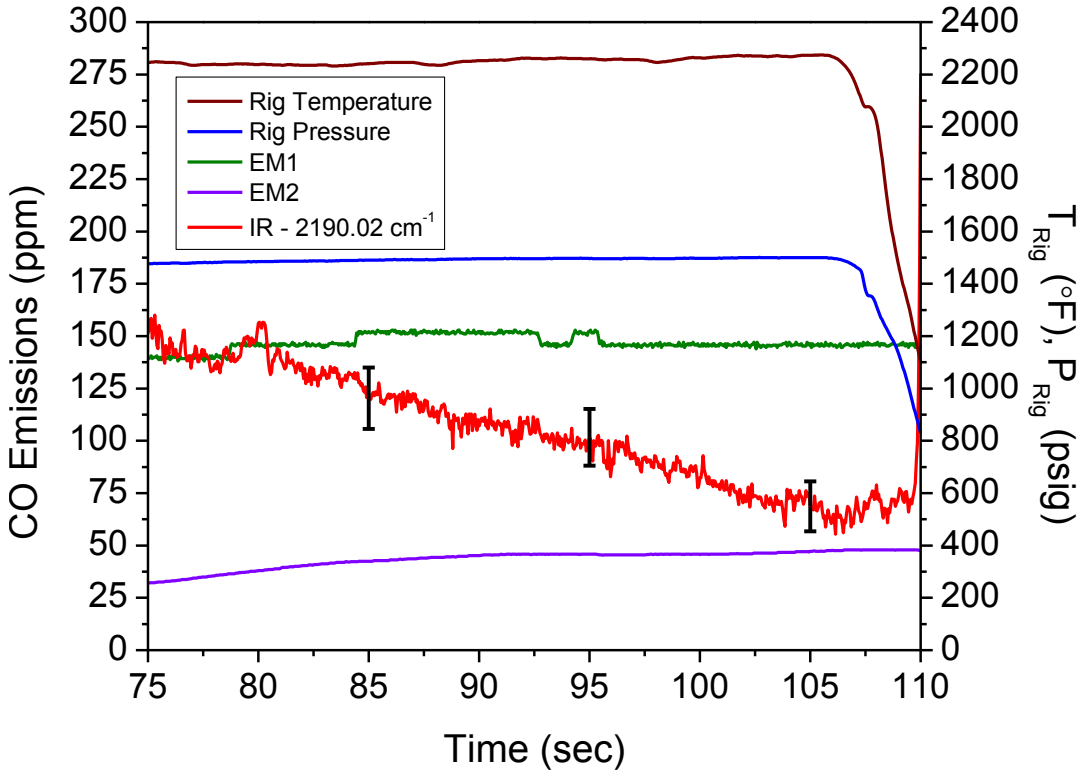

Figure 52 CO emissions during stable rig conditions from 75 – 110 s.

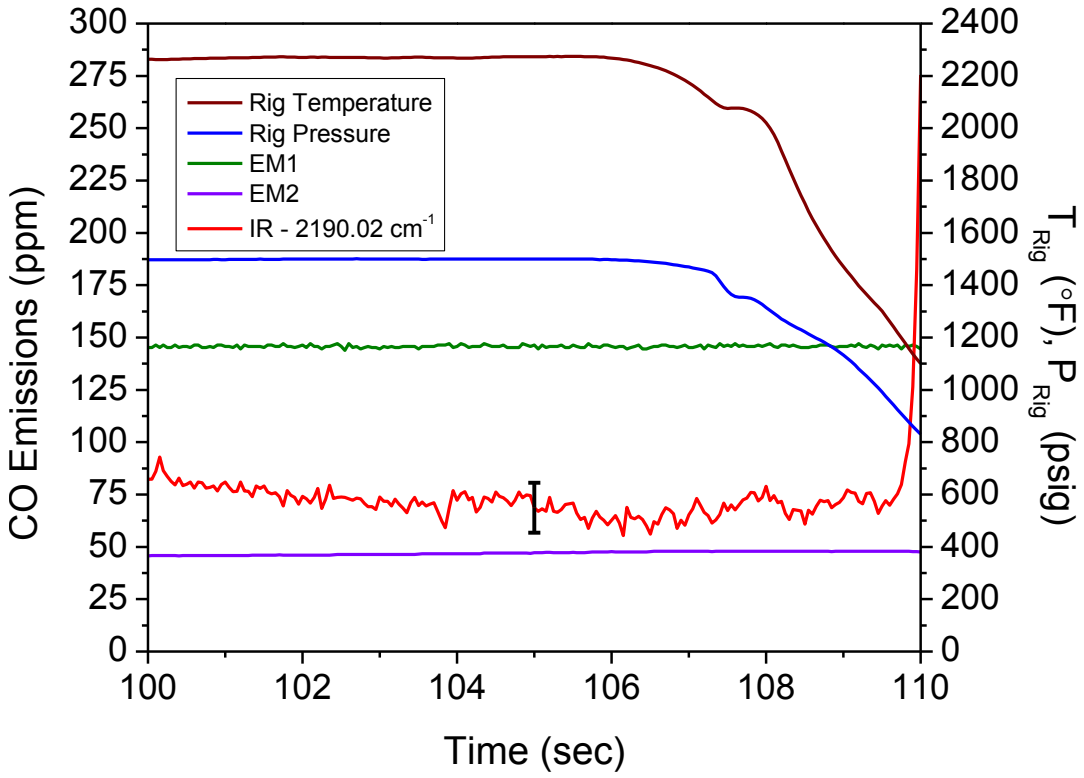

Figure 53 CO emissions during stable rig conditions from 100 – 110 s.

Figure 54 illustrates the raw mid-IR signals during the hot-fire test. The sample gas pressure measured inside the absorption cell is also plotted. A slight decrease in sample gas within the absorption cell is noticed at the point of ignition. The slight pressure-drop may be due to the combustion gases over-expanding as they exit the exhaust. Choked-flow conditions are reached at the exhaust throat causing the combustion gases to reach supersonic conditions at the exhaust exit. The combustion gases continue to expand as they reach relatively high Mach numbers even at 12 in from

the exhaust exit. The absorption cell pressure gradually increases as the rig reaches stable conditions. The rig flame-out is observed from the absorption cell pressure. The absorption cell pressure is slightly higher at the end of the hot-fire compared to the pressure before ignition due to the absence of any gases flowing after flame-out.

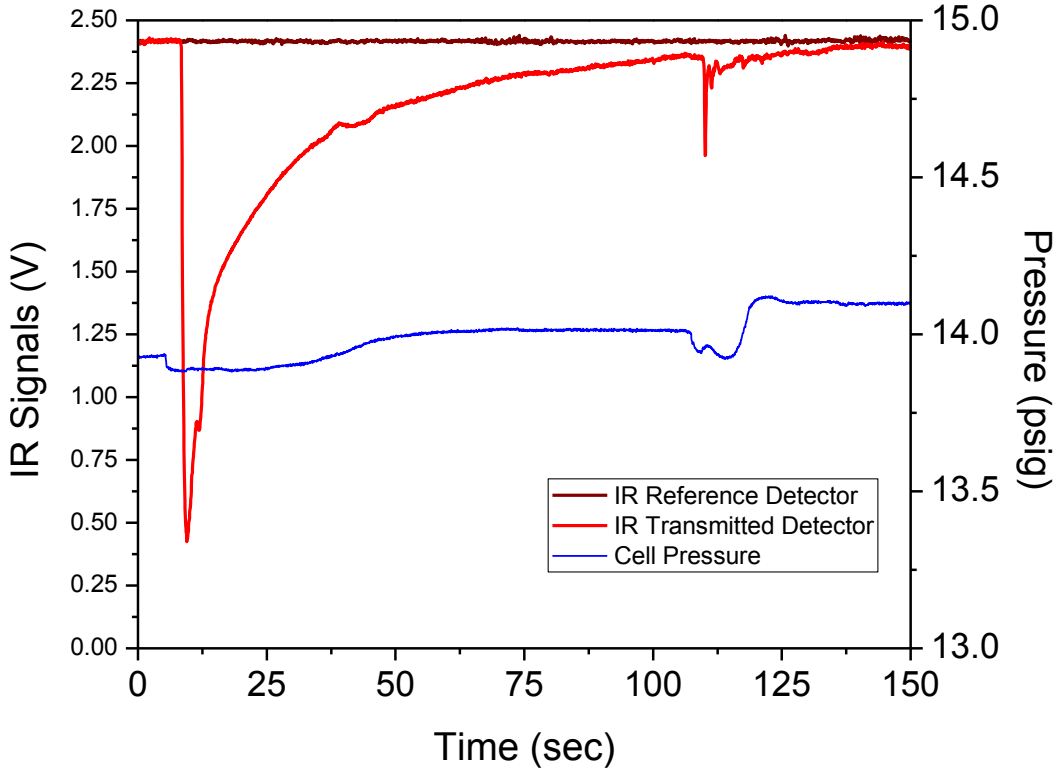

Figure 54 Raw IR signals and absorption cell pressure during a hot-fire test. The rig flame-out is observed from the absorption cell pressure trace.

Figure 55 and Figure 56 illustrate the CO absorbance and absorption trace, respectively. Figure 55 also shows the absorption cell temperature as the sample gas flows through the cell. Temperature changes in the absorption cell seem to be negligible during hot-fire tests. Figure 56 shows the peak absorption to be approximately 83% at the point of ignition. The mid-IR absorption from CO gradually decreases to approximately 2.5% absorption at stable rig conditions from 100 to 110 s.

The operating wavelength was verified after the hot-fire test to confirm the 2.5% absorption from CO to be within ± 0.008 cm^{-1} (± 0.01625 nm) from the R(12) transition at 2190.01667 cm^{-1} (4.56618 μm). It is important for the QC laser to operate at or near the selected transition to maximize the CO sensitivity and SNR as shown in Table 1 which tabulates the variation of CO concentration with absorption and absorbance. At the given rig conditions and 2.5% absorption from CO shown above, lowering the CO sensitivity of the mid-IR diagnostics would reduce the SNR and accuracy.

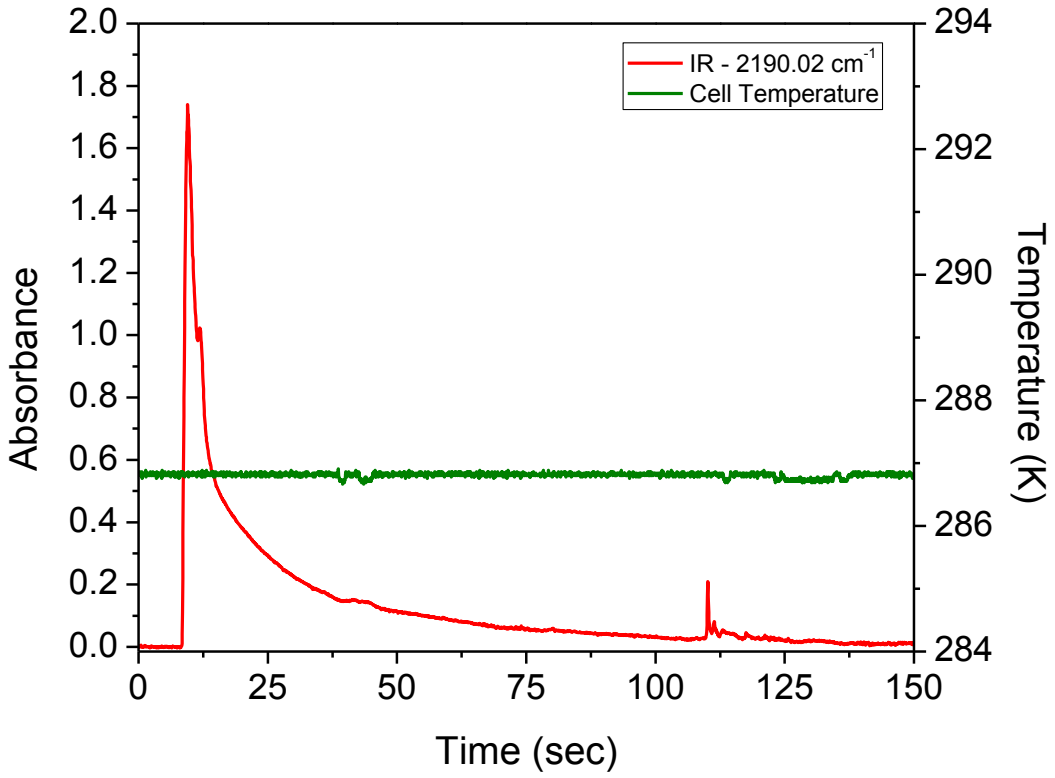

Figure 55 CO absorbance trace and absorption cell temperature during the rig hot-fire test. The temperature within the absorption cell does not seem to change throughout the entire test.

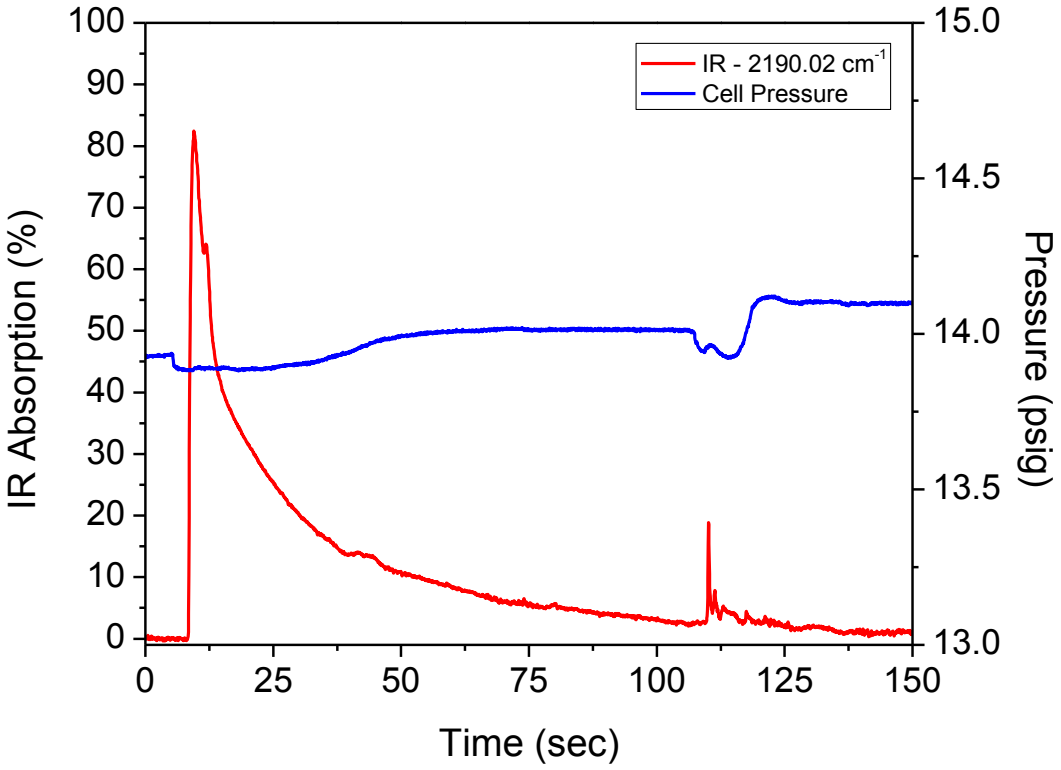

Figure 56 Mid-IR absorption (%) from CO emissions and absorption cell pressure. Absorption of 2.5% from CO was measured at stable rig conditions.

Table 1 Variation of calculated CO concentration with IR absorption and absorbance.

Absorption (%)	Absorbance	X_{CO} (ppm)
0	0.00	0.00
2.5	0.03	67.38
20	0.22	593.83
30	0.36	949.19
40	0.51	1359.42
50	0.69	1844.62
80	1.61	4283.07
99	4.61	12255.37

One major uncertainty factor during the rig hot-fire tests was possible condensation of water from the combustion products within the sample line. Condensation within the mid-IR sample line has been confirmed and needs to be eliminated for accurate CO measurements. As discussed in Chapter 2, the absorption coefficient is dependent on the gas composition. Condensation within the lines will make the gaseous H_2O content unknown while liquid H_2O may absorb or scatter a portion of the IR light leading to an incorrect CO concentration measurement. An equilibrium analysis of the rig combustion process was performed to estimate the combustion gas mole fractions at equilibrium based on the rig conditions. Figure 57 illustrates the fuel and oxidizer mass flows entering the combustor rig prior to ignition. The average inlet rig temperature was 515 K based on the mass flow shown below. Based on the inlet mass flows, the inlet reactant composition was calculated to be 8.5% CH_4 / 22.5% O_2 / 69% CO_2 (vol.).

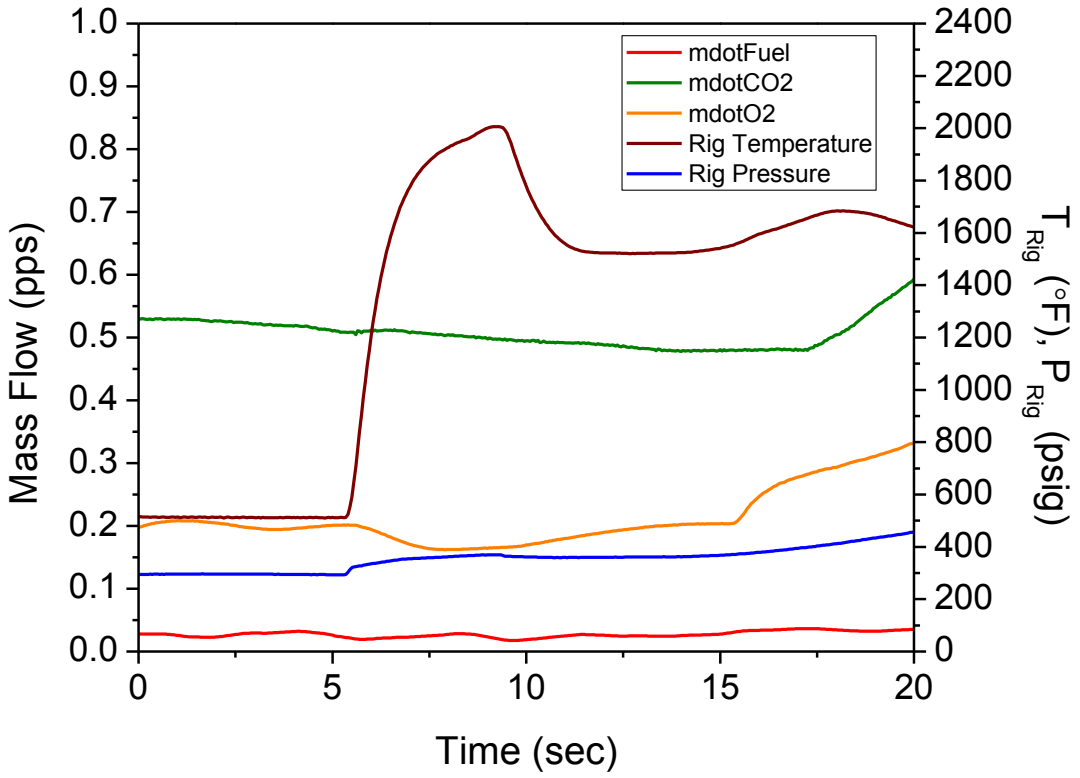

Figure 57 Fuel and oxidizer flows including rig pressure and temperature. The mass flows are measured in pounds per second (pps).

The equilibrium analysis was done using the GRI 3.0 mechanism (Smith et al., Berkely). Figure A. 4 in the appendix illustrates the calculated CO concentration at equilibrium and adiabatic flame temperature with varying inlet temperature at a constant pressure of 103.4 bar. The analysis was performed with constant enthalpy and pressure (HP). Both dry and wet analyses were performed to compare the CO concentrations. The H_2O presence is more prominent at higher inlet temperatures as shown in Figure A. 4. Figure 58 illustrates the calculated CO absorption coefficient variation with reactant inlet

temperature based on the wet and dry equilibrium analysis. The CO absorbance based on the calculated wet and dry CO concentrations at equilibrium is also plotted as a function of reactant inlet temperature. The presence of H_2O in the mixture causes a noticeable difference in the CO absorption coefficient. There seems to be very little change in the CO absorption coefficient for wet or dry conditions with varying inlet temperature at a constant pressure of 103.4 bar.

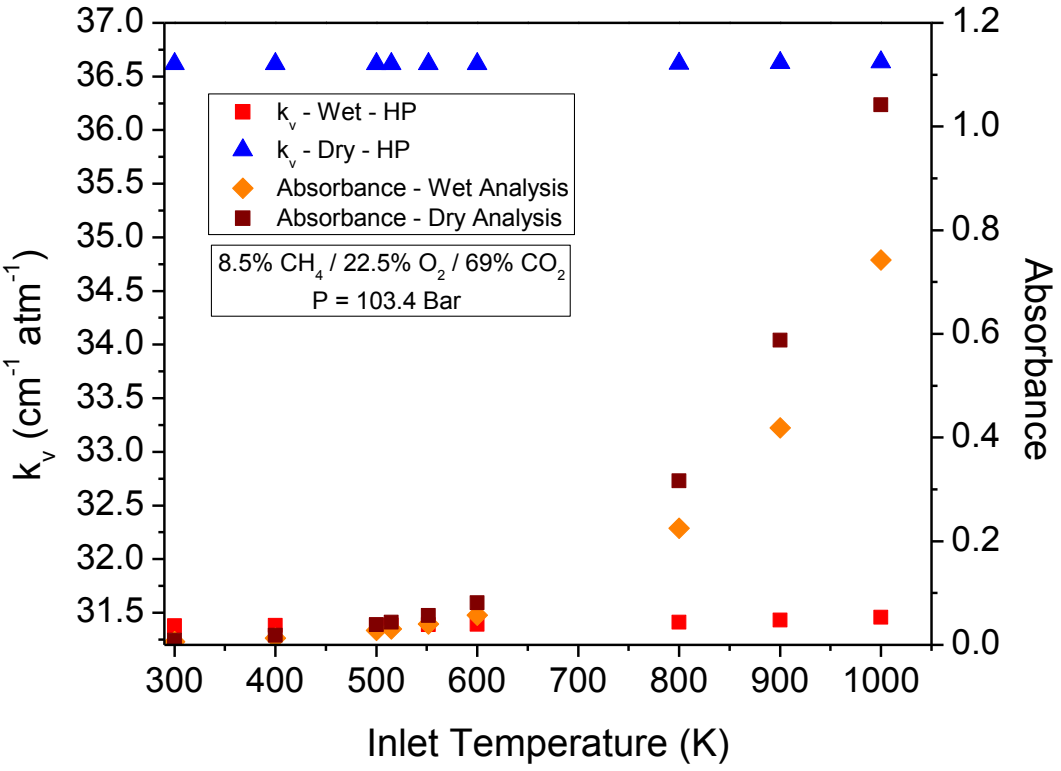

Figure 58 CO absorption coefficient variation and absorbance with reactant inlet temperature based on equilibrium conditions.

Figure 59 illustrates the spectral variation of the CO absorption coefficient for the wet and dry-based compositions centered at 2190.02 cm^{-1}. The product gas equilibrium composition calculated with an inlet temperature of 515 K was used for Figure 59. Table A. 3 and Table A. 4 tabulate the wet and dry equilibrium major product gas compositions, respectively.

The H_2O mole fraction was calculated to be approximately 0.17. The conditions used for calculating the absorption coefficient were 287 K and 96 kPa which represent the conditions of the absorption cell during the hot-fire test. The two cases shown in Figure 59 represent the sample gas with the absence and presence of H_2O in complete gaseous form. The CO absorption coefficient will fall within the two peaks shown in Figure 59 by varying the H_2O mole fraction between 0 and 0.17.

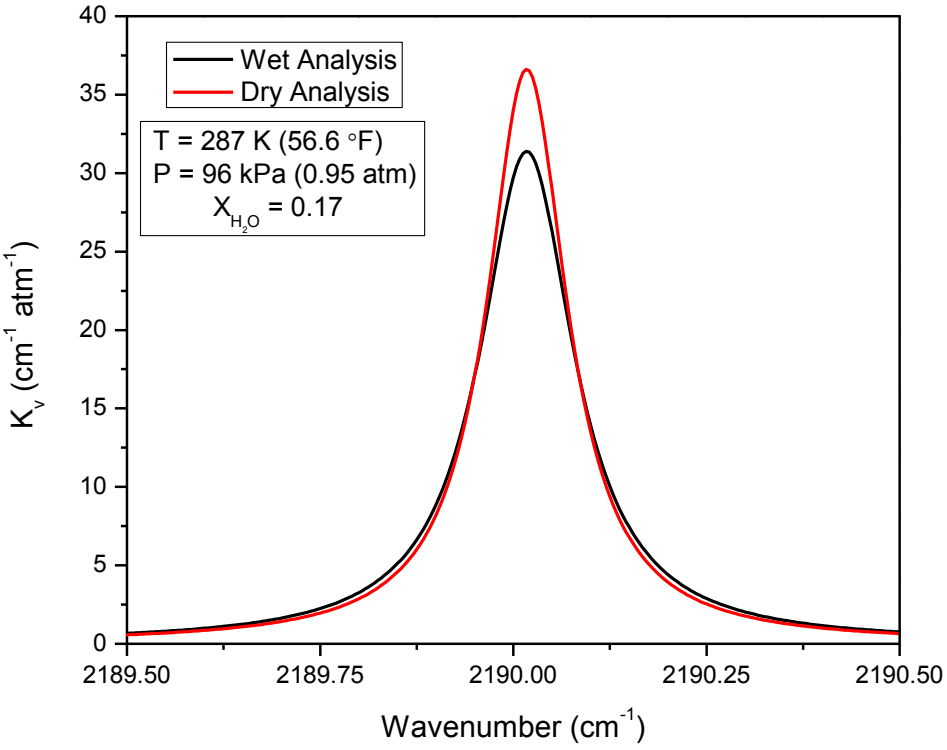

Figure 59 CO absorption coefficient spectral variation using equilibrium composition at a temperature and pressure of 515 K and 103.4 bar. The DAS convolution was performed at 287 K and 96 kPa.

Figure 60 and Figure 61 illustrate the CO concentration measurements using the wet, dry, and combined-based calculated absorption coefficients. The wet- and dry-based absorption coefficients were taken from Figure 59, while the combined-based absorption coefficient was calculated using an average of both equilibrium cases. A CO-concentration offset is shown between the three mid-IR measurements due to their difference in calculated absorption coefficient.

The dry- and wet-based mid-IR measurements do not accurately reflect the true concentration measurement due to their observed absorption and concentration calculations shown in Table 2. The measured wet-based CO concentrations are shown to be higher than the dry-based measurements. This result is due to the CO absorption coefficient adjustment without adjusting the mid-IR measured absorbance. Additional hot-fire tests need to be performed with the absence and presence of complete gaseous H_2O to properly measure the mid-IR absorbance in addition to using the proper CO absorption coefficient.

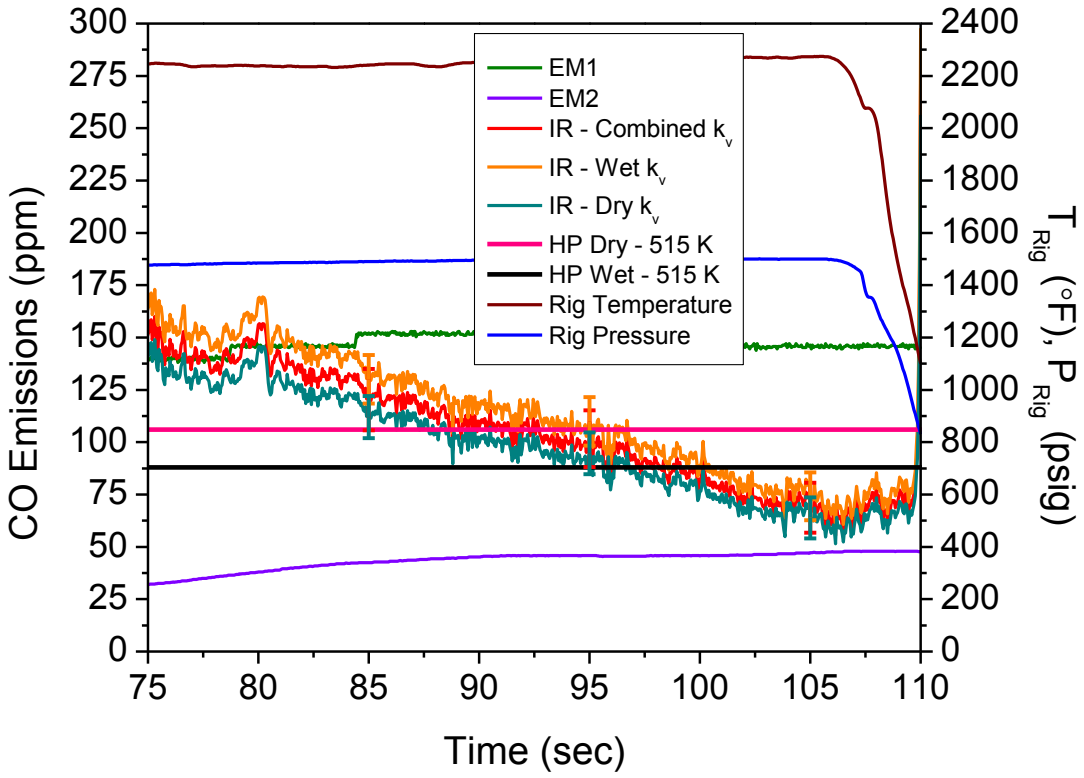

Figure 60 CO emissions using the calculated combined, wet and dry absorption coefficient during stable rig conditions from 75 – 110 s.

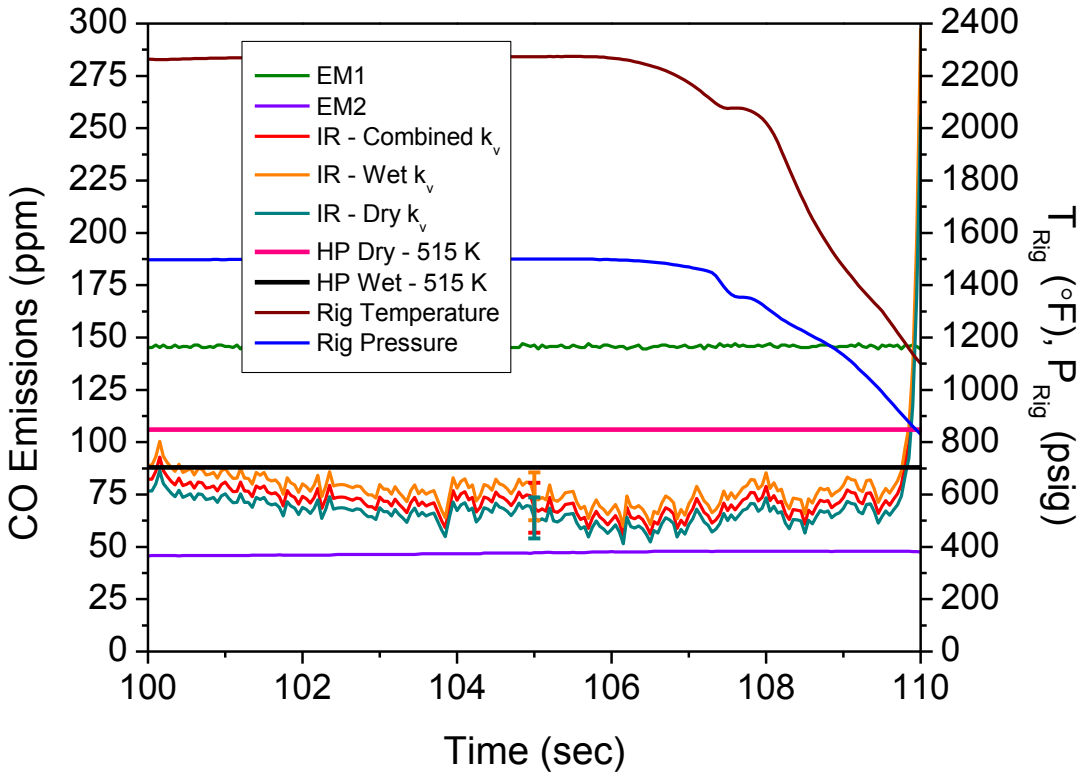

Figure 61 CO emissions using the calculated combined, wet and dry absorption coefficient during stable rig conditions from 100 – 110 s.

Table 2 Variation of measured CO concentration using the calculated combined, wet and dry-based CO absorption coefficient.

Absorption (%)	Absorbance	X_{CO}-Combined (ppm)	X_{CO}-Wet (ppm)	X_{CO}-Dry (ppm)
0	0.00	0.00	0.00	0.00
2.5	0.03	67.38	72.82	62.69
20	0.22	593.83	641.79	552.55
30	0.36	949.19	1025.84	883.20
40	0.51	1359.42	1469.20	1264.91
50	0.69	1844.62	1993.58	1716.37
80	1.61	4283.07	4628.95	3985.29
99	4.61	12255.37	13245.05	11403.33

The unknown H_2O content during the hot-fire test adds uncertainty to the CO concentration measurements due to the difference in calculated absorption coefficients. The main factors contributing to uncertainty in the CO concentration are uncertainties in the signal difference, ΔI, and the absorption coefficient, k_v. Section A.3 of the Appendix presents the uncertainty analysis for the measured CO concentration. The uncertainty within the absorption coefficient, u_{kv}, used for the X_{CO}–combined case was calculated to be approximately 8.2%. The source of this uncertainty is the deviation in absorption coefficient value between the dry and wet analysis. Optimizing the mid-IR diagnostic setup to measure true dry-based or wet-based CO concentrations will reduce the total CO concentration uncertainty, U_{Xco}, by approximately 14% due to the scatter reduction in the calculated absorption coefficient.

Figure 62 shows another combustor rig hot-fire test. This hot-fire test is presented to show the CO emission signal limitations for the mid-IR diagnostics and the CAI analyzer. However, the mid-IR saturation shown in Figure 62 does not correspond to the limit tabulated in Table 2. The mid-IR absorption shown in Figure 63 shows a signal offset of approximately 7.5% prior to ignition. This offset causes the absorption to reach 100%. By correcting the baseline, the maximum absorption drops to approximately 90% illustrated in Figure 64. However, the CO concentration measurements from EM1 show a CO concentration greater than 21000 ppm. The mid-IR sensor failed to show the true maximum CO ppm level due to its premature full laser attenuation. Additional CO concentration measurements need to be taken close to the mid-IR sensor limit to verify the maximum CO concentration. Any mid-IR signal offsets need to be corrected prior to rig tests.

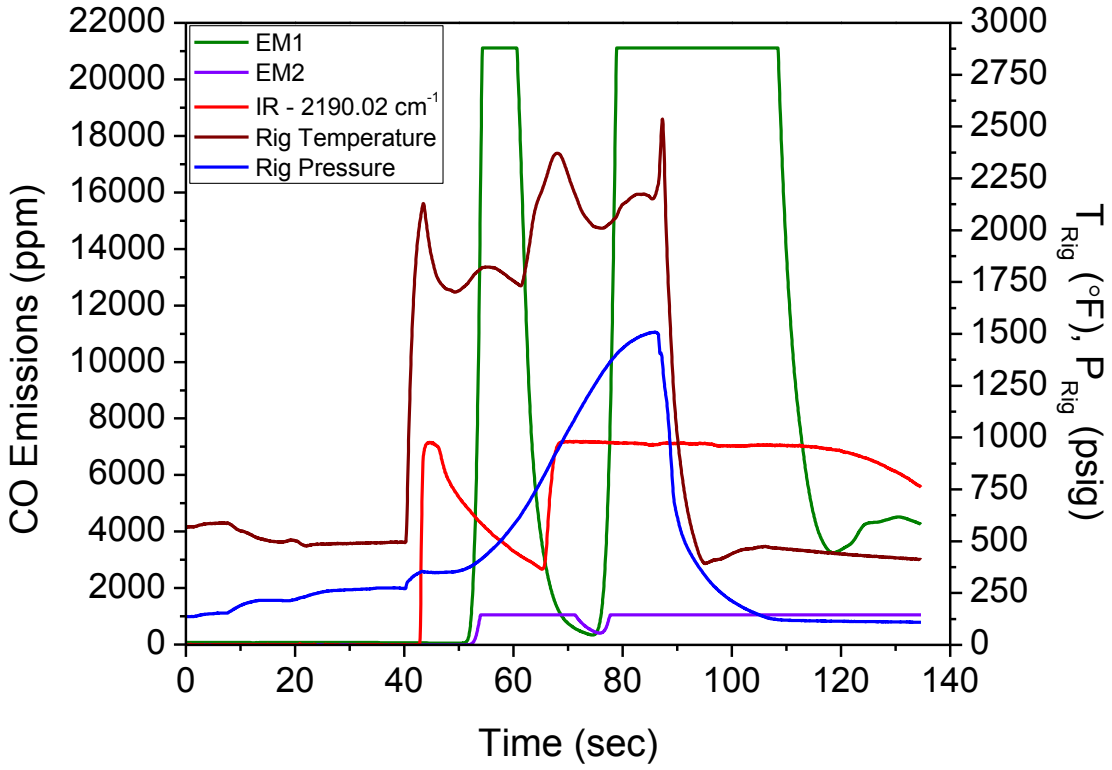

Figure 62 Combustor rig hot-fire test showing CO emissions signal saturation. This hot-fire test was one of many hot-fire tests performed on the combustor rig.

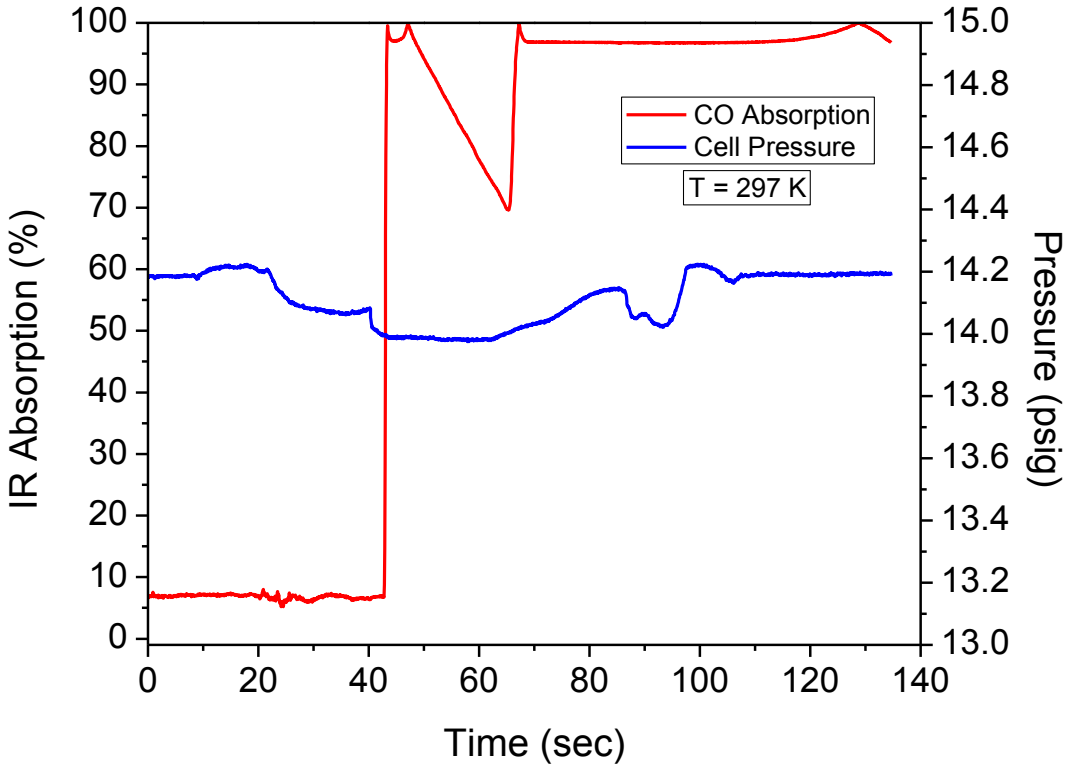

Figure 63 Mid-IR absorption due to CO showing an offset in baseline prior to ignition. The pressure within the absorption cell is also plotted.

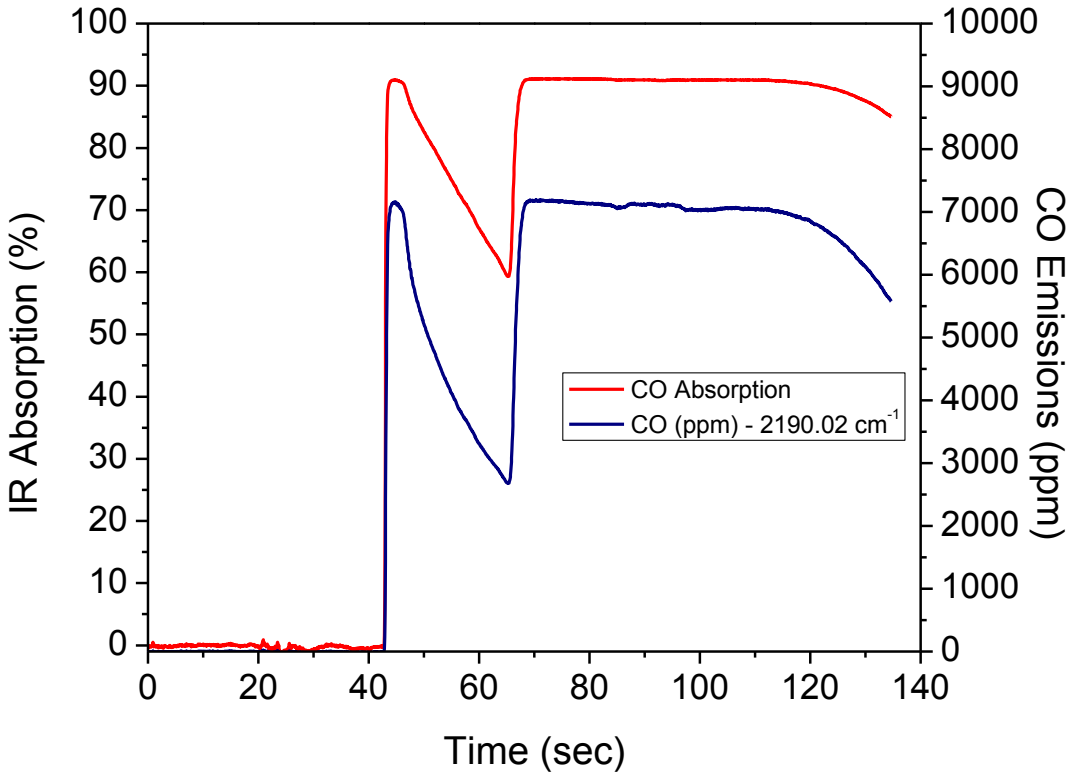

Figure 64 Corrected IR absorption baseline prior to ignition. Correcting the baseline lowers the maximum absorption while still showing IR signal saturation characteristics.

Figure 65 and Figure 66 illustrate the mid-IR CO absorbance trace along with the rig conditions and absorption cell pressure, respectively, for a third hot-fire test. As shown in these figures, ignition occurs around 40 s. A series of flame-out and re-ignition events occur between 50 s – 130 s. The mid-IR CO concentration measurements are not shown due to a greater amount of condensation within the sample line as a result of an added heater element between the emissions probe and the mid-IR diagnostics. The addition of the heated element was installed to prevent condensation by keeping the

sample gas temperature above the condensation point of H_2O. However, this installment allowed more condensation to occur within the un-heated section of the sample line entering the mid-IR diagnostics. Nevertheless, the mid-IR absorbance trace successfully captured the transient combustion conditions within the rig. The mid-IR absorbance needs to be compared to the reactant flows in order to determine the exact flame-out and re-ignition times.

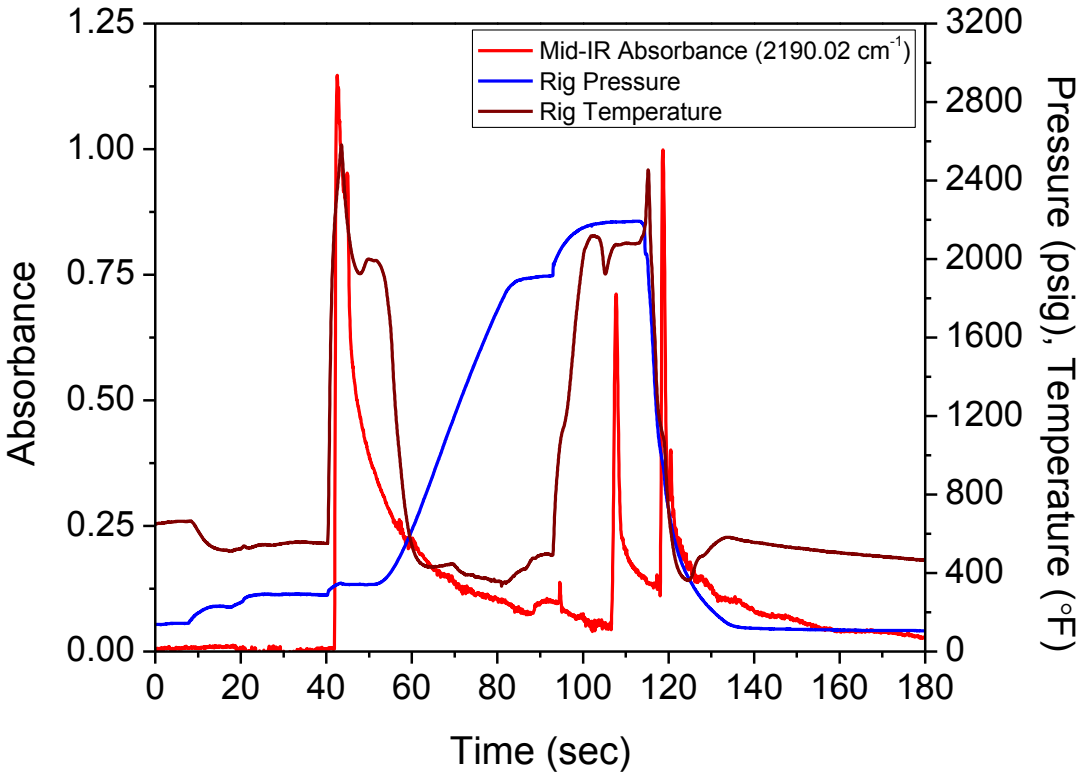

Figure 65 Mid-IR CO absorbance trace during a third hot-fire test along with the rig pressure and temperature. The mid-IR diagnostics successfully capture rig ignition and flame-out events.

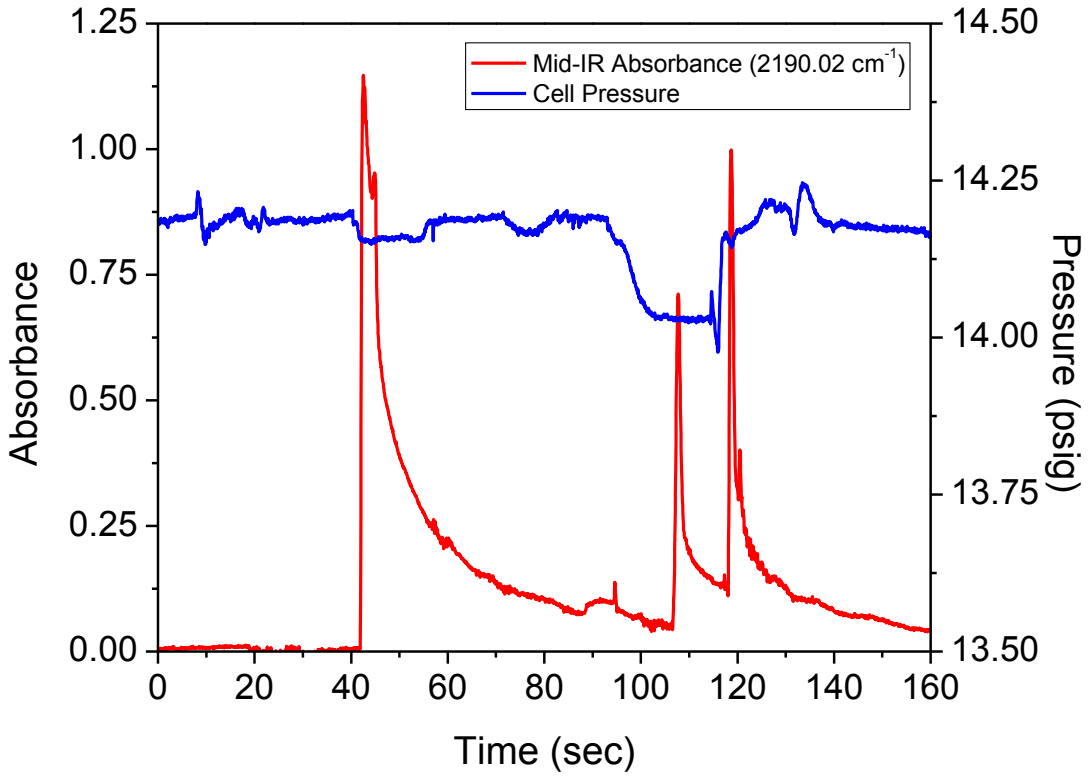

Figure 66 Mid-IR CO absorbance trace and absorption cell pressure during a third hot-fire test. The absorption cell pressure is shown to capture the rig ignition and flame-out events.

5.3 Fuel concentration measurements using IR diagnostics at 3.39μm

As discussed in Chapter 3, the mid-IR sensor was adapted to measure the fuel concentration during cold-flow rig tests to validate its use for future UHC measurements. The spectroscopy parameters of CH_4 were used for the mid-IR fuel concentration measurements since the natural gas used was mainly comprised of CH_4. The fuel concentration calculations are found in section A.4 of the Appendix.

The fuel was measured during cold-flow tests for the adjustment of flow ramp control. These tests were performed to adjust the gain controls for the fuel and oxidizer valves in order to have better flow control during hot-fire tests. Figure 67 illustrates the reactant and rig coolant flows during a cold-flow test. As mentioned in Chapter 3, the combustor rig contains CO_2 and N_2 coolant circuits within the rig that exit the exhaust nozzle with the combustion gases. Although the CFD analysis developed by PSI predicts no N_2 coolant gas flowing into the emissions probe, it is of interest to validate the CFD model to see if N_2 gas is truly flowing through the sample gas line.

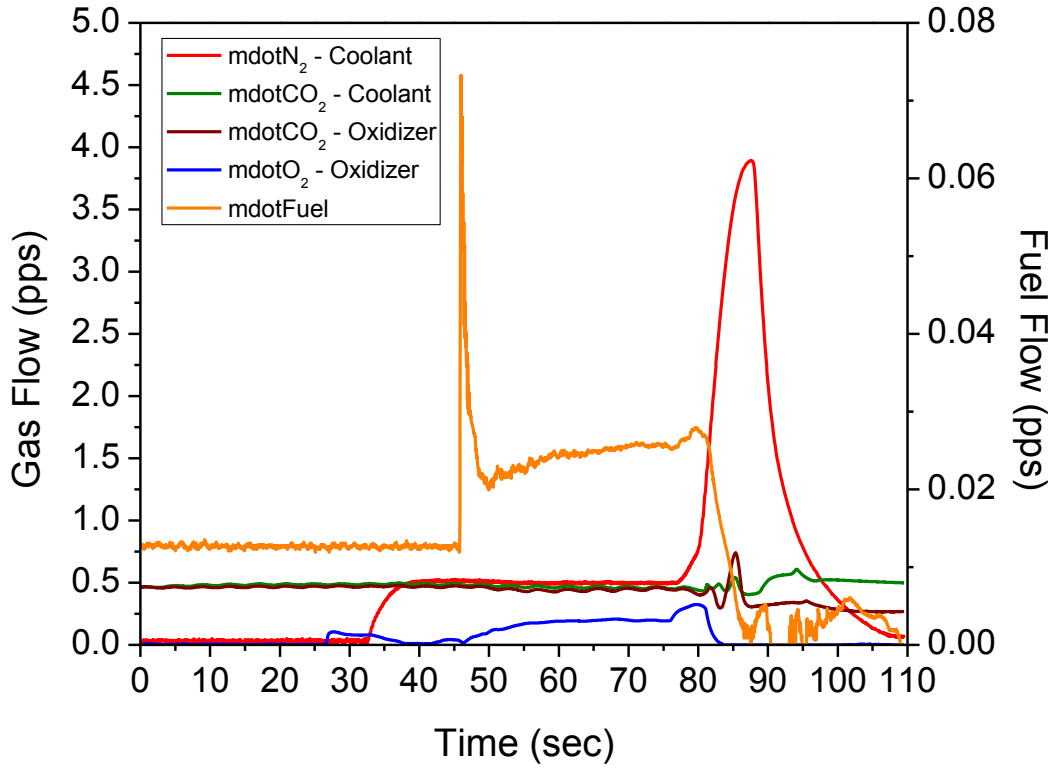

Figure 67 Combustor rig gas flows in pounds per second for cold-flow 1 (CF-1). This set of cold-flow data is used to gain better flow ramp control.

Figure 68 illustrates the fuel concentration based on the fuel flow and the UHC analyzer channel EM4. The fuel flow taken from the cold-flow test was converted to a mole fraction for two cases: fuel flowing through the sample gas line with N_2 as a constituent and fuel flowing without N_2 gas in the mixture. To validate this prediction, the UHC analyzer is compared to the two calculated fuel concentrations based on the gas flows.

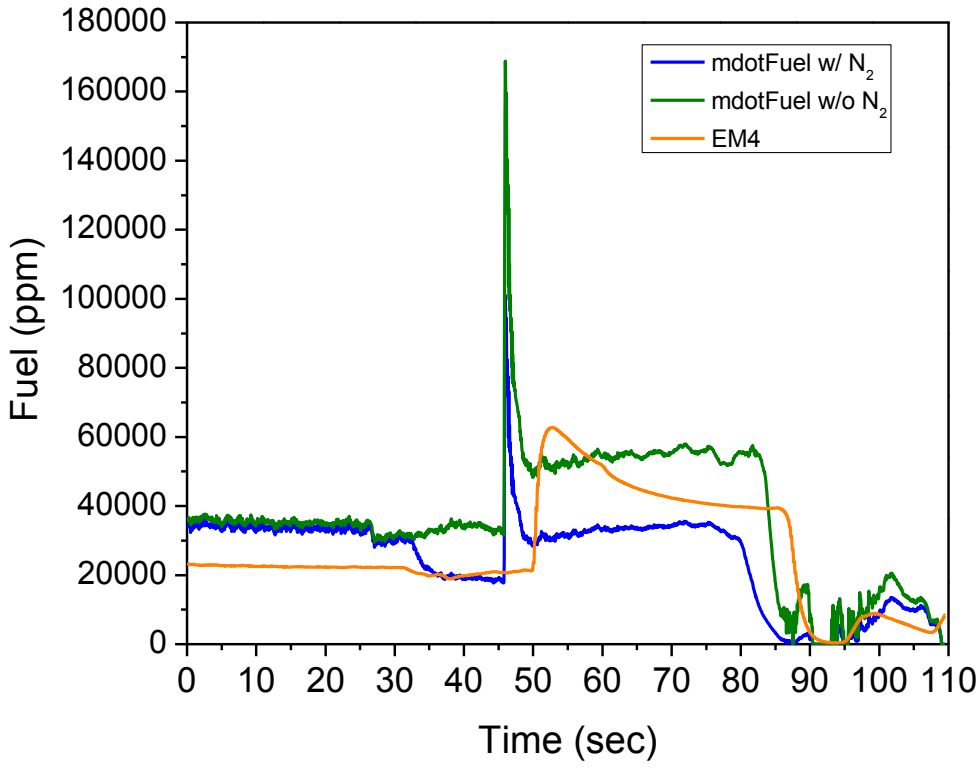

Figure 68 Fuel flow concentration measurements from the UHC analyzer (EM4) and the fuel flow for CF 1. The fuel mass flow is converted to a mole fraction for a composition with N_2 within the gas mixture and a composition without N_2.

Channel EM4 seems to be under-predicting the concentration between 0 and 30 s and over-predicting between 50 and 80 s compared to the calculated fuel concentration with N_2. There is about a 4-s time-delay for the EM4 measurement. Figure 69 illustrates the mid-IR signal absorption with the two calculated fuel concentrations. The mid-IR absorption trace indicates good signal response with the fuel flow changes. By looking at the mid-IR absorption trace and recognizing the drop-step in absorption between 33 and

45 s, it seems like there may be N_2 flowing through the emissions system. This conclusion is justified by looking at the jump in N_2 flow around 33 s shown in Figure 67.

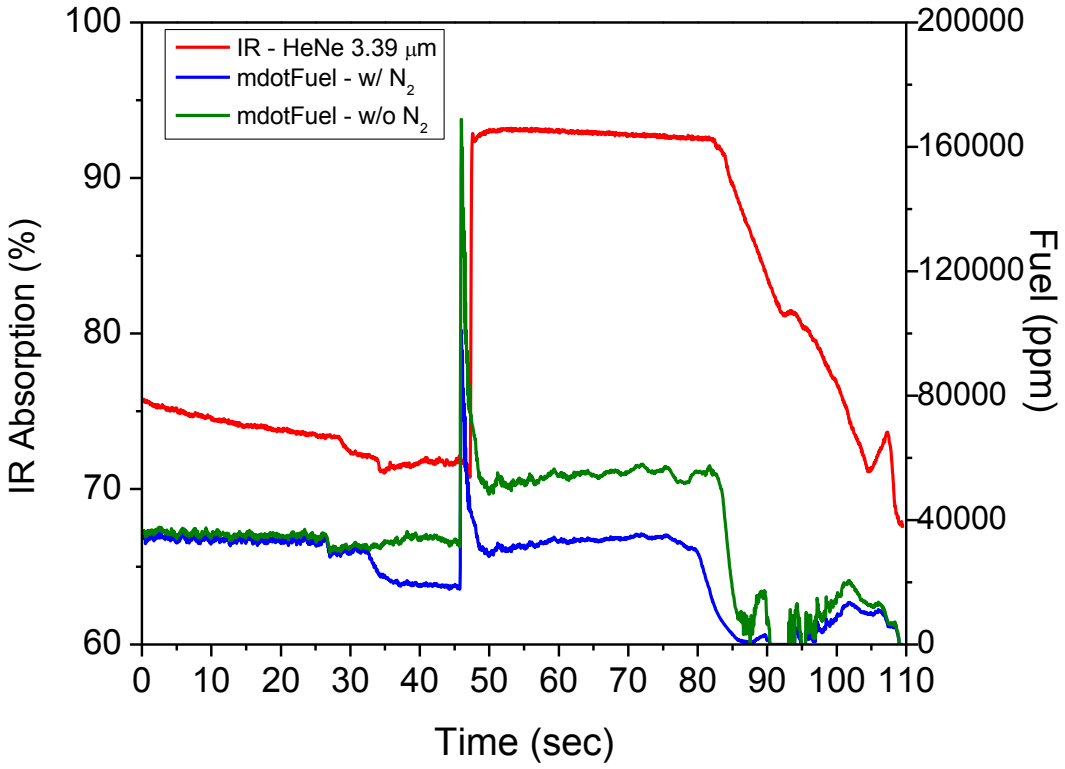

Figure 69 IR absorption trace due to UHC with calculated fuel concentrations for CF 1. The calculated concentrations are based on the fuel mass flow.

Figure 70 shows the calculated and measured fuel concentrations. Although the mid-IR diagnostics show good agreement between 50 and 80 s, there is about a 16000-ppm offset from 0 – 30 s. Additional cold-flow data are required to understand the fuel sensitivity of the mid-IR sensor and investigate the concentration offsets.

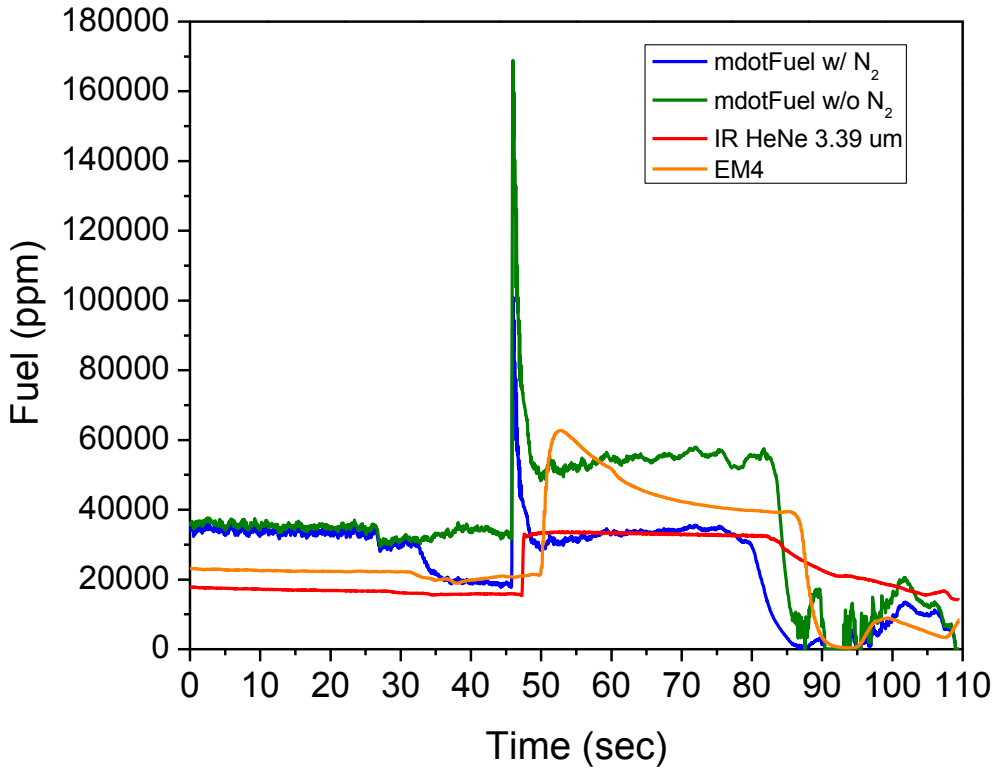

Figure 70 Fuel concentration measurements using the mid-IR sensor and UHC analyzer (EM4) for CF 1. The calculated fuel concentrations are also plotted for comparison.

Figure 71 presents mass-flow data for cold-flow 2 (CF-2) operating at different operating rig conditions where the oxygen mass flow is approximately zero. CF 2 was performed to analyze the flow ramp controls for the reactant constituents excluding O_2. Figure 72 and Figure 73 illustrate the mid-IR absorption and measured fuel

concentration, respectively. The signals from the mid-IR sensor are noisier due to operating at or near 100% absorption of the laser shown in Figure 72.

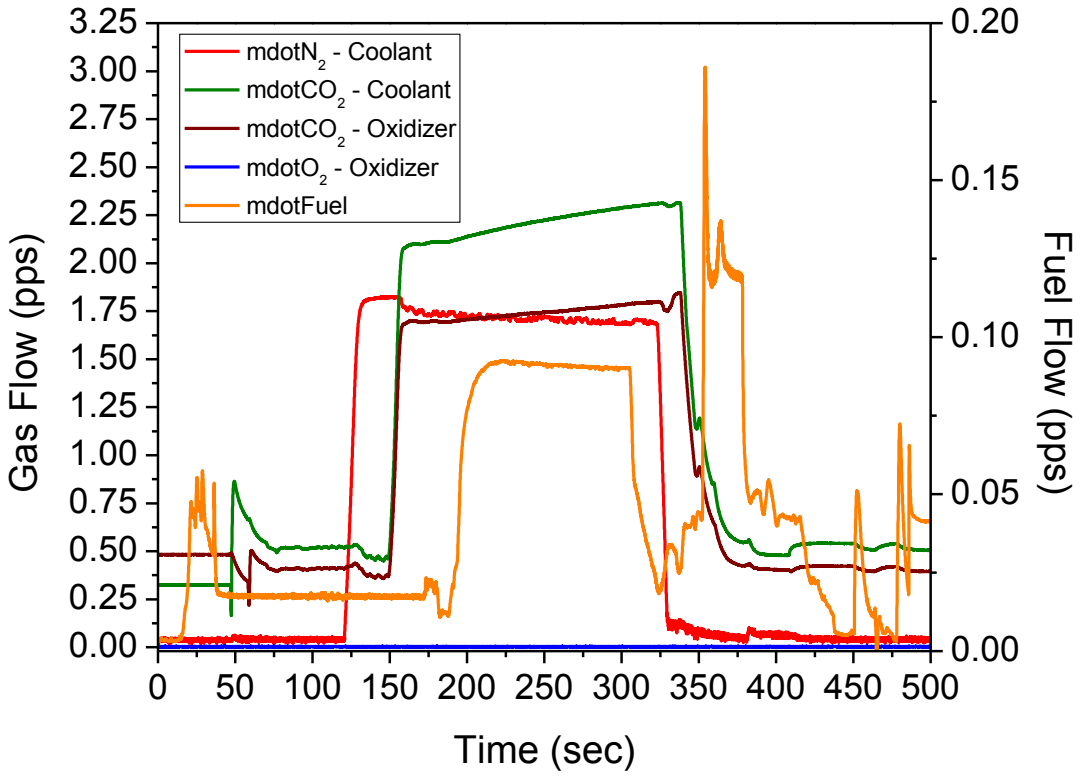

Figure 71 Combustor rig gas flows in pounds per second for Cold-Flow (CF) 2. This set of cold-flow data is used to gain better flow ramp control without flowing O_2 through the combustor rig.

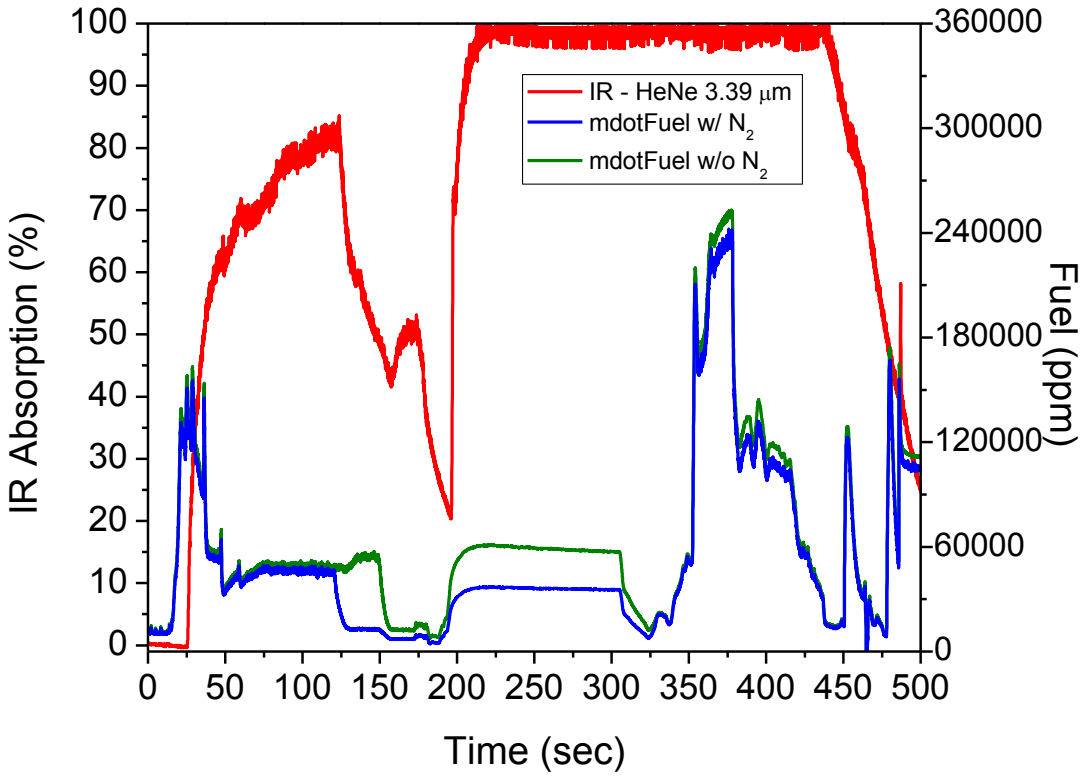

Figure 72 IR absorption trace due to UHC with calculated fuel concentrations for CF 2. The calculated concentrations are based on the fuel mass flow. The IR signal is noisier due to mid-IR sensor operating close to full laser attenuation (100% IR absorption).

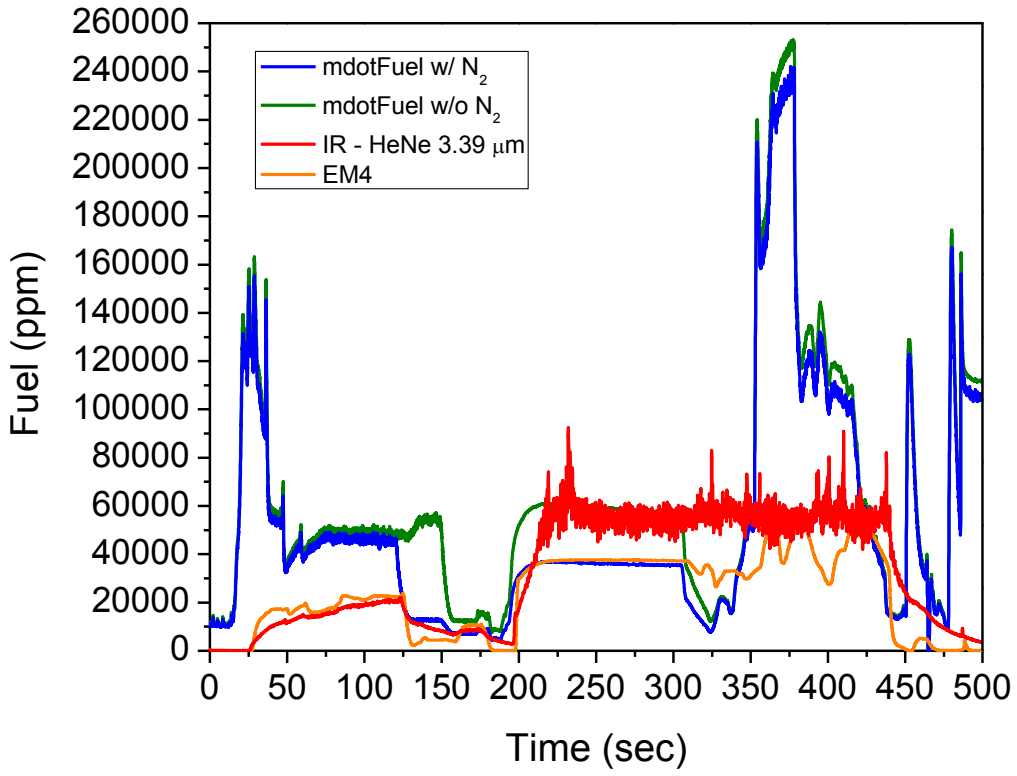

Figure 73 CF 2 fuel concentration measurements using calculated fuel from mass flow, UHC and mid-IR sensor. The fuel calculations from the fuel mass flow measure concentrations that fully attenuate the mid-IR laser from 0 – 150 s and 200 – 500 s.

Both calculated fuel concentrations from the fuel mass flow agree between 0 – 125 s due to the low N_2 mass flow shown in Figure 71. However, the UHC analyzer and the mid-IR sensor measure a large offset between 0 – 125 s. The UHC analyzer and mid-IR sensor both measure no fuel at the start of CF 2, while the fuel mass flow measures approximately 11000 ppm. The drop in calculated fuel with N_2 at around 125 s is due to the increase in N_2 flow shown in Figure 71. The second drop in fuel around 150 s is due

to the increase in CO_2 coolant and oxidizer flow which are more prominent in the fuel concentration without N_2. The mid-IR diagnostics in Figure 73 show good agreement with the calculated fuel concentration without N_2 between 200 – 300 s. It seems that the mid-IR sensor did not detect the reduction in fuel between 300 – 350 s. This result may be due to the laser being close to being fully attenuated, or perhaps the corresponding decrease in fuel concentration may be within the noise level. Figure 74 shows the mid-IR voltage signal from the transmitted detector and measures a slight drop in fuel from 300-350 s which means it may be within the noise level. EM4 also detected a slight drop in fuel concentration. This drop may indicate that the emissions equipment using the sample gas line may not be as sensitive to flow variations upstream of the rig. The fuel concentration limit of the mid-IR sensor agrees with the mid-IR absorbance and fuel concentration values tabulated in Table 3 using the absorption cell path length of 11.8 cm.

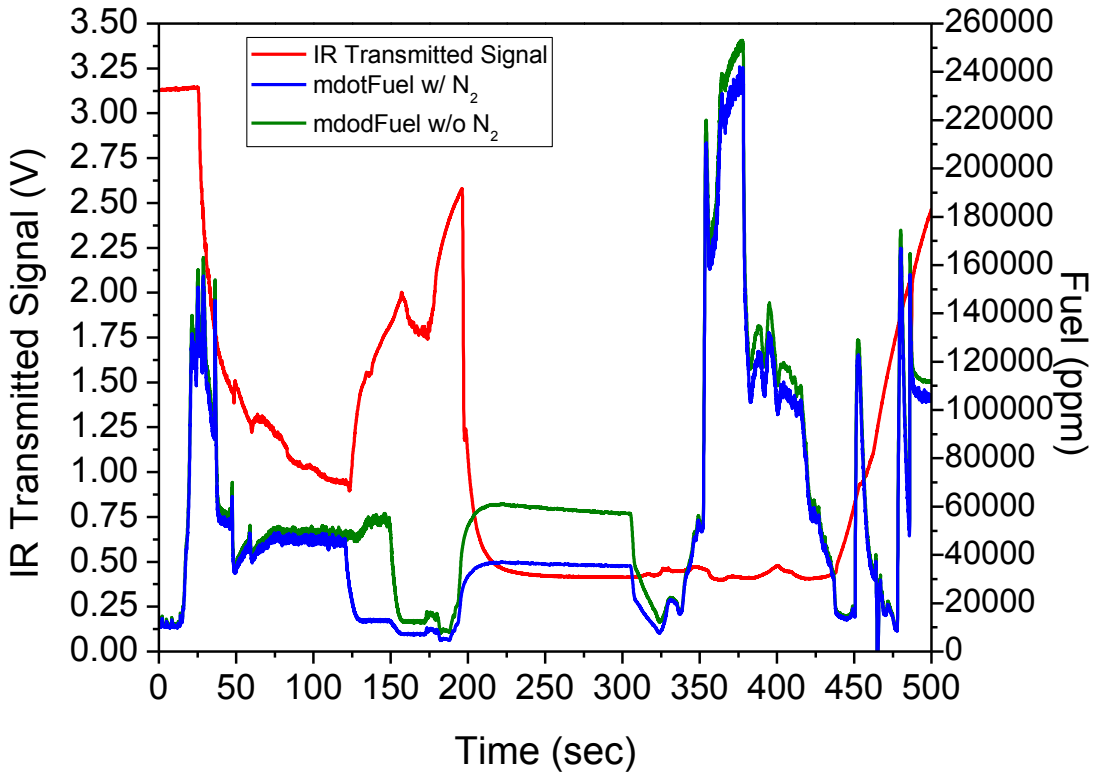

Figure 74 IR voltage signal from transmitted IR detector along with the fuel calculations based on the fuel mass flow. The IR detector shows signal response in fuel measurements that correspond to less than 100% IR absorption. The IR signal baseline is recorded as approximately 3.14 V.

Table 3 Variation of calculated fuel concentration with mid-IR absorption and absorbance using the absorption cell path length of 11.8 cm.

Absorption (%)	Absorbance	X_{fuel} (ppm)
0	0.00	0.00
2.5	0.03	318.35
20	0.22	2805.17
30	0.36	4485.60
50	0.69	8715.39
80	1.61	20236.50
99	4.61	57918.29
99.5	5.30	66622.56

The oxygen present as a constituent may have a broadening effect that will change the absorption coefficient. The absorption coefficient for these fuel concentration measurements was experimentally determined using a known CH_4/CO_2 mixture. This calibration gas was chosen due to the highly diluted fuel in CO_2. However, additional calibration experiments need to be performed using a mixture of CH_4 / CO_2 / O_2 to replicate the true composition during the cold-flows. Although data for CH_4 – N_2 broadening is given in A.4 of the Appendix, the broadening effect in using these different constituents needs to be investigated to fully understand the behavior of the absorption coefficient. Additional cold-flow tests need to be performed with varying O_2 within the oxidizer to validate these results. The fuel concentration limit of the mid-IR sensor may be increased by decreasing the absorption path length.

5.4 Preliminary discussion and analysis on fiber-coupled mid-IR sensor for CO

This section discusses the two fiber-coupled configurations of the mid-IR sensor for CO concentration measurements. The objective of using one of the two configurations is to directly couple the mid-IR sensor with the combustor rig to investigate the CO time-history within the combustor. As discussed in Chapter 3, configuration 1 couples the mid-IR fiber with the combustor by attaching the collimator housing directly onto the optical window port. Configuration 2 aligns the mid-IR laser at the exhaust exit by mounting the collimator housing close to the exhaust. Preliminary results and design challenges using both configurations are discussed in this section.

5.4.1 Fiber-coupled mid-IR diagnostics using configuration 1

Configuration 1 directly couples the mid-IR laser through the combustor exhaust liner via the optical window ports. The inner-diameter of the exhaust liner was measured as 3.25 in, as provided by PSI. This dimension is used as the absorption path length for the DAS simulations. An equilibrium analysis was performed using different reactant inlet temperatures as well as the oxygen percentage of the rig within the oxidizer. Figure 75 illustrates the variation of calculated CO equilibrium concentration with oxygen percentage. The equilibrium analysis was performed at 1 atm and 170.5 atm for the inlet temperatures of 300 K and 600 K using constant pressure and enthalpy.

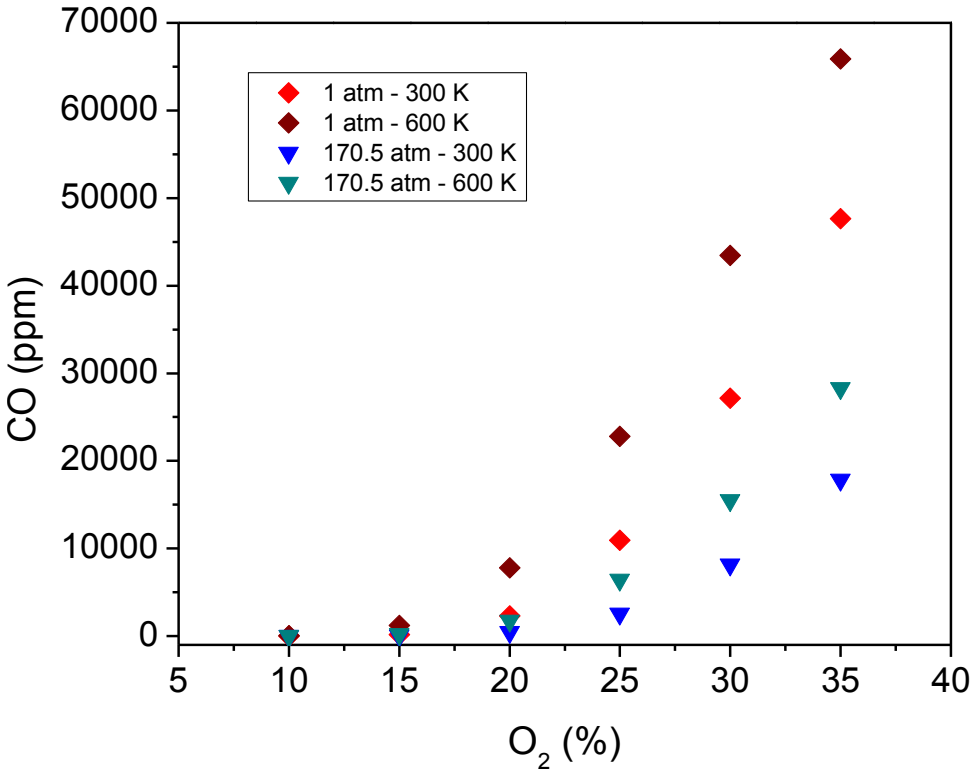

Figure 75 Variation of equilibrium CO concentration with reactant O_2 percentage. The concentrations are plotted for 1 atm and 170.5 atm at 300 K and 600 K.

Figure 75 shows the calculated CO concentration to be higher at 1 atm for both temperatures shown. At 20% O_2 and 300 K, the calculated CO concentration is shown to be approximately 2300 ppm and 450 ppm for 1 atm and 170.5 atm, respectively. Figure 76 and Figure 77 illustrate the simulated spectral variation of CO absorption with an inlet temperature of 300 K for 1 atm, 170.5 atm (2500 psi) and 341 atm (5000 psi). The line shapes become more broadened at higher pressure due to collisional (pressure) broadening, as discussed in Chapter 2. The absorption increases when changing the

oxygen percentage from 20% to 30% due to the increase in calculated CO concentration from the equilibrium analysis shown in Figure 75. The operating wavelength of the QC laser can be tuned (within the tunable range) to optimize the CO sensitivity and SNR of the mid-IR diagnostics to avoid saturation. An operating pressure limit needs to be determined for the mid-IR diagnostics to avoid full attenuation of the IR laser and maintain the SNR. The operating pressure limit of the fiber-coupled mid-IR sensor is dependent on the inlet temperature and the design oxygen percentage as shown in Figure 75. Additional CO spectral line shapes are provided in A.5 of the Appendix. The spectral absorption of CO_2 and H_2O is also provided to compare mid-IR absorption at high pressures.

The main sensor challenges faced with configuration 1 is the coupling of the mid-IR diagnostics directly with the combustor rig. The mid-IR fiber and collimator will be exposed to the rig vibrations during performance tests. The mid-IR laser coming out of the fiber collimator needs to be perfectly aligned through the 0.12 in.-diameter optical path and exhaust liner in order to "catch" it with the integrating sphere on the other side of the rig. Any misalignments due to rig vibrations will block the mid-IR laser and ruin the mid-IR diagnostics. The mid-IR fiber can also be easily damaged by vibrations since it is a CIR optical glass fiber. Therefore, configuration 1 has not been used during an actual combustor rig performance test.

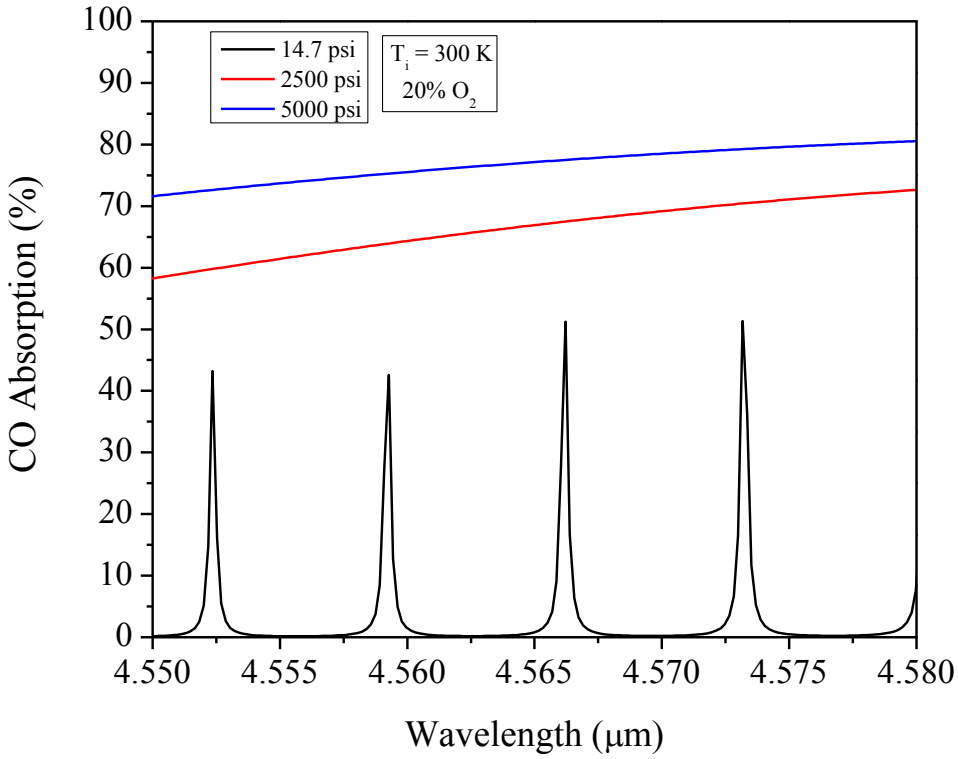

Figure 76 Spectral variation of CO absorption near the R(12) transition for 14.7 psi, 2500 psi and 5000 psi at an inlet temperature of 300 K. The equilibrium composition calculated at 20% O_2 is used.

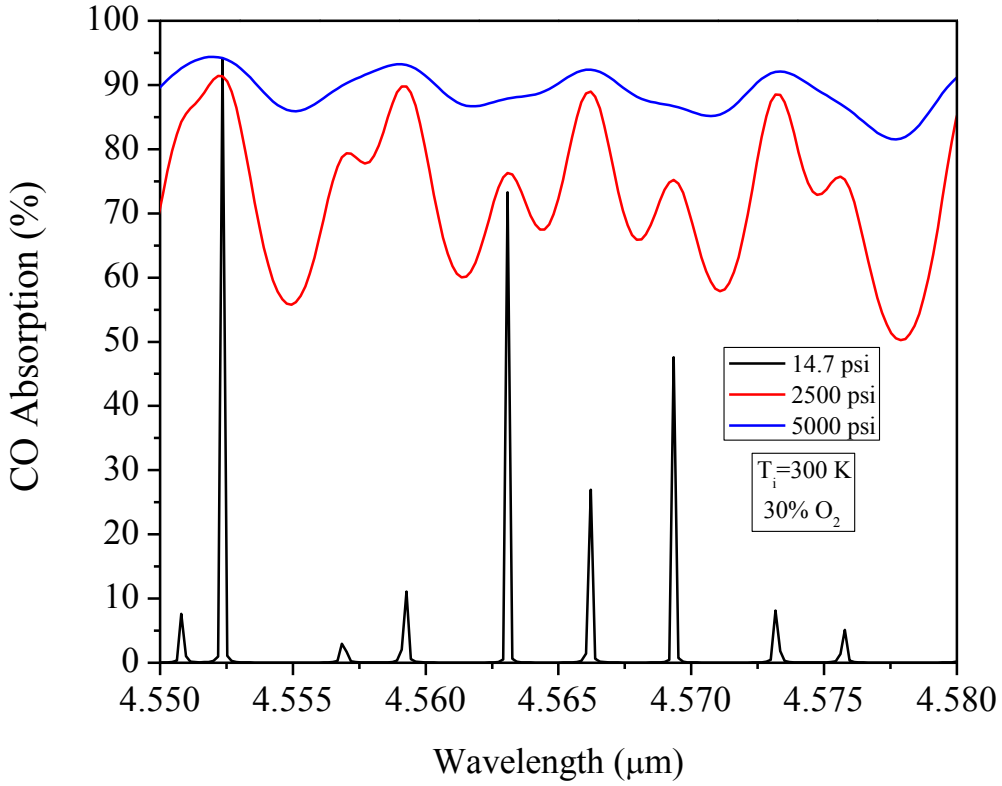

Figure 77 Spectral variation of CO absorption near the R(12) transition for 14.7 psi, 2500 psi and 5000 psi at an inlet temperature of 300 K. The equilibrium composition calculated at 30% O_2 is used.

5.4.2 Fiber-coupled mid-IR diagnostics using Configuration 2

Configuration 2 couples the mid-IR laser through the exhaust nozzle exit as discussed in Chapter 3. This configuration eliminates the difficulties in attaching the mid-IR fiber and collimator directly onto optical window port which exposes them to vibrations during performance tests. Instead, the mid-IR fiber and collimator are attached to a plate bolted onto a concrete block near the exhaust. This setup is intended to isolate

the equipment from the rig vibrations and eliminate misalignment issues from the optical window ports. However, the major design challenge faced with configuration 2 is measuring the true conditions and true path length at the exhaust. The choked flow conditions at the exhaust throat and the gas dynamics at the exhaust exit make it difficult to accurately measure or predict the static temperature and pressure over the path length of the laser propagation. These static conditions vary with radial and axial distance from the exhaust. An integrated method can be applied using the CFD analysis provided by PSI to determine the static conditions and true absorbance path length based on the location of the laser beam with respect to the exhaust nozzle exit.

5.4.3 General discussion for the fiber-coupled mid-IR diagnostics

The safety of the mid-IR equipment is also of concern in addition to the design challenges faced from both configurations. Using configuration 2 may reduce the vibrations that the mid-IR equipment experiences but it may not be enough to isolate the glass fiber from vibrating up to its breaking point. The high temperatures exiting the rig can also damage the transmitted detector on the "catch" side.

Once the safety of the mid-IR equipment has been secured, the battle for IR signal through the coupling system still makes it difficult to measure accurate concentration measurements. Based on the mid-IR optical fiber datasheet provided by the manufacturer, the fiber transmits approximately 35% of the IR signal between 2100 and 2200 cm^{-1}. The amount of IR signal transmitted through the fiber decreases with increasing fiber length. Only ≈3% of the IR signal coupled into the sphere is incident on

the detector due to the losses within the gold-coated integrating sphere. As shown in Figure 78, the IR signal generated from the exhaust thermal emission may dominate the IR QC laser signal. Figure 78 illustrates the IR signal output from the transmitted IR detector during a steady 9.5-bar (950 kPa) hot-fire test along with the rig temperature. A flame-out is shown to occur towards the end. The IR signal generated from the thermal emission peaked at approximately 0.78 V. The IR signal output from the laser using the integrating sphere is on the order of several hundred mV.

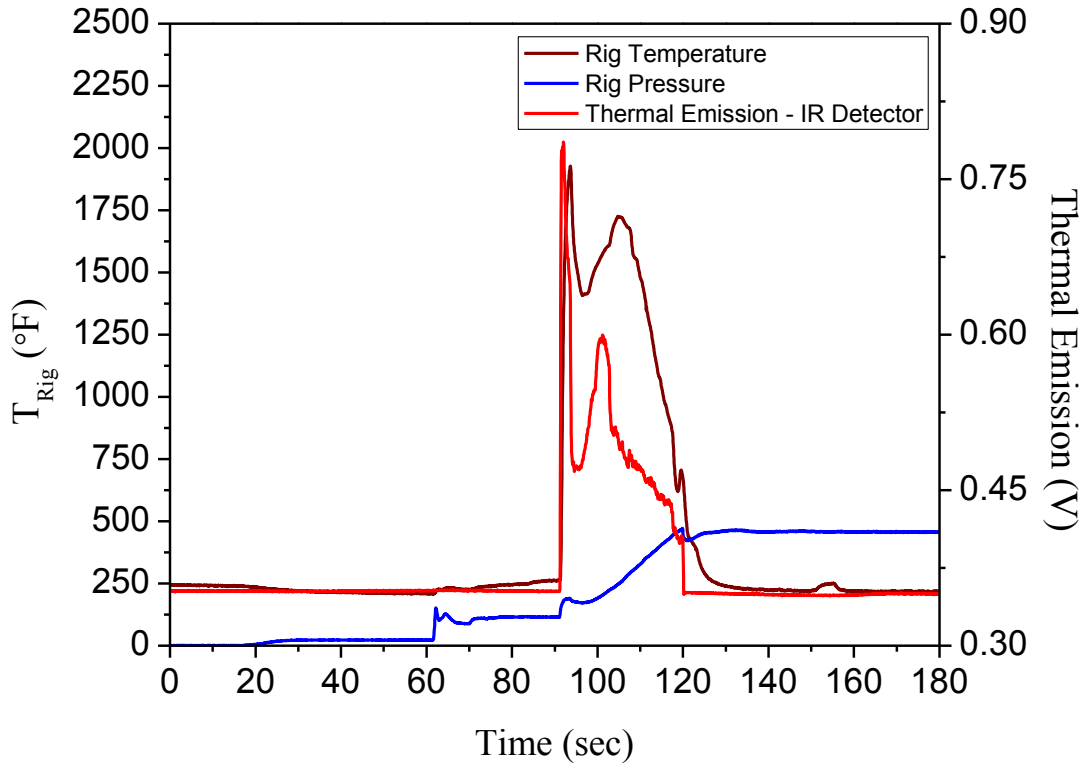

Figure 78 IR signal (V) generated from the exhaust thermal emission along with the rig temperature and rig pressure. This signal is captured through the integrating sphere and into the transmitted IR detector.

The fiber-coupled, mid-IR diagnostic was changed from DC- to AC-coupled measurement to reduce the IR signal from thermal emission. Operating in AC mode and implementing an optical chopper in front of the QC laser allows only the changing signal to be recorded. Therefore, operating in AC mode will eliminate the steady IR signal from thermal emission. Adjusting the frequency of the optical chopper also adjusts the frequency of the AC signal generated by the QC laser. A gain of 20 dB (10V) is implemented through the PA-9 preamplifiers for the IR detectors when operating in AC mode, resulting in an increase in IR signal from the QC laser. The laser output from the fiber is collimated up to 35 in. between the collimator and the inlet of the integrating sphere.

6. CONCLUSION

6.1 Summary

Accurate measurements of carbon monoxide (CO) concentrations are important in hydrocarbon-based combustion systems due to its direct relation to combustion inefficiency. Accurately measuring CO in hydrocarbon-based combustion systems can offer potential improvements in combustion design such as providing an indication if any local regions are operating fuel-lean or fuel-rich that may be a result of poor fuel/oxidizer mixing even when operating at the optimum equivalence ratio. Laser-based diagnostic techniques have been proven to be reliable in accurate species concentration measurements as well as other flow-field parameters such as pressure and temperature. They have been used extensively in combustion and propulsion applications to accurately measure time-sensitive species concentrations.

A mid-IR sensor for carbon monoxide (CO) concentration measurements has been developed using a DFB quantum-cascade (QC) laser operating near the fundamental band of CO at 4.566 μm. The objective of the mid-IR sensor was to demonstrate the CO detectability on a high-pressure combustor rig for steady and transient conditions. The mid-IR sensor was first validated using a shock-heated mixture containing a known amount of CO in a shock tube at Texas A&M University. Then the sensor was coupled to the high-pressure combustor rig to measure the CO concentration during performance tests. The mid-IR sensor proved to successfully capture the CO time-history during performance tests and also provided comparable concentration levels with calculated equilibrium concentrations based on the combustor rig stable conditions.

The mid-IR sensor was also adapted to measure unburned hydrocarbons (UHC) using a 3.39-μm HeNe laser. This sensor configuration proved to be responsive to fuel flow adjustments and provided comparable concentration levels to a flame-ionization detector (FID) that was also coupled to the combustor rig.

6.2 Recommendations

Recommendations for future work involve the improvement of the mid-IR diagnostics for CO and UHC concentration measurements. For both configurations, the spectral broadening behavior of the species at the selected wavelength needs to be better understood to accurately measure their concentrations. Although predicting the composition and all the constituents within the combustion gases may be impractical, understanding the broadening behavior from the major species and their impact factor on CO is crucial in accurately measuring CO, especially in steady rig conditions where a low mid-IR absorption trace is present. This recommendation is similar for the UHC concentration measurements where it is important to understand the broadening behavior based on the mixture composition in order to validate the constituents. This scenario directly applies to the CF 1 case where the N_2 presence within the sample line was unknown. The mid-IR sensor adapted for hydrocarbons was able to detect the fuel flow variations, but the concentration magnitudes showed various offsets compared to the calculated fuel concentration from mass flows.

Aside from improving the broadening data and calculation, the mid-IR diagnostics can be improved by a more accurate method in monitoring the baseline and

zero signals during the performance tests. Any baseline shifts or change in zero signals due to change in ambient conditions can cause an offset resulting in an incorrect concentration measurement. The mid-IR sensor fuel configuration seemed to have more issues with baseline shifts due to the nature in power drifts from the 3.39 μm HeNe laser. The QC laser proved to show minimal baseline shifts. However, its external cooling system may need to be improved to provide a more-stable laser operating condition while reducing the thermal load on the laser system. Operating on a more-stable condition can reduce the overall uncertainty in CO concentration measurements by minimizing the laser mode-jumps that cause a shift in operating wavelength.

The overall uncertainty of the CO concentration measurements can be reduced even further by operating in a completely dry or wet-based diagnostic to eliminate condensation problems. The condensation of water within the sample line may cause some of the mid-IR laser signal to be absorbed or scattered by the liquid H_2O droplets resulting in a false absorbance measurement. The H_2O within the combustion gases needs to be either in gaseous form or be removed for proper CO absorption sensing. This remedy will reduce the absorption coefficient deviation, resulting in a lower total uncertainty. It is recommended to use a desiccant to remove all of the water due to the complexity in adding heating lines on the entire sample line and absorption cell. However, adding a desiccant can cause a slower time-response as shown with the CAI analyzer. Nevertheless, a longer-time delay can be acceptable since this recommendation offers a more-accurate measurement on a dry basis. In addition to comparing the mid-IR CO concentration measurements with the equilibrium results discussed in this thesis, the

mid-IR diagnostics need to be compared to the combustor rig kinetic model to obtain a better representation of the combustion process.

Finally, the implementation of the fiber-coupled mid-IR sensor configuration should be continued and potentially tested during a hot-fire or a cold-flow test to validate its usability. This configuration potentially offers a true reading of what is really happening during combustion within the exhaust liner. The pressure and temperature limitations of the spectroscopy parameters obtained from the HITRAN database need to be investigated in order to validate the DAS simulations up to the operating combustor rig pressure of 300 bar. The accuracy of the CO mid-IR absorption measurements at elevated pressures can potentially be improved by implementing a wavelength-modulation-spectroscopy (WMS) technique where the operating laser wavelength is sinusoidally modulated at a selected frequency. This technique allows for species concentration measurements as well as pressure and temperature of the mixture by properly selecting the operating wavelengths during frequency modulation. Absorption measurements using a WMS technique offer optimal detection of broadened spectra at high pressures. The QC laser can be current and temperature-tuned to select the appropriate operating wavelengths to accurately distinguish the mid-IR absorption from CO, CO_2, and H_2O since the estimated interfering absorptions are significant at elevated pressures. The validation of the absorption simulations at elevated conditions as well as the coupling of the mid-IR diagnostics need to be addressed in order to overcome the design challenges faced with the fiber-coupled configurations.

REFERENCES

Anderson, J. D. 2006. *Hypersonics and High Temperature Gas Dynamics*, *2nd Ed.* McGraw-Hill, New York.

Aul, C. J., Metcalfe, W. K., Burke, S. M., Curran, H. J., and Petersen, E.L. 2013. Ignition and kinetic modeling of methane and ethane fuel blends with oxygen: A design of experiments approach. *Combustion and Flame*, **160**, 1153 – 1167.

Chao, X., Jeffries, J. B., and Hanson, R. K. 2009. Absorption sensor for CO in combustion gases using 2.3 μm tunable diode lasers. *Meas. Sci. Technol.*, **20**, 115 - 201.

Demtröder, W. 1996. *Laser Spectroscopy: Basic Concepts and Instrumentation, 2nd Ed.,* Springer-Verlag, New York, NY.

Edwards, B. N., and Burch, D. E. 1965. Absorption of 3.39-micron helium-neon laser emission by methane in the atmosphere. *Journal of the Optical Society of America*, **55**, 174 – 177.

Hartmann, J. M., Rosenmann, L., Perrin, M. Y., and Taine, J. 1988. Accurate calculated tabulations of CO line broadening by H_2O, N_2, O_2, and CO_2 in the 200 – 3000 K temperature range. *Applied Optics*, **27**, 3063 – 3065.

Hollas, J. M. 2005. *Modern Spectroscopy, 4th Ed.,* J. Wiley, Chichester, New York.

Jimenez, R. B., Caton, J. A., Anderson, T. N., Lucht, R. P., Walther, T., Roy, S., Brown, J. R., and Gord, J. R. 2006. Application of a difference-frequency-mixing based iode-laser for carbon monoxide detection in the 4.4 – 4.8 μm spectral region. *Applied Physics B,* **85**, 185 – 197.

Klingbeil, A. E., Jeffries, J. B., and Hanson, R. K. 2006. Temperature- and pressure-dependent absorption cross sections of gaseous hydrocarbons at 3.39 μm. *Meas. Sci. Technol.*, **17**, 1950 – 1957.

Klingbeil, A. E., Jeffries, J. B., and Hanson, R. K. 2007. Design of a fiber-coupled mid-infrared fuel sensor for pulse detonation engines. *AIAA Journal*, **45**, 772 – 778.

Law, C. K. 2006. *Combustion Physics,* Cambridge University Press, New York.

Lefebvre, A., H., Ballal, D. R. 2010. *Gas Turbine Combustion: Alternative Fuels and Emissions, 3rd Ed.,* Taylor Francis Group, Boca Raton, FL.

Lin, X., Yu, X. L., Li, F., Zhang, S. H., Xin J. G., and Chang, X. Y. 2013. CO concentration and temperature measurements in a shock tube for Martian mixtures by coupling OES and TDLAS. *Applied Physics B,* **110**, 401 - 409.

McMahon, J., Troup, G. J., Hubbert, G., and Kyle, T. G. 1972. The effect of pressure and temperature on the half-width of the methane absorption at 3.39μ. *Journal of Quantitative Spectroscopy & Radiative Transfer*, **12**, 797 – 805.

Mével, R. Boettcher, P.A., and Shepherd, J. E. 2012. Absorption cross section at 3.39 μm of alkanes, aromatics and substituted hydrocarbons. *Chemical Physics Letters,* **531**, 22 – 27.

Mihalcea, R.M., Baer, D. S., and Hanson, R. K. 1998. A diode-laser absorption sensory system for combustion emissions meaurements. *Meas. Sci. Technol.*, **9**, 327 – 338.

Porter, J. M., Jeffries, J. B., Hanson, R. K. 2009. Mid-infrared absorption measurements of liquid hydrocarbon fuels near 3.4 μm. *Journal of Quantitative Spectroscopy & Radiative Transfer*, **110**, 2135 – 2147.

Ren, W., Farooq, A., Davidson, D. F., and Hanson, R. K. 2012. CO concentration and temperature sensor for combustion gases using quantum-cascade laser absortion near 4.7 μm. *Applied Physics B*, **107**, 849 – 860.

Rotavera, B., Scheu, K., Polley, N., Crofton, M., Petersen, E. L., and Bourque, G. 2010. Ignition and combustion of heavy hydrocarbons using an aerosol shock-tube approach. *Proceedings of ASME Turbo Expo 2010: Power for Land Sea and Air*, **GT2010-22844**.

Rothman, L. S., Jacquemart, D., Barbe, A., Benner, D. C., Birk, M. et al. 2005. The HITRAN 2004 molecular spectroscopic database. *Journal of Quantitative Spectroscopy and Radiative Transfer*, **96**, 139 – 204.

Saravanamutto, H. I., Cohen, H., Rogers, G. 2001. *Gas Turbine Theory*, 6^{th} *Ed.,* Prentice Hall, Harlow, England.

Smith, G. P., Golden, D. M., Frenklach, M., Moriarty, N. W., Eiteneer, B., Goldenberg, M., Bowman, C. T., Hanson, R. K., Song, S., Gardiner, Jr., W. C., Lissianski, V. V., and Qin, Z. *GRI-Mech 3.0,* 1999, http://www.me.berkeley.edu/gri_mech/, Nov. 2013.

APPENDIX

A.1 DFB QC-laser single mode emission frequencies

Figure A. 1 illustrates a compilation of the QC laser datasheet provided by Alpes Lasers. The operating wavelength can be tuned by adjusting the current supplied to the QC laser and temperature at which it operates. As shown, there is a large jump between 370 and 390 mA. Operating near this jump will make the QC laser more susceptible to mode-jumping. Therefore, the QC laser operates in a more stable condition furthest from this mode-jump. This ideal condition corresponds to 400 mA and -20 ˚C which is closest to the R(12) transition (2190.02 cm^{-1}). The laser conditions used for the wavelength calibration procedure and performance tests are between 360 – 370 mA and -10 to -15 ˚C in order to reduce the thermal load on the thermoelectric cooler and PT-100 RTD sensor located within the QC laser package. Reducing the thermal load on these components will enhance the life of the QC laser. The external cooling system of the QC laser can be improved in order to reduce the thermal load while operating at a more stable condition.

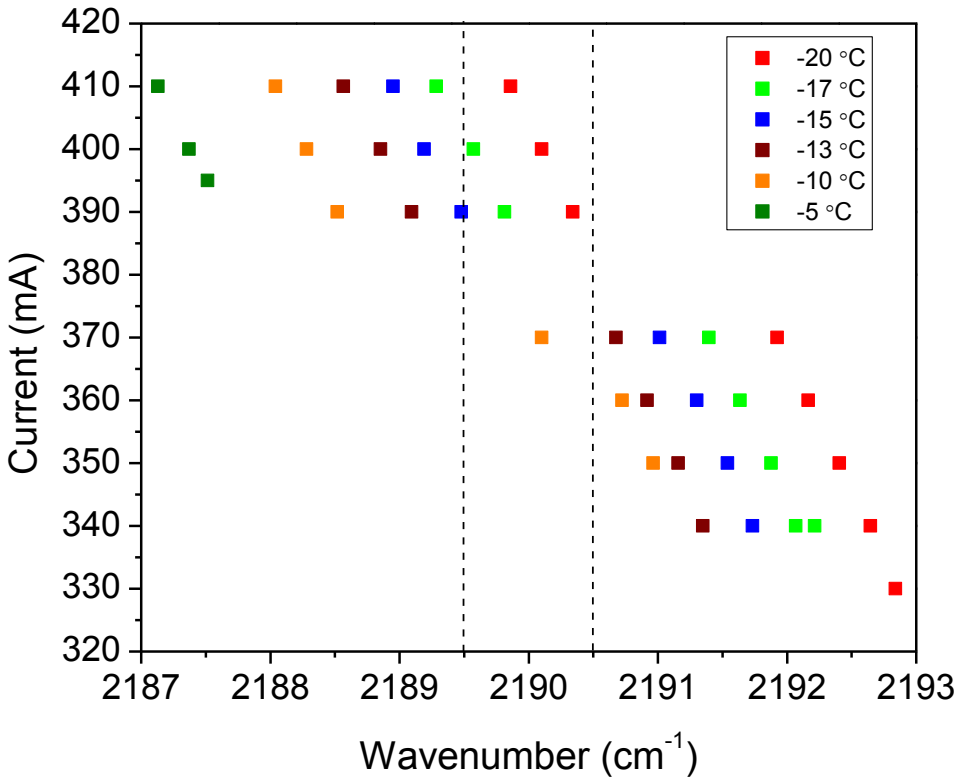

Figure A. 1 Applied DC current as a function of single mode emission frequencies and temperatures. Data were compiled from the datasheet provided by Alpes Lasers.

A.2 Mid-IR sensor validation analysis using a shock-heated mixture

Table A. 1 summarizes the CO line-strength and Ar-broadening parameters along with their uncertainty for the selected transition in this study. Ren et al. (2012) measured the Ar-broadening coefficient, $2\gamma_{CO\text{-}Ar}$, and extrapolated it to fit the temperature range of 1100-2000 K along with the temperature index, n. Ren et al. also reported the measured CO-line-strengh and Ar-broadening parameters for neighboring transitions in the R branch as well as the P branch using a DFB QC laser in a shock tube. Their measured

and calculated line-strengths were investigated as a function of temperatures up to their corresponding temperature fit 1100 – 2000 K.

Table A. 1 Measured CO line-strength and Ar-broadening parameters for the R(12) transition experimentally determined by Ren et al. (2012).

Transition (v'', J'')	S (296 K) (cm^{-2} atm^{-1})	$2\gamma_{CO\text{-}Ar}$ (296 K) (cm^{-1} atm^{-1})	$2\gamma_{CO\text{-}Ar}$ (296 K) Fit to 1100-2000 K	n Fit to 1100-2000 K
0, R(12)	7.16 (2.3%)	0.088 (3.0%)	0.079 ±0.007	0.581 ±0.012

A.3 Mid-IR diagnostics for on-site CO concentration measurements during rig performance tests

A.3.1 Absorption cell path-length optimization for CO absorption

Figure A. 2 illustrates the calculated IR absorption from CO with respect to path length and temperature. The absorption was calculated at various temperatures within the absorption cell to select an optimal path length for the combustor rig hot-fire tests. The absorption at 300 K has the highest IR absorption from CO from the three path lengths chosen. As discussed in 3.5 and presented in 5.2, the absorption cell contained a path length of 11.8 cm due to the availability of the sapphire optical windows originally used for the fiber-coupled configurations. According to Figure A. 2, this would fully attenuate the IR laser since the absorption cell temperature was measured to be around room temperature. However, Figure A. 2 shows the absorption calculation based on a high CO concentration of 20,800 ppm. The CO concentration levels presented in 5.2

shows a considerably lower level than shown below. The path length and temperature of the absorption cell would need to be adjusted for a predicted CO concentration of 20,800 ppm to avoid 100% IR laser absorption.

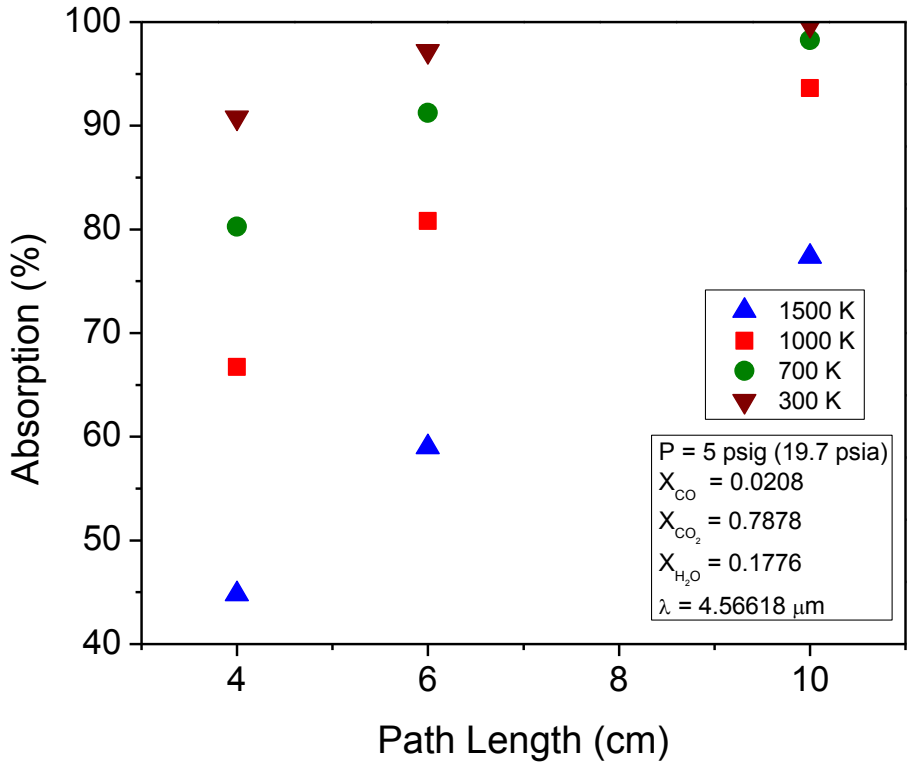

Figure A. 2 Calculated IR absorption from CO with respect to path length for various temperatures.

A.3.2 Tabulated CO line broadening by H_2O, N_2, O_2, CO_2

Table A. 2 tabulates the CO line-broadening parameters for the R(12) transition line calculated by Hartmann et al. (1988) at room temperature. These values were

calculated using a model that has been tested on the broadening of CO[1,4,7], CO_2[3,8,11], and H_2O lines. These values were used in Eq. 42 to calculate the CO line-broadening at the corresponding rig temperature presented in 5.2.

Table A. 2 CO line-broadening parameters at 300 K for the R(12) transition line ($m = 13 = J'' - 1$) for 220 – 3000 K. calculated by Hartmann et al (1988).

Collisional Partner	γ (300 K) (10^{-3} cm^{-1} atm^{-1})	n
CO-CO_2	65.6	0.54
CO-H_2O	127	0.78
CO-N_2	61.4	0.66
CO-O_2	50.1	0.60

A.3.3 Mid-IR signal temperature sensitivity

Figure A. 3 shows the IR detector signals without the incident IR laser (zero signals) from the QC laser. In DC operating mode, the IR detectors have a zero signal mainly due to the mid-IR emissions from the surroundings. These signals were minimized as much as possible by covering the mid-IR diagnostics. As discussed in Ch. 3, the mid-IR sensor was located in the emissions shed along with the additional gas analyzers. Both analyzers dissipated heat especially the UHC analyzer since it used a H_2-O_2 flame within the housing. All of these IR sources along with the ambience contributed to the zero signals that resulted in an offset during the absorption diagnostics. The zero signals increased with increasing ambient temperature. Although a

zero IR signal correlation with temperature can be created, it is difficult to characterize the measured temperature within the absorption cell as a function of all of the heat sources near the mid-IR diagnostics. Therefore, the zero IR signals were monitored and recorded along with the baseline signals before and after every performance tests to properly calculate the CO and fuel concentration measurements.

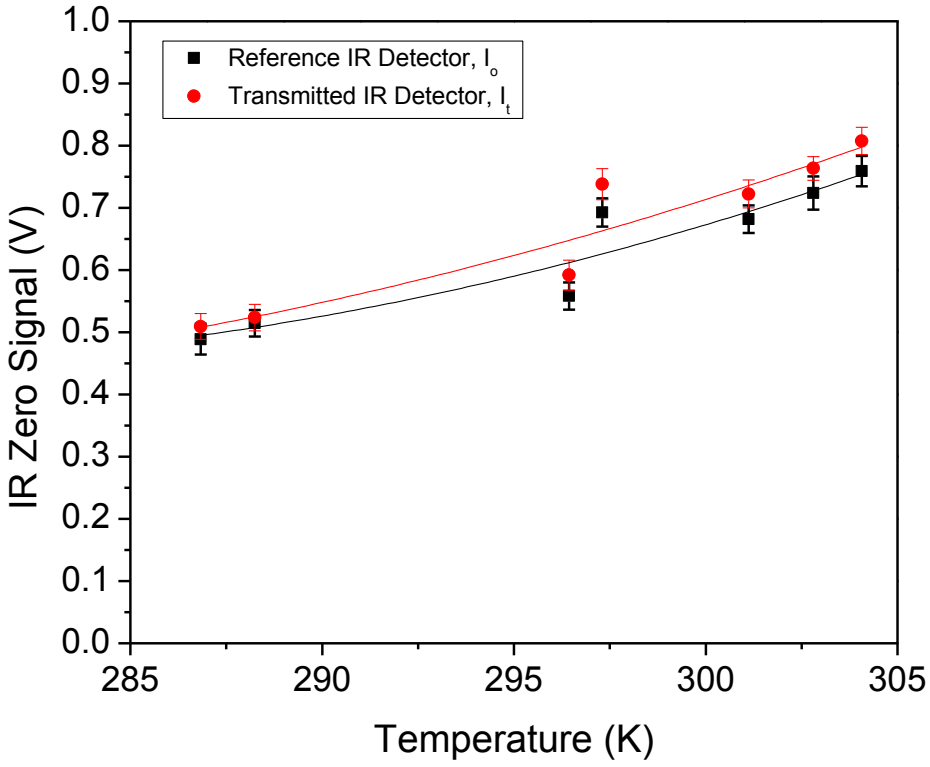

Figure A. 3 Zero signal from both IR InSb detectors with respect to ambient temperature. The average zero signals increase with temperature.

A.3.4 Dry and wet equilibrium analysis at constant enthalpy and pressure for CO concentration measurements

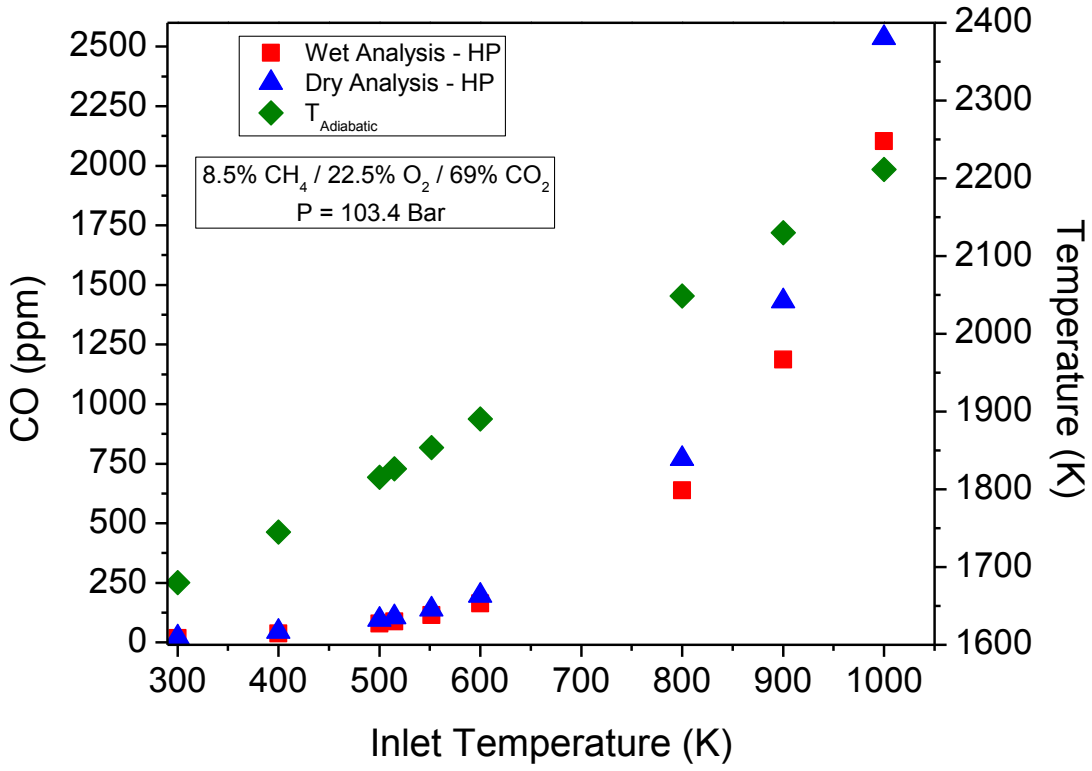

Figure A. 4 Wet and dry CO equilibrium analysis and adiabatic temperature with varying inlet temperature at 103.4 bar.

Table A. 3 Wet-based equilibrium product composition for major species as a function of inlet reactant temperature. The equilibrium analysis was performed at constant enthalpy and constant pressure of 103.4 bar.

Constraint	T_i (K)	$T_{Adiabatic}$ (K)	X_{CO2}	X_{H2O}	X_{O2}	X_{CO}
HP	500	1815.6	774610	169904	55174.3	78.7
HP	515	1826.5	774594	169895	55174.7	88.0
HP	552	1853.6	774548	169869	55176.7	114.9
HP	600	1890.3	774468	169828	55182.8	163.2

Table A. 4 Dry-based equilibrium product composition for major species as a function of inlet reactant temperature. The equilibrium analysis was performed at constant enthalpy and constant pressure of 103.4 bar.

Constraint	T_i (K)	$T_{Adiabatic}$ (K)	X_{CO2}	X_{H2O}	X_{O2}	X_{CO}
HP	500	1815.6	933419.1	0	66486.0	94.9
HP	515	1826.5	933407	0	66487.0	106.0
HP	552	1853.6	933370.7	0	66490.8	138.5
HP	600	1890.3	933303.1	0	66500.2	196.7

A.3.5 CO absorption coefficient uncertainty analysis for on-site calibration

The uncertainty of the measured absorption coefficient for the on-site mid-IR sensor was calculated using the Kine-McClintock method. This method allowed for the total uncertainty calculation based on the individuals uncertainties from each parameter. Equations A.1 and A.2 were taken from Eq. 50 to calculate the absorption coefficient as a function of the measured absorbance. Equations A.3 and A.4 show the total uncertainty and the partials taken with respect to each parameter.

$$\alpha_v = -\ln\left(\frac{I_t}{I_o}\right) = S(T)\phi_v X_i PL = k_v X_i PL \tag{A. 1}$$

$$k_v = \frac{\alpha_v}{X_i PL} \tag{A. 2}$$

$$U_{k_v} = \left[\left(\frac{\partial k_v}{\partial \alpha_v}\cdot u_{\alpha_v}\right)^2 + \left(\frac{\partial k_v}{\partial X_i}\cdot u_{X_i}\right)^2 + \left(\frac{\partial k_v}{\partial P}\cdot u_P\right)^2 + \left(\frac{\partial k_v}{\partial L}\cdot u_L\right)^2\right]^{1/2} \tag{A. 3}$$

$$\begin{aligned}
\frac{\partial k_v}{\partial \alpha_v} &= 1 \\
\frac{\partial k_v}{\partial X_i} &= -\frac{\alpha_v}{PLX_i^2} \\
\frac{\partial k_v}{\partial P} &= -\frac{\alpha_v}{X_i LP^2} \\
\frac{\partial k_v}{\partial L} &= -\frac{\alpha_v}{X_i PL^2}
\end{aligned} \tag{A. 4}$$

A.3.6 CO concentration uncertainty analysis for combustor rig performance tests

Equations A.5 and A.6 were taken from the Beer-Lambert law to calculate the mole fraction of species *i*. Equations A.7 and A.8 show the uncertainty of the mole fraction using the Kline-McClintock method along with the partials with respect to each parameter. Equations A.9 ant A. 10 show how the mid-IR signals were processed and how the uncertainty from both channels (incident and transmitted IR signals) was calculated. This method allowed for the signal correction from the zero signals and baseline fluctuations.

$$\left(\frac{I_t}{I_o}\right)_v = \exp\left(-k_v X_i PL\right) \tag{A. 5}$$

$$X_i = -\frac{1}{k_v PL}\ln\left(\frac{I_t}{I_o}\right) = -\frac{1}{k_v PL}\ln\left(\frac{(I_t - I_o) + I_o}{I_o}\right) = -\frac{1}{k_v PL}\ln\left(\frac{\Delta I + I_o}{I_o}\right) \tag{A. 6}$$

$$U_{X_i} = \left[\left(\frac{\partial X_i}{\partial k_v}\cdot u_{k_v}\right)^2 + \left(\frac{\partial X_i}{\partial \Delta I}\cdot u_{\Delta I}\right)^2 + \left(\frac{\partial X_i}{\partial I_o}\cdot u_{I_o}\right)^2 + \left(\frac{\partial X_i}{\partial P}\cdot u_P\right)^2 + \left(\frac{\partial X_i}{\partial L}\cdot u_L\right)^2\right]^{1/2} \tag{A. 7}$$

$$\begin{aligned}
\frac{\partial X_i}{\partial k_v} &= \frac{1}{PLk_v^2}\ln\left(\frac{\Delta I + I_o}{I_0}\right)\\
\frac{\partial X_i}{\partial \Delta I} &= \left(-\frac{1}{k_v PL}\right)\left(\frac{1}{\Delta I + I_o}\right)\\
\frac{\partial X_i}{\partial I_o} &= \left(\frac{1}{k_v PL}\right)\left(\frac{\Delta I}{\Delta I\cdot I_o + I_o^2}\right)\\
\frac{\partial X_i}{\partial P} &= \frac{1}{k_v LP^2}\ln\left(\frac{\Delta I + I_o}{I_o}\right)\\
\frac{\partial X_i}{\partial L} &= \frac{1}{k_v PL^2}\ln\left(\frac{\Delta I + I_o}{I_o}\right)
\end{aligned} \tag{A. 8}$$

$$\begin{aligned}
\Delta I &= I_t - I_0\\
I_t &= I_{t,raw} - I_{t,zero}\\
I_o &= I_{o,raw} - I_{o,zero}
\end{aligned} \tag{A. 9}$$

$$u_{\Delta I} = \left[\left(\frac{\partial \Delta I}{\partial I_t} \cdot u_{I_t} \right)^2 + \left(\frac{\partial \Delta I}{\partial I_o} \cdot u_{I_o} \right)^2 \right]^{1/2} = \left[u_{I_t}^2 + u_{I_o}^2 \right]^{1/2}$$

$$u_{I_t} = \left[\left(\frac{\partial I_t}{\partial I_{t,raw}} \cdot u_{t,raw} \right)^2 + \left(\frac{\partial I_t}{\partial I_{t,zero}} \cdot u_{I_{t,zero}} \right)^2 \right]^{1/2} = \left[u_{I_{t,raw}}^2 + u_{I_{t,zero}}^2 \right]^{1/2} \quad \text{(A. 10)}$$

$$u_{I_o} = \left[\left(\frac{\partial I_o}{\partial I_{o,raw}} \cdot u_{o,raw} \right)^2 + \left(\frac{\partial I_o}{\partial I_{o,zero}} \cdot u_{o,zero} \right)^2 \right]^{1/2} = \left[u_{I_{o,raw}}^2 + u_{I_{o,zero}}^2 \right]^{1/2}$$

A.4 Mid-IR sensor calibration for UHC using He-Ne laser at 3.39 µm

The mid-IR sensor adapted to fuel concentration measurements using the 3.39 µm HeNe Laser was calibrated using a CH_4/CO_2 mixture discussed in 3.6. This was done to experimentally determine the CH_4 absorption coefficient with CO_2 to replicate the cold-flow test conditions. However, the absorption coefficient was converted to the absorption cross-section, σ_v, to compare the CH_4-N_2 broadening determined from Klingbeil et al. (2006). This was done in order to see how the broadening differed between the collisional partners N_2 and CO_2 on CH_4. Equations A.11 through A.14 show the conversion from the absorption coefficient, k_v, to the absorption cross-section, σ_v, as a function of the molar concentration of species *i* [mole cm^{-3}].

$$\left(\frac{I_t}{I_o} \right)_v = \exp\left[-k_v X_i P L \right] \quad \text{(A. 11)}$$

$$k_v \left[cm^{-1} atm^{-1} \right] = \frac{-\ln\left(I_t / I_o \right)}{X_i P L} \quad \text{(A. 12)}$$

$$\left(\frac{I_t}{I_o}\right)_v = \exp\left[-k_v L\right] = \exp\left[-\sigma_v NL\right] \quad \text{(A. 13)}$$

$$k_v\,[cm^{-1}] = \frac{k_v[cm^{-1}atm^{-1}]}{X_i P} = \sigma_v N_i \quad \text{(A. 14)}$$

Table A. 5 tabulates the comparison of measured absorption cross sections for CH_4-N_2 at 298 K from different groups. The references for each reported value and technique may be found from Klingbeil et al. (2006). Figure A. 5 illustrates the experimentally-determined absorption cross section for CH_4-CO_2 at various pressures within the absorption cell used for CO and fuel concentration measurements. The plot shows a compilation of data at different pressures with varying ambient temperatures. The results showed that the absorption cross section was higher at lower ambient temperatures for a given pressure. The scatter shown in Figure A. 5 seems to fall within the difference in absorption cross-sections for CH_4-N_2 at 760 torr reported by different groups.

Table A. 5 Comparison of measured absorption cross-sections for CH_4-N_2 at 298 K. Compiled by Klingbeil et al. (2006).

Total Pressure (Torr)	σ_v (298 K) (m^2 $mole^{-1}$)	Uncertainty	Technique
760	21.1	3%	HeNe
760	25.3	-	HeNe
760	21.9	2%	HeNe
760	22.5	5%	HeNe
760	21.4	-	Calculation
30.4	36.7	-	HeNe
760	19.5	3%	FTIR

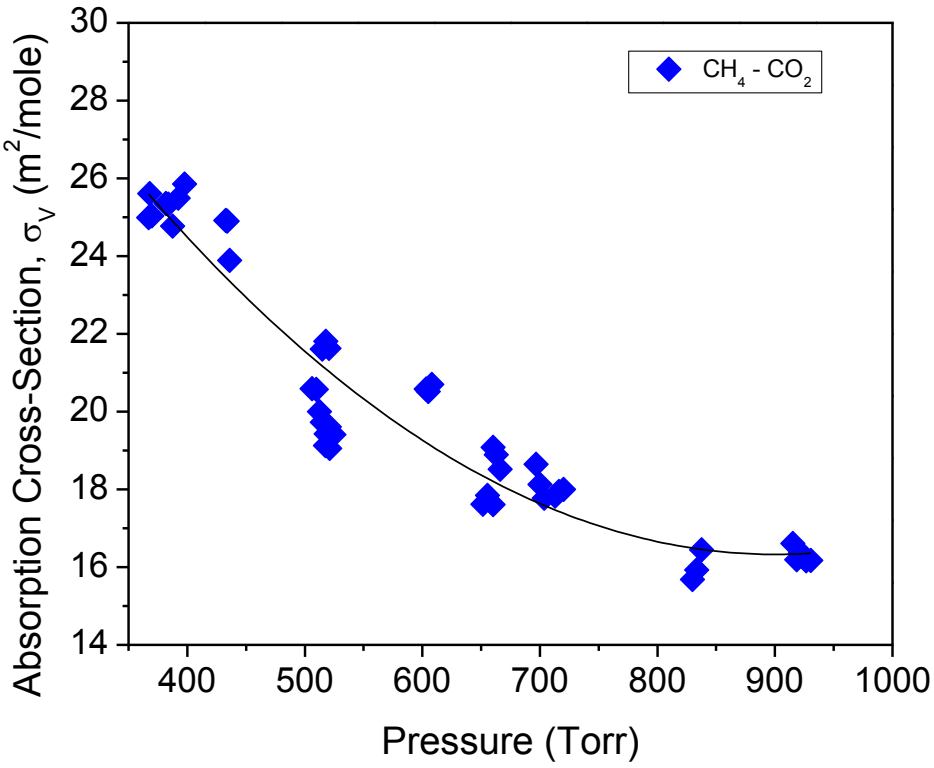

Figure A. 5 Experimentally determined absorption cross section for CH_4-CO_2 using the absorption cell with a path length of 11.8 cm. The data are a compilation of absorbance measurements at various ambient temperatures (not shown).

A.5 Fiber-coupled mid-IR diagnostics

Figures A.5 through A.10 illustrate the calculated IR spectral absorption near the R(12) transition a 4.566 μm (2190.02 cm^{-1}) for CO, CO_2, and H_2O at different pressures. The calculated mole fractions for each species were performed using the equilibrium constraint of constant pressure and enthalpy at an initial reactant temperature of 900 K. These calculations used a path length of 3.25 in representing the combustor exhaust liner inner-diameter for the fiber-coupled mid-IR sensor configuration 1.

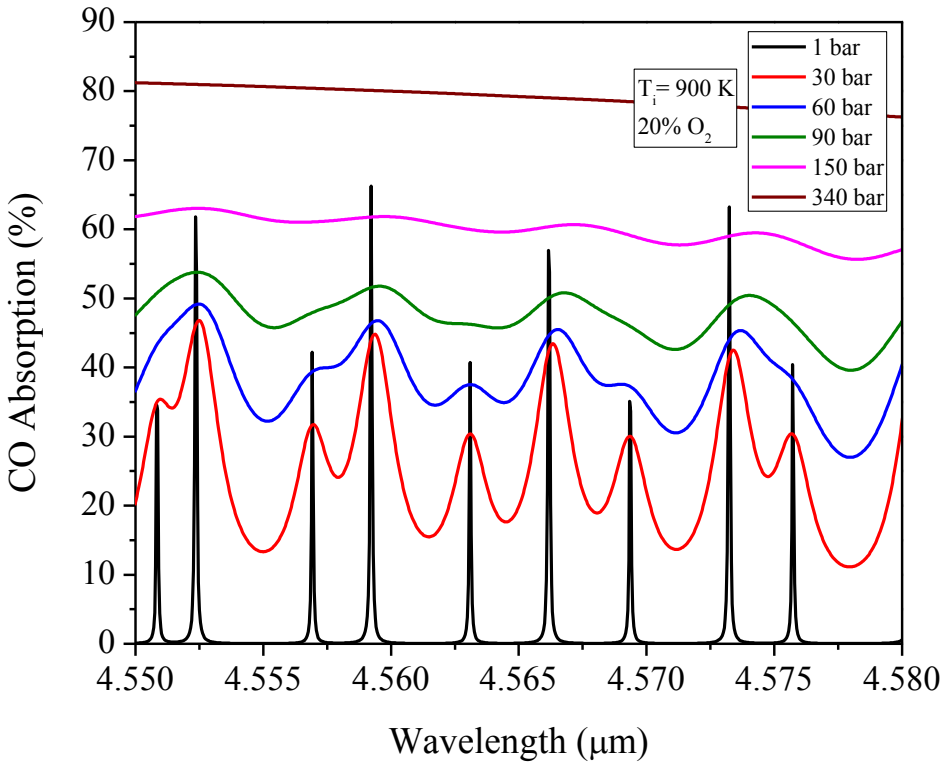

Figure A. 6 IR absorption from CO at different rig pressures. Equilibrium composition was based on 20% O_2 in reactants.

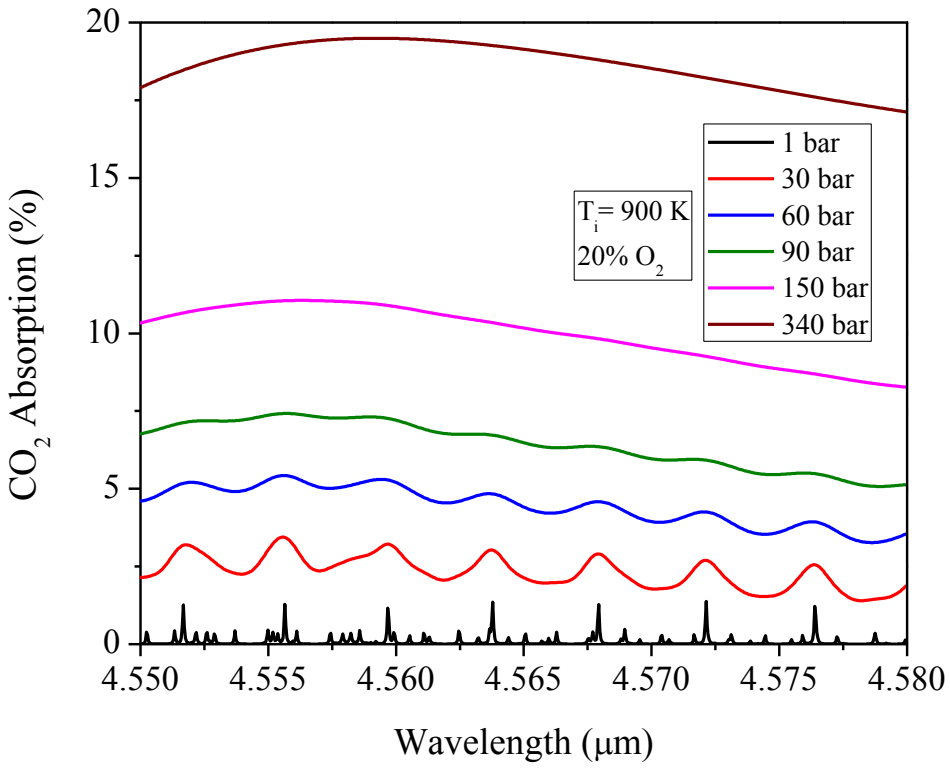

Figure A. 7 IR absorption from CO_2 at different rig pressures. Equilibrium composition was based on 20% O_2 in reactants.

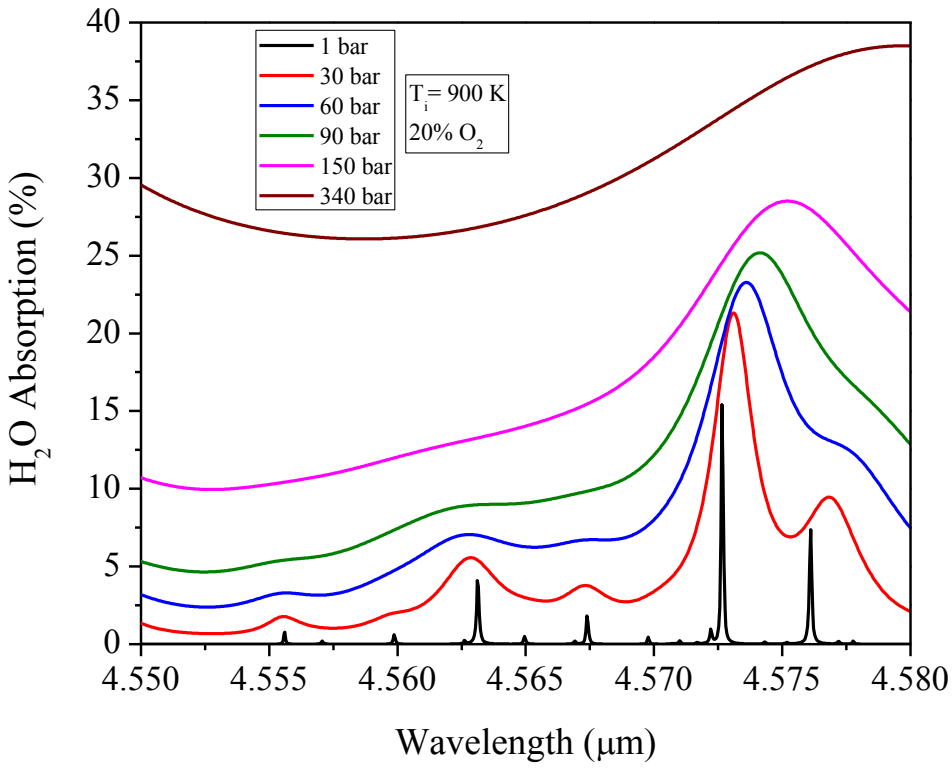

Figure A. 8 IR absorption from H_2O at different rig pressures. Equilibrium composition was based on 20% O_2 in reactants.

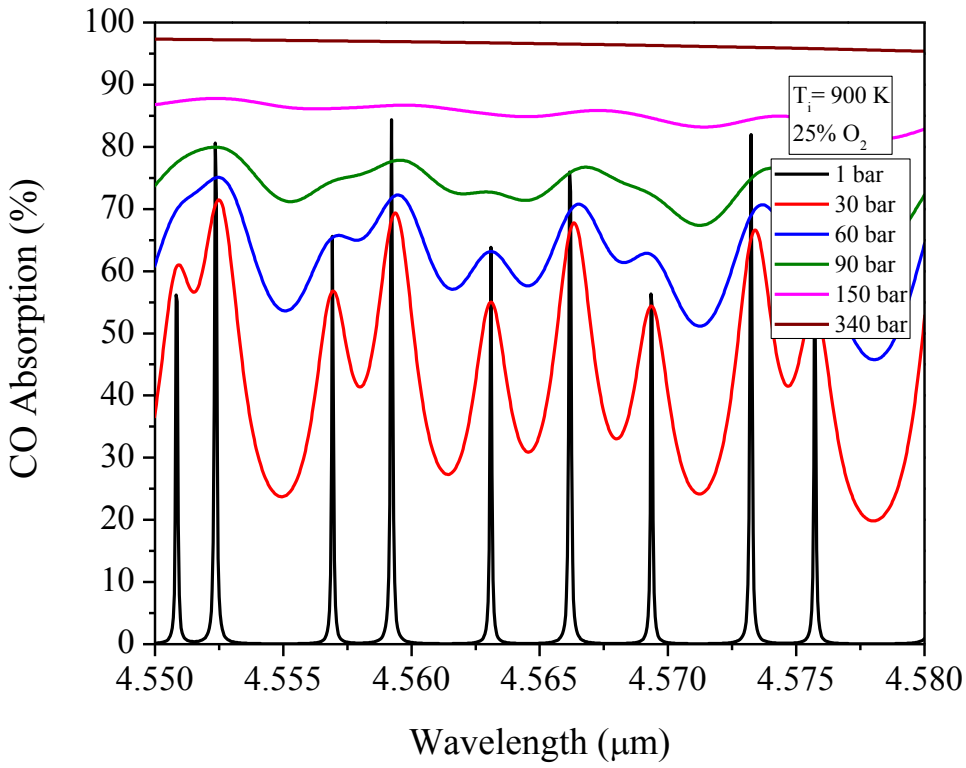

Figure A. 9 IR absorption from CO at different rig pressures. Equilibrium composition was based on 25% O_2 in reactants.

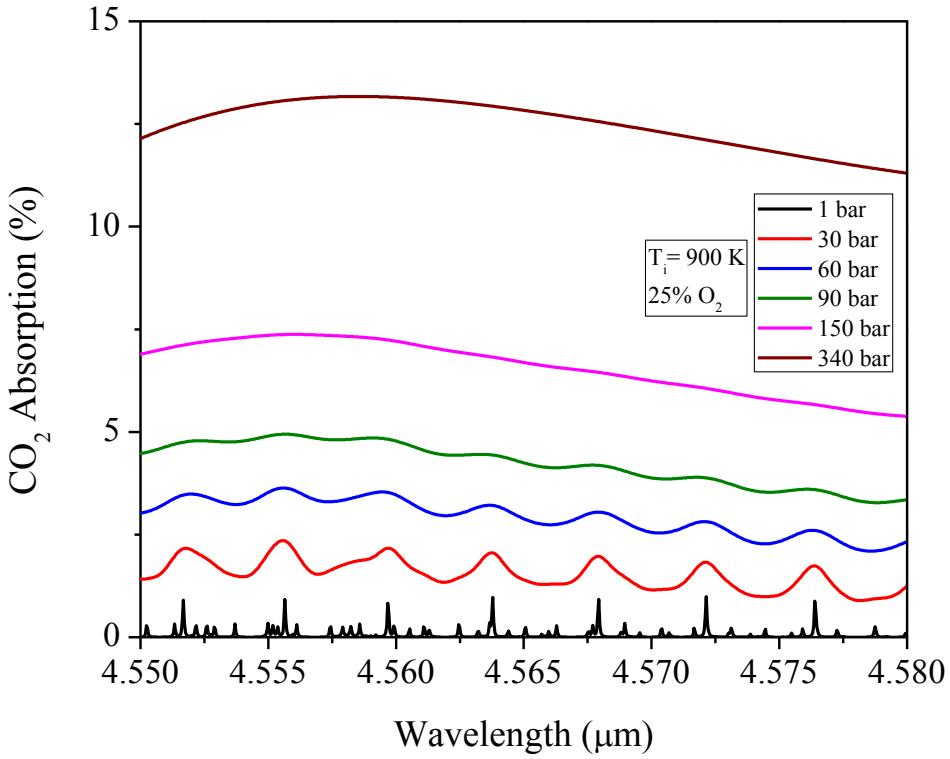

Figure A. 10 IR absorption from CO_2 at different rig pressures. Equilibrium composition was based on 25% O_2 in reactants.

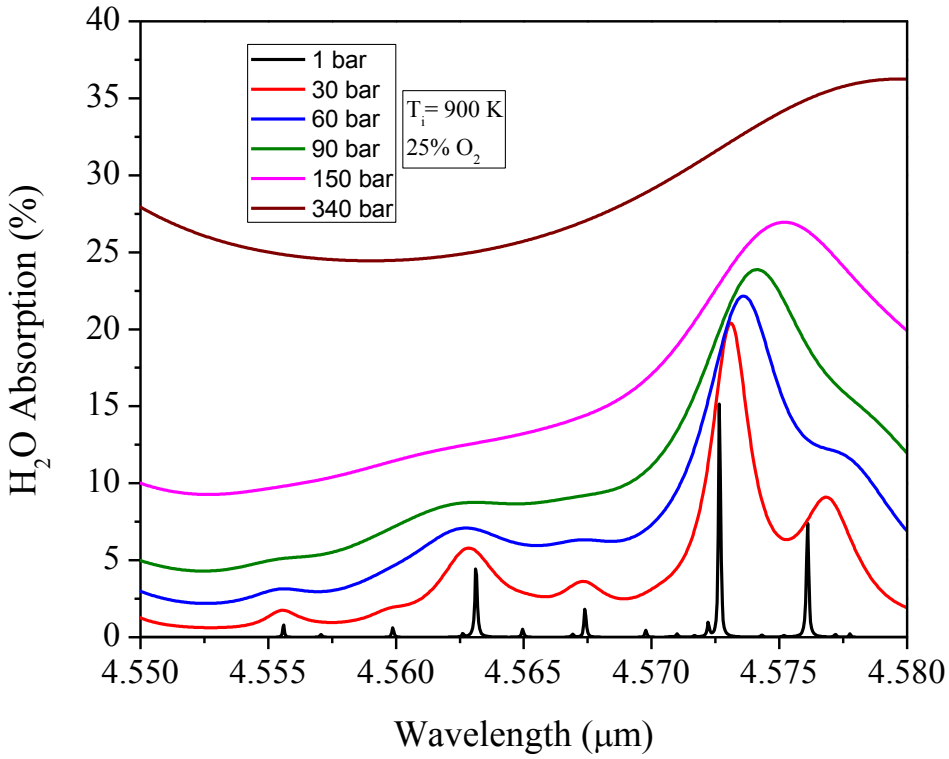

Figure A. 11 IR absorption from H_2O at different rig pressures. Equilibrium composition was based on 25% O_2 in reactants.